

**IMPACT AND POST-IMPACT RESPONSE OF A COMPOSITE MATERIAL TO
MULTIPLE NON-COINCIDENT IMPACTS**

by

Kevin R. Cromer

A thesis submitted to the Faculty of the University of Delaware in partial fulfillment of the requirements for the degree of Master of Science in Mechanical Engineering

Spring 2010

Copyright 2010 Kevin R. Cromer
All Rights Reserved

**IMPACT AND POST-IMPACT RESPONSE OF A COMPOSITE MATERIAL TO
MULTIPLE NON-COINCIDENT IMPACTS**

by

Kevin R. Cromer

Approved: _____
Michael Keefe, Ph.D.
Co-advisor in charge of thesis on behalf of the Advisory Committee

Approved: _____
John W. Gillespie, Jr., Ph.D.
Co-advisor in charge of thesis on behalf of the Advisory Committee

Approved: _____
Anette M. Karlsson, Ph.D.
Chair of the Department of Mechanical Engineering

Approved: _____
Michael J. Chajes, Ph.D.
Dean of the College of Engineering

Approved: _____
Debra Hess Norris, M.S.
Vice Provost for Graduate and Professional Education

ACKNOWLEDGEMENTS

It is through the eyes of those I love that I may truly measure the worth of my accomplishments.

TABLE OF CONTENTS

ACKNOWLEDGEMENTS	iii
LIST OF TABLES	vii
LIST OF FIGURES	ix
ABSTRACT	xv
1 INTRODUCTION.....	1
1.1 Introduction.....	1
1.1.1 Impact of Composites	4
1.1.2 Compression after Impact (CAI)	9
1.1.3 Flexure after Impact (FAI)	11
1.2 Summary.....	14
1.3 Organization of Thesis	17
2 BACKGROUND OF EXPERIMENTAL METHODS AND MATERIALS	20
2.1 Introduction.....	20
2.2 Manufacturing Techniques	21
2.2.2 Vacuum-Assisted Resin Transfer Molding (VARTM)	22
2.2.3 Material Quality.....	25
2.3 Materials	28
2.3.1 Matrix.....	28
2.3.2 Fibers	31
2.4 Testing	33
2.4.1 Impact	34
2.4.2 Nondestructive Evaluation (NDE).....	38
2.4.3 Compression after Impact (CAI)	45
2.4.4 Flexure	51
2.5 Summary.....	56

3	STRESS ANALYSIS OF CAI AND FAI SAMPLES	58
3.1	Introduction.....	58
3.2	In-Plane Loading.....	59
3.2.1	Infinite Orthotropic Plate with Inclusion/Hole.....	60
3.2.2	Stress Distribution in an Infinite Width Plate	66
3.2.2	Notched Strength.....	69
3.2.3	Finite Orthotropic Plate with Hole	71
3.2.4	Finite Orthotropic Plate with Orthotropic Inclusion.....	73
3.3	Bending Loads	78
3.3.1	Infinite Orthotropic Plate with Orthotropic Inclusion	79
3.3.2	Infinite Orthotropic Plate with Hole	82
3.3.3	Infinite Isotropic Plate with Hole	89
3.3.4	Bending of a Finite Orthotropic Plate with Hole.....	95
3.3.5	Bending of a Finite Orthotropic Plate with Orthotropic Inclusion.....	96
3.4	Summary.....	101
4	EXPERIMENTAL STUDY OF CAI AND FAI.....	103
4.1	Introduction.....	103
4.2	Samples.....	104
4.3	Single Impact	106
4.3.1	Impact	106
4.3.2	Damage Evaluation.....	111
4.3.3	Post-Impact	118
4.3.4	FEA of Post-Impact Performance	125
4.4	Multiple Impacts	133
4.4.1	Impact	133
4.4.2	Damage Evaluation.....	142
4.4.3	Post-Impact	146
4.4.4	FEA of Residual Performance after Multiple Impacts	155
4.5	Summary.....	167
5	CONCLUSIONS AND FUTURE WORK	171
5.1	Introduction.....	171
5.2	Multiple Impact Testing	171

5.3	Flexure after Impact (FAI)	173
5.4	Damage Width Analysis.....	176
5.5	Future Work.....	178
REFERENCES.....		179

LIST OF TABLES

Table 2.1	Quality characteristics for the parent panels from which samples were cut.....	26
Table 2.2	Weight and density measurements used to calculate the FVF of the six parent panels.....	27
Table 2.3	Mechanical properties of commercially available fiber reinforcements [36].	32
Table 2.4	The low, middle, and high impacts produced consistent incident and absorbed energy values with a low standard deviation (Stdev).....	37
Table 2.5	Threshold values with standard deviations and the percent difference between the areas associated with these values.	45
Table 2.6	Strength values for the nominal material and samples damaged by a single impact.	50
Table 2.7	Flexural modulus and strength results for the nominal material and samples damaged by a single impact.	54
Table 3.1	Composite properties used for the finite element model.....	67
Table 3.2	The orthotropic properties used by Hsieh <i>et al.</i> [44] are applied to the FE model to compare the results.	88
Table 3.3	Tangential moment concentration for an infinite orthotropic plate around the boundary of a circular hole [44].	88
Table 3.4	Stress concentration results for uniaxial bending of an infinite plate with $\nu=0.25$ compared to exact values of three-dimensional elasticity [51].	93
Table 3.5	Composite properties used for the out-of-plane bending model.....	97
Table 4.1	Quality characteristics for the parent panels from which samples were cut.....	106

Table 4.2	Impact parameters for the three energies used in single impact.	107
Table 4.3	Impact characteristics for ten samples at three incident energy levels	108
Table 4.4	Area and diameter measurements of threshold images for each impact energy.....	112
Table 4.5	Residual compressive properties of five samples as each impact energy.	119
Table 4.6	Flexural results for five samples at each impact energy.....	120
Table 4.7	Impact characteristics of the first middle-energy impact at two separation distances.	135
Table 4.8	Impact characteristics of the first high-energy impact at two separation distances.	136
Table 4.9	Impact characteristics of the second middle-energy impact at two separation distances.	137
Table 4.10	Impact characteristics of the second high-energy impact at two separation distances.	138
Table 4.11	CAI results for samples damaged by two impacts separated by 2in and 0.5in at middle and high energies.	147
Table 4.12	Residual flexural properties after two impacts separated by 2in and 0.5in at the middle and high impact energies.	148

LIST OF FIGURES

Figure 1.1	A flow diagram illustrates the methods and assumptions used to achieve the goals suggested for this research.	16
Figure 2.1	Schematic of VARTM process including gas permeable membrane to assist evacuation of volatiles [32].	24
Figure 2.2	Completed VARTM setup and infusion of four parent panels.	24
Figure 2.3	Photomicrograph of typical void size and location.	26
Figure 2.4	Relative toughness characteristics of CCMFCS2 to commercial resin system [37].	30
Figure 2.5	24 oz/yd plane-weave s-2 glass fiber mat.	33
Figure 2.6	Experimental setup of the Instron drop-weight impact tester.	35
Figure 2.7	Setup of simple-support impact.	36
Figure 2.8	Schematic diagram of pulse-echo C-scan by peak amplitude analysis [38].	40
Figure 2.9	C-scan water tank mounted with perpendicular guide rail/drive assemblies to scan the transducer over the submerged samples.	40
Figure 2.10	Image histogram for low and high impact energies.	42
Figure 2.11	A Gaussian peak fit analysis was used to approximate the two modal shapes as normal distributions. Two threshold values were taken from each image according to these curves.	42
Figure 2.12	Typical C-scan images with the corresponding threshold areas for samples with (a) no, (b) low, (c) middle, and (d) high energy impacts.	44
Figure 2.13	Experimental setup for CAI testing in an Instron 4484 universal testing machine.	46

Figure 2.14	Adjustable fixture assemblies for CAI testing [18].	46
Figure 2.15	Typical CAI plots show that though the loading slopes appear similar there is a distinct difference in strength for various impact energies.	48
Figure 2.16	(a) Acceptable CAI failure typically occurs through the impact damage site. (b) Unacceptable failure can occur as a result of the loading concentration induced by the support fixture (end crushing).	48
Figure 2.17	IITRI compression setup with typically failed sample.	50
Figure 2.18	Fixture setup for four-point FAI testing.	52
Figure 2.19	Flexural load versus deflection for the nominal material and samples damaged by a single impact.	54
Figure 2.20	Typical failure modes for the flexural tests included compressive failure on the loaded surface and ultimate failure by fiber rupture.	55
Figure 3.1	An infinite anisotropic plate of arbitrary shape contains an elliptical inclusion and is subjected to in-plane loads at infinity [24].	60
Figure 3.2	Boundary conditions at the inclusion boundary [24]	63
Figure 3.3	Radial stress distribution around a circular hole in a plywood plate under unidirectional tension [40].	65
Figure 3.4	Tangential stress distribution around a circular hole in a plywood plate under uniaxial tension [40].	65
Figure 3.5	Quarter-symmetric in-plane model with refined triangular mesh at the inclusion and inclusion boundary.	67
Figure 3.6	FE in-plane stress distribution for experimental backing panel material.	69
Figure 3.7	The effect of hole diameter on the stress concentration in a finite plate containing the experimental material.	72
Figure 3.8	Stress distribution of finite width experimental material composite material: $W/D=3$.	72
Figure 3.9	Effect of inclusion stiffness and damage width on the in-plane stress concentration of a finite width plate with a central inclusion.	74

Figure 3.10	As the inclusions approach one another the maximum in-plane stress concentration at their edges begins to significantly increase.	75
Figure 3.11	Effect of inclusion stiffness and damage width on the in-plane stress concentration of a finite width plate with two inclusions separated by 2in.	76
Figure 3.12	The in-plane stress concentrations and moduli for samples with a single central inclusion and symmetrically displaced inclusions are similar.	77
Figure 3.13	Coordinates at the inclusion boundary of an anisotropic plate under coupled bending-stretching [43].	80
Figure 3.14	Biaxial bending of an infinite anisotropic plate with an elliptical hole [44].	84
Figure 3.15	Distribution of moment component concentrations around a circular hole in a orthotropic plate under uniaxial bending for fiber orientations of (a) 0°, (b) 30°, (c) 60°, and (d) 90° [44].	87
Figure 3.16	Generalized bending of an infinite isotropic plate with a circular hole [51].	90
Figure 3.17	Moment concentrations for an infinite isotropic plate with various hole diameters and Poisson's ratios from out-of-plane bending [45].	94
Figure 3.18	Effect of inclusion width and stiffness on the apparent flexural modulus of a finite plate containing (a) a centrally located inclusion and (b) two identical inclusions separated by 2in.	99
Figure 3.19	Effect of inclusion width (D) and stiffness on the moment concentration at the edge of the inclusion within a finite plate of finite width (W) for (a) a centrally located inclusion and (b) two identical inclusions separated by 2in.	100
Figure 4.1	Plane-weave fiber construction used in the experimental material.	105
Figure 4.2	Normalized impact characteristics for three impact energies.	110
Figure 4.3	Linear relationship of damage area to absorbed energy. Energy absorbed increases with incident energy (Figure 4.2).	110

Figure 4.4	Typical C-scan images with the corresponding threshold areas for samples with (a) no, (b) low, (c) middle, and (d) high energy impacts.....	114
Figure 4.5	Damage by out-of-plane impact in composites typically contains delaminations and matrix cracking. The larger delaminations are typically further from the impacted surface creating an overall conical shape [56].	116
Figure 4.6	Representative samples were sectioned and polished to visualize the extent of the damage through the thickness and to gauge the accuracy of the C-scan images (3x magnification).....	117
Figure 4.7	The residual (a) modulus, (b) flexural strength, and (c) compressive strength tend to decrease with increasing damage area.....	121
Figure 4.8	Normalized residual mechanical properties after a central, three-point impact of varying energy.....	123
Figure 4.9	Samples damaged by the three impact energies failed similarly in (a) compression and (b) flexure.	124
Figure 4.10	As damage width increases the inclusion stiffness begins to plateau, creating a bilinear-type trend ($W = 4$ inches)	127
Figure 4.11	The particular inclusion stiffness suggests that estimating the damage as a hole may be unnecessarily conservative.....	129
Figure 4.12	While the inclusion values do not exactly match, the moment concentrations predicted by the model may be similar to the experimental strength ratios.....	129
Figure 4.13	Plotting the experimental and FE stress concentrations against their shared damage diameters shows a good correlation of the FE model.	130
Figure 4.14	Though the exact inclusion stiffness is not known for the CAI samples, the stiffness values read from the chart are comparable to those from the flexural models.	132
Figure 4.15	Similar trends emerge when comparing the in-plane concentrations of the flexural models and the experimental strength ratios.....	132
Figure 4.16	Impact characteristics for two impacts separated by 2in at (a) middle and (b) high energies.	140

Figure 4.17	Impact characteristics for two impacts separated by 0.5in at (a) middle and (b) high energies.	140
Figure 4.18	C-scans of the damage in samples impacted with a 2in separation show two distinct damage regions with no overlap for both the (a) middle and (b) high energies.	143
Figure 4.19	An overlay of the initial damage caused by (a) middle and (b) high impact energy shows that the bulk of its growth coincides with the formation of the second damage region.	144
Figure 4.20	Sections through the damage of samples impacted twice with a 0.5in separation show a greater degree of matrix cracking on the back surface as well as more severe delaminations than those with a single impact (Figure 4.6): 3x magnification.....	145
Figure 4.21	Plot of residual (a) flexural modulus, (b) flexural strength, and (c) compressive strength against maximum damage area.	149
Figure 4.22	Comparison of normalized residual properties for the (a) middle and (b) high impact energies at separated locations.	152
Figure 4.23	Failed CAI and FAI samples for the (a) 2in and (b) 0.5in separated impacts.....	154
Figure 4.24	While the inclusions of the (a) 2in impacts have a similar slope and plateau as the single impacts, the loss of stiffness in the (b) 0.5in impacts appears more drastic with increasing damage diameter.....	157
Figure 4.25	The experimental modulus data for (a) 2in and (b) 0.5in impacts show the effect of inclusion stiffness and diameter.	159
Figure 4.26	Though the experimental and FE stress concentrations for the (a) 2in and (b) 0.5in impacts may not exactly correspond, there is good agreement between the inclusion stiffness of the model and those read from the chart.	160
Figure 4.27	The (a) 2in and (b) 0.5in separated impacts show more disparity between experimental and FE stress concentrations, but they may still be considered suitable conservative approximations.	162
Figure 4.28	Though the exact stiffness for the (a) 2in and (b) 0.5in impacts is not known, values read from the design charts seem reasonable compared to the flexure models.	165

Figure 4.29 While there is a greater disparity between the in-plane stress concentrations for the (a) 2in and (b) 0.5in impacts, the distributions appear to significantly overlap.....166

ABSTRACT

It is well known that laminated composite materials are susceptible to damage by out-of-plane impact, often associated with a corresponding reduction of mechanical properties. Much research has been conducted to characterize the impact and post-impact response of various composite systems, but little attention has been given to the proximity effects of repeated impacts. Structural composite panels developed for military vehicles must survive numerous impacts of various energies with distinct damage characteristics. The size, number, and proximity of these events may have a unique influence on the structure's residual performance.

A series of low-velocity drop-weight impact tests were conducted on S-2 glass/epoxy samples simply-supported along two edges. Three single-impact energies were used to determine the effect of damage size on the residual performance. Two of those energies were used to study the effect of impact proximity; 0.5in and 2in distances separated the two impacts. Along with damage size, the residual compressive strength and flexural properties were measured. An elastic finite element model was developed to approximate the impact damage as an elliptical inclusion. The damaged modulus and inclusion dimensions were used to uniquely determine the inclusion stiffness. The corresponding stress concentration was then used to predict the experimental loss of strength.

Increasing incident impact energies exhibited greater absorbed energy, associated with larger damage dimensions. Post-impact tests and stress analyses revealed that both damage size and inclusion stiffness are related to the extent of overall structural degradation. Thus, simply considering the damage to be a hole may be overly conservative. Multiple impact tests showed that when separated by 2in, the initial impact damage does not influence the material's response during a second impact. At 0.5in, however, the damage areas significantly overlap, increasing the absorbed energy and degree of damage. This correlated to a significant loss of flexural modulus and strength as well as compressive strength. With these results it seems that a multiple non-coincident impact method could potentially gauge the damage tolerance of various composite systems. Also, it is feasible to model the damage dimensions and elastic flexural modulus as a nondestructive means to reasonably predict the residual flexural and compressive strength.

Chapter 1

INTRODUCTION

1.1 Introduction

The benefits of composites have been well documented as their presence in society is becoming more pervasive. Their strength-to-weight-ratio and environmental resistance make them especially attractive for many applications. For example, the United States Army's desire for lightweight alternatives to traditional steel or aluminum materials is driving the research behind new composite systems. These systems are commonly thick-section laminates that require significant damage tolerance to repeated impacts at high energy levels. In a laboratory setting, these impacts will be generated by a controllable and repeatable drop-weight tower that will monitor the response of the panels and characterize their damage tolerance, especially to repeated impacts.

Damage tolerance of composites is important in both ballistic and structural applications. For example, in ceramic-composite armor systems, high-energy impacts typically induce a global deflection of the panel and local crushing and fragmentation of the ceramic core at the impact site. The effectiveness of the ceramic tile at each impact site is dependent on the retention of structural support (i.e. damage tolerance). In the case of lightweight composite vehicle applications, the composites must withstand multiple low velocity impact such as tool drops and tree impacts over the vehicle lifetime without

loss of structural properties or excessive maintenance and repair - the materials must be damage tolerant. As with many composites, this panel is susceptible to damage from out-of-plane impacts that ultimately reduce its overall mechanical properties through delamination and matrix and fiber cracking. Thus, the question arises as to the tolerance and survivability of a damaged backing panel subjected to multiple impacts.

Compression after impact (CAI) has become the accepted standard for damage tolerance testing. It was developed alongside an impact method by the aerospace industry to test materials against simulated bird strikes or accidental tool impacts. On an actual structure, these events are typically considered to be isolated and the damaged component is promptly repaired or replaced. A thick-section composite structure, however, is expected to be impacted consecutively at neighboring locations before replacement. The number of impacts, their size, and their proximity to each other may have a unique effect on the residual properties of the material. Based on CAI testing, damage tolerant materials are those that exhibit smaller damage sizes and higher residual strength after impact. The influence of multiple impacts on damage size and residual strength has not been widely studied. The properties determined by this test, i.e. in-plane compressive strength after impact, are also not directly relevant to the flexural loading conditions that are commonly encountered in vehicle structures during off-road missions. The residual flexural strength and loss of flexural stiffness due to multiple out-of-plane impacts will also be studied.

As a precursor to expensive, large-scale tests, a small-scale impact procedure will be developed to explore the potential structural response of a multiply impacted backing

panel composite. While experimental tests have been developed to measure the damage tolerance of composite systems, little work has been done on the multiple impact response of these materials. The effects of multiple damage sites on the impact and post-impact response of a representative material will be recorded through a series of mechanical tests. A flexure after impact (FAI) test will be used alongside the standard CAI to compare its practicality as a damage tolerance technique. The correlation between the elastic flexural modulus and other residual properties will be investigated to study its viability as a metric for the reusability of a damaged panel.

In the field, vehicle operators are not typically outfitted with nondestructive inspection equipment (e.g. ultrasonic C-sans), but there remains a need to gauge the survivability of the damaged structures. For high-energy or ballistic impacts, however, the most apparent indication of an impact event is the resulting visual damage. Therefore, this study will also record the correlation between the dimensions of a damage region to the residual properties of the damaged material. As with most composites, much of the damage can be invisible (e.g. delaminations within the laminate); but its visibility is likely related to the severity. The samples will be ultrasonically scanned to ensure that the maximum dimensions of the damaged region are recorded. A strong correlation may justify further investigation into the connection between visible damage and structural retention of full-scale panels. If successful, the damage itself could provide another nondestructive means to predict the residual impact tolerance of a damaged panel. However, this study also reveals that the residual stiffness of the damaged region is an important factor on the residual global stiffness and strength of the impacted laminate.

While samples used throughout this research will be far smaller than typical backing panels, the methodology used herein may be adopted for larger panels to be tested with the CCM's newly developed high energy impact test capabilities.

1.1.1 Impact of Composites

While advanced composites offer a number of superior design characteristics, they are generally susceptible to damage caused by an out-of-plane impact. To study the tolerance of these materials, a standard method [1] was developed to induce damage into a composite plate via low-velocity drop-weight impact. This technique was originally developed to simulate the impact created by a tool being dropped on a structure, and has come to be the standard for categorizing the damage resistance of composite systems. It will be modified to include the effects of multiple, non-coincident impacts and to better simulate the response of a larger structure.

Impact testing can help establish the influence of stacking sequence, fiber surface treatment, fiber volume fraction (FVF), and processing variables on the damage resistance of a composite laminate. It can also be used to compare the damage resistance for composites with different constituents. As only a single material system is considered in this research, this section will present the results of researchers who address these parameters. It could be expected that these parameters may similarly affect the results for the conditions tested in this research, but further testing will be needed to verify.

Drop-weight test machines can be instrumented with a variety of data collecting equipment. Velocity detectors, displacement gauges, and rebound height indicators constitute a number of different setups, but typically force versus time is the most basic

measurement. The contact force history provides crucial insight into the response of the material and also contains data that can be used to calculate other impact characteristics that are not otherwise measured: velocity, displacement, and energy.

The force-versus-time histories, however, typically contain many oscillations which are introduced by two primary sources. The first source is the natural frequency (or frequencies) of the impactor, often referred to as “impactor ringing”. The second source of force oscillations is the flexural vibration of the impacted specimen. Ringing generally occurs at higher frequencies than the oscillations generated in the specimen. These high-frequency oscillations do not typically represent an actual force transmitted to the specimen. However, oscillations caused by the motion of the specimen depict actual forces and are a factor of the material response. Both types of oscillations are usually excited during initial contact and during the formation of damage. Tracy *et al.* [2] showed that the presence of damage, however, does not greatly affect the natural frequencies and mode shapes of the specimen. Therefore, these vibrations can be ignored in the raw impact data since they do not reflect the presence of damage and should be consistent for a single material. The resonant response of the material, however, likely dissipates a portion of the impact energy. This energy will be assumed much less significant than that dissipated by the formation of damage.

Low-velocity impact induced damage typically consists of permanent indentation, matrix cracking, fiber breakage, and delaminations. These damage mechanisms dissipate the majority of the energy. This is most often triggered by transverse shear stresses that develop cracks within plies. Kwon and Sankar [3] studied the static load-indentation

behavior of several graphite-epoxy laminates. The combination of interlaminar shear and flexural stresses were shown to initiate matrix cracking before a sudden load drop was caused by the unstable propagation of delaminations. A linear relationship was found between the delamination radius and maximum applied force. They also performed low-velocity impact tests that generated force-deflection diagrams similar to the static indentation results, and the initiation and propagation of delaminations also showed good correlation. Kumar and Narayanan [4] found that delamination induced by impact was caused mainly by mode II fracture. In their experiments, only 11.4% percent of the incident impact energy was required to initiate delaminations.

Both fiber and matrix properties tend to influence the impact and damage tolerance of composite systems. Morton *et al.* [5] compared the damage resistance of nine composite material systems and showed that brittle systems have lower threshold velocities and a higher damage area growth rate than systems including a toughened matrix. Wang *et al.* [6] showed that the addition of glass fiber plies to graphite/PPS composites improved the overall impact resistance of the material. The maximum tolerated load and absorbed energy were found to increase with larger percentages of glass fibers. The additional strain energy dissipated also helped decrease the sudden catastrophic failure mode often associated with brittle graphite fiber composites.

Lagace and Wolf [7] conducted impact tests on laminates with different fiber layups. They found that the peak force and the impact duration were not affected by the lamination scheme. However, Wang and Khang [8] showed that for graphite/PEEK cross-ply laminates with 15 plies, the stacking sequence had a major influence on the

total delamination area. The laminate with the lowest number of interfaces between plies with different fiber orientations had the largest delamination area. Hull and Shi [9] concluded that the overall stiffness of the laminate determined the geometry of the damaged area, and that the local stacking sequence near an interface determined the shape of delaminations.

While the impact behavior of fiber reinforced composites has been extensively documented, still relatively little research has been conducted to address the endurance of such materials under repeated impact loading. Hosur *et al.* [10] investigated the effect of repeated impacts on the damage resistance of stitched and unstitched S2-glass/epoxy composites. They found at low incident energies that the peak load does not significantly change with the number of impacts, but at higher energy levels the peak load shows a distinct drop with the increase of impact events. Sugun and Rao [11] performed repeated low-velocity drop-weight impacts on glass/epoxy, carbon/epoxy, and Kevlar/epoxy composite materials. Their results also show a steady decrease of peak load as the number of impacts increase. This was accompanied by an increase in the total energy. They also concluded that mapping the final damage contour can help evaluate the damage tolerance of polymer composites subjected to repeated impacts.

The experimental results of Morais *et al.* [12] show that cross-ply and non-symmetric laminates have greater damage resistance than unidirectional laminates to repeated low-velocity impacts. This is attributed to the ability of multidirectional reinforcement to hinder the formation and propagation of through-thickness and transverse matrix cracks that would eventually contribute to the final failure of the

material. Icten [13] compared the tolerance of cross-ply and quasi-isotropic composites to repeated impacts. While quasi-isotropic laminates tend to have a slightly higher number of impacts to failure they also develop larger failure areas than those found in the cross-ply samples. Therefore, it may be expected that a cross-ply laminate will retain greater residual strength during post-impact tests sensitive to the size and type of damage, i.e. compression after impact.

Wyrick and Adams [14] discovered that the damage in carbon/epoxy laminates increased with increasing number of impacts. They also found that the incident energy level and the number of impacts significantly influence the degradation of the residual properties [15]. Rotem [16] noted that the damage area increases under repeated impact and is associated with a distinct reduction in strength and modulus values. He found this mechanism to be more severe in brittle materials, like graphite/epoxy, than for more ductile glass/epoxy composites; an observation supported by Harris *et al.* [17].

Low-velocity, low-energy impact typically produces damage, often invisible, from the contact stresses between the impactor and laminate. Rotem [16] reported only slight changes in the residual flexural strength since it primarily depends on the lower layers during bending, which remain relatively undamaged. After repeated impacts, however, he found that the intensification of damage allows greater bending under an equivalent impact load and correlates to a significant loss of residual strength and modulus.

1.1.2 Compression after Impact (CAI)

In order to evaluate the damage tolerance of laminates, a standard compressive method was developed by Boeing and adopted by the ASTM to quantify the membrane-dominated response to the damaged material [18]. It is a uniaxial compression test on a damaged quasi-isotropic laminated plate. The damage can be induced by quasi-static indentation or drop-weight impact. The damaged plate is installed in a multi-piece support fixture that includes vertical edge-supports to minimize loading eccentricities and bending. The specimen is inserted into the fixture assembly and compressively loaded until failure.

In-plane compression is generally regarded as the critical loading condition for impact damaged specimens. Delaminations are traditionally the dominant failure mode under low-velocity impacts and CAI shows particular sensitivity to the size of the induced delaminations. Nehjad and Parvizi-Majidi [19], as well as a number of other researchers, showed a strong correlation between the size of the delaminated area to the residual compressive strength; smaller damage areas give smaller reductions in residual strength [19]. Since much of the energy absorbed during impact is accumulated by the formation of these delaminated regions, CAI strength ultimately depends on the energy dissipated by the specimen during impact.

Just as the material parameters influence the impact response of composite structures, so do they contribute to the retention of mechanical properties. Therefore, it is expected that composites with different constituents, layups, thicknesses, etc. are likely to correspond to a particular retention of residual properties. The work of a number of

researchers will be revisited in this section to highlight these effects. By extending the current investigation to include these variables, the results may be compared to the findings of previous researchers.

Mechanical properties of the matrix, fibers, and the fiber-matrix interface each have a particular effect on the residual compressive strength of impact-damaged composites. Chen *et al.* [20] showed that impact damage reduced the compressive strength of thin walled composite struts by a maximum of 45-55% when a graphite-epoxy material system was used. With a toughened epoxy matrix, the maximum strength reduction was approximately 10%. The experimental work of Pintado *et al.* [21] showed that the use of toughened matrices and interleaved systems improved the residual strength of impact-damaged laminates in compression as well as in bending. Manders and Harris [22] found that fiber surface functionality, which promotes adhesion between fiber and matrix, is a key requirement for damage tolerance. In addition, the CAI tests indicated that the fiber tensile strength has relatively little influence and that, for a given fiber, higher matrix strain to failure improves the CAI strength. Hull and Shi [9] also concluded that CAI strength is matrix dominated and correlates positively with the maximum strain to failure of the resin.

Dost *et al.* [23] presented extensive experimental results for 24-ply graphite-epoxy laminates showing that stacking sequence can significantly affect the CAI strength. They found that the degree of laminate orthotropy strongly affects the failure mode as larger changes in orientation angles from layer to layer tend to result in lower CAI strength.

Monib *et al.* [24] investigated the effect of resin toughness and through-the-thickness stitching on the damage tolerance of thick-section composites. Panels were ballistically impacted and the residual compressive strength was measured using a Compression after Ballistic Impact (CABI) method. Stress analysis showed that the stress concentration and corresponding membrane failure are sensitive to the in-plane stiffness of the damaged region. Delamination growth failure, on the other hand, is dependent on the size and location of the damage as well as the fracture toughness. Experimental results showed that through-the-thickness stitching improved fracture toughness and reduced the size of damage. The stiffness within the damage region, however, was severely degraded due to fiber breakage and pullout. By examining fracture toughness, inclusion stiffness, and finite width effects, design charts were developed to optimize the damage tolerance of the composite panel.

1.1.3 Flexure after Impact (FAI)

The post-impact mechanical properties of composites have been receiving extensive investigation in recent years, most of which devoted to compression properties [13, 17-24]. The research on residual flexural properties, especially the influences and mechanisms of the various factors, are still few [16, 25-31].

A test method has been established to characterize the flexural properties of composite materials [25]. This test method utilizes a four point loading system applied to a simply supported beam. The major difference between four point and three point bending modes is the location of the maximum bending moment and maximum axial fiber stress. In four-point bending the maximum axial fiber stress is uniformly distributed

between the loading noses. In three-point bending the maximum axial fiber stress is located immediately under the loading nose. The support span-to-specimen thickness ratio is chosen such that failure occurs in the outer fibers of the specimens, due only to the bending moment.

Low-velocity impact-induced non-penetrating damage in pultruded glass fiber composites was investigated by Zhang and Richardson [26]. An instrumented drop-weight impact test machine with a chisel shaped impactor was used to create the damage. The post-impact structural integrity of impacted specimens was evaluated under three point bending tests, which revealed that flexural strength is more sensitive to the presence of localized damage than modulus. Damage area was shown to increase with incident impact energy just as the residual flexural properties were shown decrease with the same energy increase.

Chenghong *et al.* [27] explored the effect of fiber properties on the residual flexural properties of impacted composites. Three types of fibers were studied: S-2 glass, basalt, and Twaron 1000 (aramid). Basalt fiber has similar mechanical properties to glass and displayed similar damage mechanisms to the glass during a high energy impact. The aramid beams also produced a similar damage evolution, but their flexural properties decreased more significantly at low impact energy than the glass or basalt. For all of the fibers, however, the reduction in residual flexural modulus is slightly larger than that in strength, especially for aramid reinforced spell out beams (contrary to the work of Zhang and Richardson [26]). All three composites beams show a similar variation in residual flexural properties as a function of impact energy.

As discovered by Peijs *et al.* [28], the surface treatment of the fibers also tends to influence impact and post-impact behavior of composite systems. Hybrid carbon composites incorporating plies with surface-treated high-performance Polyethylene (HP-PE) fibers showed improved damage tolerance to low-energy impacts. At high energy, however, extensive fiber fracture occurred in the HP-PE plies. They concluded that the increased level of adhesion due to the surface treatment induced a more brittle failure behavior. With the fracture of the HP-PE fibers, the energy storage capacity diminishes and damage in the carbon plies becomes more severe. The hybrids containing untreated HP-PE fibers, on the other hand, showed no fiber fracture in the HP-PE plies at any of the impact energies. As a result, the residual flexural strength of the laminates hybridized with treated fibers impacted at higher energies was found to be lower than that of the untreated hybrids.

Though woven fibers provide greater control and consistency during the manufacture of composites, the damaging effects of the weaving process on the fibers are commonly acknowledged. Mouritz *et al.* [29] compared the impact and post-impact performance of non-woven and woven glass fiber laminates. Damage was induced by a low-velocity impact after which the residual flexural and shear properties were measured. The woven fiber composite contained a slightly lower flexural strength than that of the non-woven laminate with a significant reduction in interlaminar shear strength. Under repeated impacts the woven laminates experienced a large deterioration in flexural strength due to the increase in fiber damage.

Experiments conducted by Mariatti *et al.* [30] on various laminates and weave patterns showed that the mechanical properties of woven composites are significantly influenced by the weave pattern. Satin- and plain-weave plies in single- and three-ply constructions were tested with and without the presence of damage in the form of a hole. The flexural strength and modulus of the satin-weave tended to be larger in both the single- and three-ply laminates with and without holes. The difference in mechanical properties is partially attributed to resin flow characteristics during the manufacture of the composites, especially in thicker laminates. For the given process, they found that the satin-weave allowed greater interply resin impregnation that ultimately resulted in better mechanical properties.

While flexural properties tend to be fiber dominated, matrix properties dictate certain damage mechanisms associated with bending modes. Kim *et al.* [31] studied the influence of a rubber-modified matrix on the post-impact residual flexural properties of a fiber composite. Along with the flexural strength and modulus, the residual stiffness and the Mode I interlaminar fracture toughness were determined under dual cantilever beam testing. Results clearly demonstrated that residual mechanical properties for the composites with rubber-modified matrices are better than those of the unmodified controls. An increase of 25% for the flexural strength and modulus and 80% for the fracture toughness were reported for the modified resin system.

1.2 Summary

While the damage resistance and tolerance of composites has been extensively investigated in recent years due to the development of standardized methods, little

attention has been given to the response of such materials to repeated impact; section 1.1.1 presents the work of various researchers that characterized the response of composites repeatedly impacted at the same point. Much less work has been done, however, to address multiple impacts at separated locations. Structural backing panels on military vehicles will contain numerous impacts over the surface of the panel, which are more likely to be in the same vicinity than at the same point. Therefore, this study will provide recommendations as to the viability of a non-coincident multiple impact method to gauge the damage tolerance of composite panels and its adaptability to test full-scale backing panels.

While CAI is the traditional method for ranking the damage tolerance of composite materials, it does not simulate the flexural loading conditions commonly encountered in vehicle mobility testing. Failure in such cases is likely to be dominated by bending and shearing mechanisms that are not accounted for in compression tests. Thus, the reusability of a damaged backing panel may be more dependent on the residual flexural properties. As seen in Section 1.1.2, CAI has been extensively studied for various material systems and results have shown an excellent agreement between damage size and residual strength. This, however, has not been accomplished for flexure after impact (FAI) and so will be investigated in this study. If a reliable correlation exists, the damage size alone may be used as a nondestructive means to approximate the residual mechanical properties of a damaged backing panel. These properties may in turn be a good indicator for the survivability of the panel.

The goals for this research may be better illustrated by the flow diagram in Figure 1.1. An impact method will be developed to measure the effect of multiple impacts on the residual response of a composite plate. The resulting damage size and residual properties will also be measured to explore various damage tolerance techniques. This data will be combined in a simple finite element (FE) model to determine the particular stiffness within a commensurate idealized elliptical inclusion. The combination of the inclusion's size and stiffness will likely produce a unique stress concentration that may be used to predict the loss of strength. This prediction can be compared back to the experimental values to determine the accuracy of these methods.

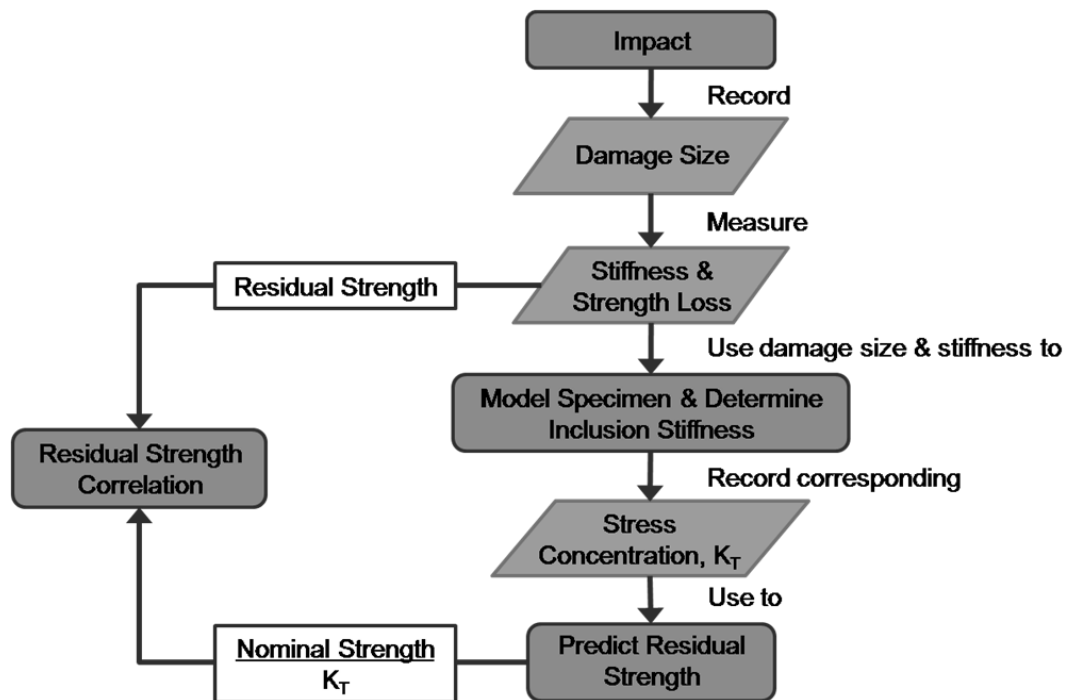


Figure 1.1 A flow diagram illustrates the methods and assumptions used to achieve the goals suggested for this research.

This study will only address the performance of a single representative backing panel material. As can be seen in the studies presented in this chapter, the impact and post-impact mechanical response of composite systems can be highly dependent on the composition of the materials. Therefore, results cannot be scaled to other material characteristics or testing conditions. Further testing will be required to develop a more complete picture for the response of a composite system under the conditions tested in this study. The primary intention of this research, however, is to discuss the applicability and feasibility of these tests such that further investigation is justified. If so, the results of the researchers referenced in this chapter may provide general expectations for the performance of other materials.

1.3 Organization of Thesis

Chapter 2 provides background information on the processing and testing methods used in this research. A discussion of the materials used in this study includes comparisons to the properties of similar materials, which gives insight into the application of the given composite system. A number of tests will be conducted to understand the effects of multiple impacts on the mechanical response of this material. Certain ASTM standards are referenced in an attempt to standardize the procedures developed specifically for this research. As previously discussed, these tests are often not scalable in terms of materials, layups, etc., so a series of studies by various researchers have been presented that address some of these issues.

In Chapter 3, a theoretical background is introduced to develop a foundation for modeling the response of damaged laminates. Analytical methods for in-plane loading of

anisotropic materials with inclusions are presented. Lekhnitskii's solution to an infinite plate with an elastic inclusion has been deconstructed to give a continuous solution to the distribution of stresses across an infinite plate as a result of an open hole. A finite width correction factor has been applied to this solution to approximate the notched strength of weakened panels and the resulting distribution of in-plane stresses. Though not much literature exists in regards to bending plates with an elastic inclusion, especially of finite width, the work of three researchers is recapitulated to provide a broad starting point for modeling. These solutions address the bending-stretching coupling of an anisotropic plate with an elastic inclusion, the generalized bending of an isotropic plate with an elastic inclusion, and the bending of anisotropic plate with a hole or rigid inclusion. Results from the analytical solutions will be used to verify a finite element model that simulates the pure bending of a composite plate of finite width containing an elliptical inclusion of reduced stiffness.

The models developed in Chapter 3 are used to simulate the response of the materials during the tests performed in Chapter 4. Samples will be damaged by a drop-weight impact event at multiple locations to study the effect of the number of impacts and their vicinity on the residual properties of the material. The impacted samples are ultrasonically scanned to visualize and quantify the extent of the internal damage. It is postulated that the dimensions of the damage are predictably scalable to the reduction of mechanical properties, and so could be used as a metric to approximate these properties. Similarly, a nondestructive flexural test is designed to study its potential as metric for other relevant residual properties. CAI has become the standard method for comparing

the damage tolerance of various materials. It will be used alongside the flexural tests as a comparative basis for the sensitivity of flexure to impact induced damage.

Finally, Chapter 5 will discuss the results gathered during the experimental testing. Conclusions will be made as to the viability of gauging damage tolerance using multiple, non-coincident impacts. Approximating the residual properties according to damage size and flexural modulus will also be discussed. Ultimately, the ability to modify these methods to accommodate full-scale panels will determine the relevance of the results to future studies.

Chapter 2

BACKGROUND OF EXPERIMENTAL METHODS AND MATERIALS

2.1 Introduction

This chapter will introduce the techniques, materials, and methods used to create and test a representative backing panel material. Traditional manufacturing and mechanical testing techniques were originally developed by the aerospace industry to address the feasibility of composite material systems as structural components in high-performance applications. New applications are continually emerging, however, so these standardized methods are being modified to accommodate the specific engineering requirements.

One such application, as described in Section 1.1, was proposed by the U.S. Army to replace steel and aluminum monoliths with a lighter weight composite system on military ground vehicles. Unlike aerospace composites these materials are designed to absorb the repeated impact of high-energy events. As a consequence, recent developments in constituent materials have generated materials suitable for this purpose.

The composite used in this research contains S-2 glass fibers from AGY that have a good balance of modulus (86-90 GPa) and high strength (4590-4830 MPa). The fibers are coated with an epoxy resin-compatible chemical sizing. They are infused with CCMFCS2, an epoxy resin system designed by the CCM and available from Applied

Poleramic. The resin combines good toughness with processing-friendly characteristics such as room temperature infusion and low temperature post-bake temperature.

The material will be damaged by a drop-weight impact at multiple locations. An ultrasonic C-scan technique will be used to visualize the extent of the internal damage. The residual properties will be measured using a standard CAI method and modified flexural tests. Experiments will be conducted to determine the correlation of these properties to the associated damage dimensions and apparent flexural modulus.

As discussed, the results from these mechanical tests are subject to numerous variables. These include test rate, boundary conditions, material constituents, layup schedule, etc. Therefore, results can only be compared between materials tested with the same setup. Since only a single material is used in this study, the effects of these parameters were not investigated.

2.2 Manufacturing Techniques

Composites are an attractive engineering material because they offer excellent physical properties for a wide range of applications. They have a considerably high strength-to-weight ratio, offer good flexibility, and are resistant to environmental effects. Unlike their metallic counterparts, externally attached fixtures can be integrally manufactured into the structure of a composite. Composite manufacturing, however, requires specialized processing techniques in order to produce quality parts with controllable and repeatable properties. Numerous techniques have been developed to produce composite parts, which include pultrusion, autoclave and filament winding, and a series of Liquid Molding processes. One such process is known as VARTM (Vacuum-

Assisted Resin Transfer Molding Process), which is a relatively affordable and efficient way to produce quality parts.

Several of the mechanical tests used in the experimental study were developed by the aerospace industry to investigate the effect of impact-induced damage on the residual properties of composite structures. To produce these structures, a basic Resin Transfer Molding (RTM) process is typically used since it provides excellent surface finish, dimensional control, and is compatible with high-performance resin systems. The surface and dimensional requirements for ground vehicles, however, are significantly less restrictive. Therefore, a VARTM process presents a low-cost alternative and the available resin systems will be compared to those for aerospace applications in following sections.

2.2.2 Vacuum-Assisted Resin Transfer Molding (VARTM)

The VARTM process uses a vacuum sealed environment to permeate the matrix material through the fiber layup. Unlike RTM, VARTM uses only a single-sided mold to form the desired part. A basic VARTM setup uses a resin injection line accompanied by a vacuum exhaust line on opposing sides of the part to transfer the resin. An extremely permeable material, or distribution media, is placed over the preform. The vacuum line causes a pressure differential across the preform and draws the resin initially through the distribution media. The resin is simultaneously pulled through the thickness of the preform at much lower pressures than the RTM process. Sequential injection lines allow parts of large size to be produced that are not viable with the RTM setup. Air and excess resin are then drawn from the preform through the vacuum vent line. The compaction of the plies and exhaust of excess resin help produce a panel with a high fiber-volume

fraction (FVF). Voids are also reduced as air bubbles are forced through the layup by the advancing resin. A schematic of the VARTM process is shown in Figure 2.1.

The injection and vent lines offer a certain degree of control over the final FVF. By clamping the injection line after infusion, the pressure gradient is gradually removed until the fibers are uniformly compacted. This also removes further excess resin thereby creating a high FVF part. By clamping both the injection and vent lines, excess resin remains within the fibers and the FVF decreases. A long pot life is necessary in this case as the pressure gradient is more gradually removed. Otherwise, thickness variations are likely to occur. In the case of this research, the vent line was clamped and the resulting FVF values are measured and reported in the following section. A completed VARTM setup and infusion is presented in Figure 2.2. This process was used to manufacture six 2.5ft square parent panels from which the experimental samples were cut.

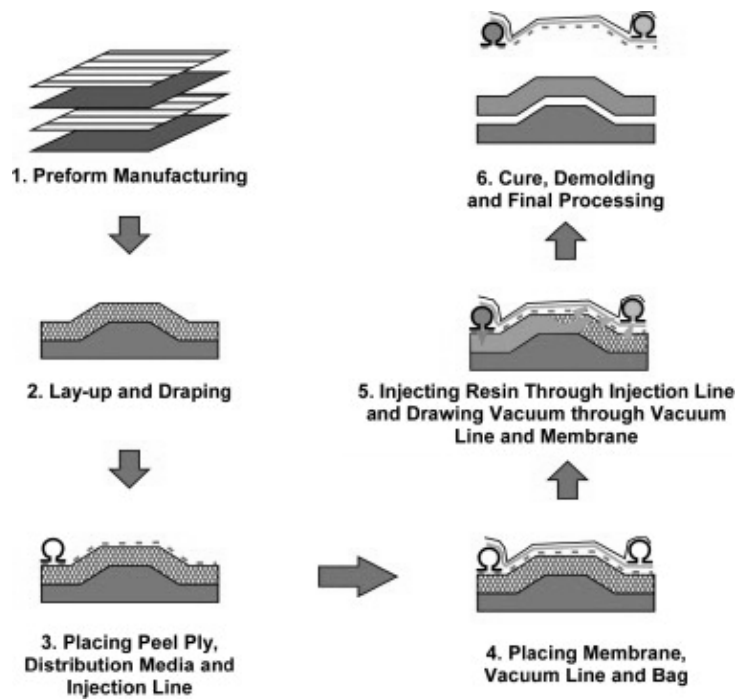


Figure 2.1 Schematic of VARTM process including gas permeable membrane to assist evacuation of volatiles [32].

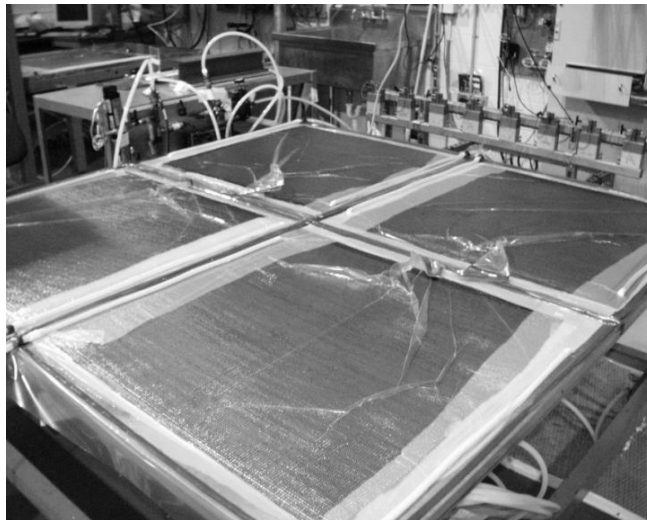


Figure 2.2 Completed VARTM setup and infusion of four parent panels.

2.2.3 Material Quality

It is essential to characterize the quality of the samples being tested. The quality is typically defined by the volume fraction of voids, fibers, and resin.

Voids are inclusions of various sizes that typically exist within the matrix phase of the composite parts that are not removed during the injection process. Voids can be entrapped air or volatiles or regions where the resin has not permeated the fabric or tow (i.e. dry spots). These voids represent a defect in the structure of the composite and can act as a stress concentration during loading applications that reduces strength. An acceptable VARTM part typically contains a void content less than 1-3% over the entire volume. This can be verified using areal-density microscopy, by which the percentage of planar area accounted as voids within a scanned cross-section is assumed proportional to the volume of the part (Figure 2.3). Void content can also be checked using the standard ASTM methods for relative density by displacement (water immersion) [33] and void content based on relative density [34]. For the purposes of this research, this method is considered less reliable than that of microscopy. Since the density of the fibers and resin are not independently verified, the constituent densities used in the method will not be exact. Samples for both methods are typically taken from the edges and center of the parent material to verify the consistency throughout the composite part. Results for the six parent panels are presented in Table 2.1. Void contents of less than 1% were measured reflecting the high quality panels used for testing in this research.

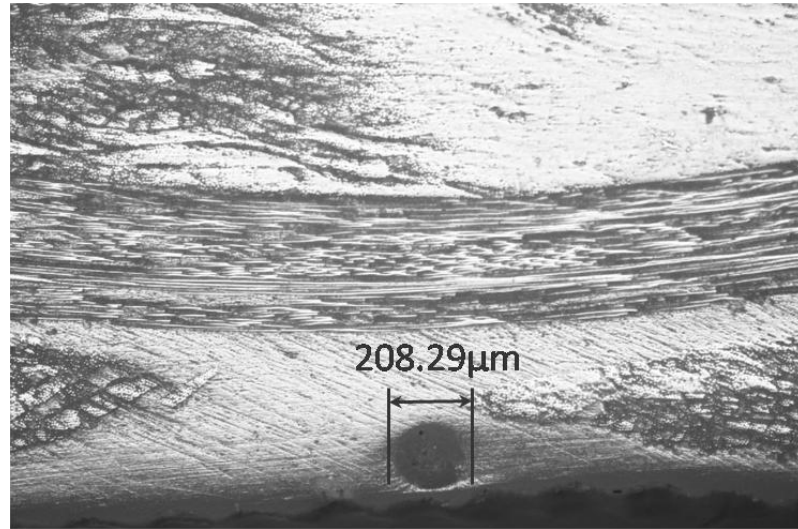


Figure 2.3 Photomicrograph of typical void size and location.

Table 2.1 Quality characteristics for the parent panels from which samples were cut.

Panel #	Thickness (in)	FVF	Void Content
1	0.225	55%	< 1%
2	0.226	57%	< 1%
3	0.223	58%	< 1%
4	0.226	55%	< 1%
5	0.224	58%	< 1%
6	0.227	57%	< 1%

FVF refers to the relative percentage of the volume of fibers to that of the entire part. For woven fabrics used in this study, a FVF of 50-60% is typical of a high quality part. The FVF of the parent panels are checked using the standard ignition loss method [35]. Samples are dried and weighed. They are then placed in an oven above the degradation temperature of the resin but below that of the fibers for several hours. When the resin has completely evaporated from the fibers, the remaining fibers are weighed.

The density of the composite measured by water immersion [33] and the density of the fibers [36] are used to calculate the volume fraction from their weights:

$$FVF = \frac{\rho_c W_f}{\rho_f W_c} \quad (2.1)$$

Values for the density (ρ) and weight (W) of the fibers (subscript, f) and composite (subscript, c) are given in Table 2.2. Though this method also references the particular constituent densities, it is traditionally less sensitive to slight variations of the physical properties than low void content measurements. Again, samples are taken from the center and edges of the panels to verify consistency. The values given in Table 2.1 not only show the high quality of the material but also the consistency across the samples.

Table 2.2 Weight and density measurements used to calculate the FVF of the six parent panels.

Panel #	Composite		Fibers	
	W_c	ρ_c	W_f	ρ_f
	(g)	(g/cm ³)	(g)	(g/cm ³)
1	4.346	1.986	2.969	2.475
2	4.273	2.011	2.981	
3	4.225	2.019	2.985	
4	4.225	1.915	2.978	
5	4.373	2.126	2.956	
6	4.265	2.043	2.944	

2.3 Materials

The standard testing methods for measuring the impact response and resulting residual properties used in the research were originally developed by the aerospace industry to simulate the effects of bird strikes or accidental tool drops on a composite aircraft structure. These tests have been accepted for years as the basic standard for damage tolerance testing of composite material systems. With the development of new composite systems for ground vehicle structures, however, the conditions used in these tests are not particularly relevant to those expected of these new material systems.

Backing panels in military ground vehicles are designed to absorb large loads from high energy impacts. In order for these systems to survive against multiple impacts they must be able to disperse the incoming energy and have superior mechanical tolerance to the damage likely to be induced. Therefore it is essential to employ materials that demonstrate excellent toughness and strength. Since these structures are currently under development, there is no single system or design guideline that has been established. For the purposes of this research, a composite system composed of S-2 glass fibers infused with a CCMFCS2 matrix will be used as a comparable material. Their advantages will be outlined in the following sections as they relate to the conditions expected for a backing panel structure.

2.3.1 Matrix

With excellent mechanical properties and good environmental resistance, high performance epoxies are being used extensively in aerospace composite applications. Their high fracture toughness and good adhesive properties make them more desirable

than traditional vinyl ester and polyester resins. The increase in mechanical performance, however, is often accompanied by a greater cost. Epoxy resins also typically require higher cure temperatures and are more applicable to the traditional RTM processing. New epoxy resins are constantly being developed in order to maximize the mechanical benefits while minimizing processing costs, especially in VARTM applications. Such systems generally maintain a low viscosity and processing temperature but can tend to suffer from a decrease in mechanical properties and glass transition temperature (T_g) as compared to the aerospace resins.

The resin used for this research is a proprietary formulation developed by the CCM and supplied by Applied Poleramic, Inc. (API), known as CCMFCS2. While other commercial systems are available and extensively characterized, CCMFCS2 offers a better balance of processing functionality and mechanical toughness. API also offers two other epoxy systems developed for use in backing panel applications. API SC-15 is the most widely data based VARTM resin for ballistic panels and is used as the baseline for mechanical properties. It allows for a room temperature infusion with a post-cure temperature at 200°F but has a wet T_g of 185°F. SC-79 also allows for room temperature processing and has a wet T_g sufficient for post-cure processing, 275°F. However, the recommended post-cure temperature is 350°F. The fracture toughness and damage tolerance of SC-79 are also significantly lower than that of SC-15.

CCMFCS2 is capable of being VARTM infused at room temperature and post-cured at either a 200°F or 250°F. It features excellent toughness, a simple cure cycle, and a viable hot/wet T_g (245°F). The processing time is expanded with a 16-32 hour gel time

and a mix viscosity of 350cp at room temperature. The mechanical properties of CCMFCS2 are compared to those of SC-15 and SC-79 when infused into 8 plies of 24oz/yd S-2 glass by VARTM as in Figure 2.4. It is easy to see that CCMFCS2 incorporates the ballistic properties of SC-15 with the toughness of SC-79. Therefore CCMFCS2 is chosen as the matrix material for this study and is post-cured at 200°F for eight hours according to the processing guidelines for the resin [37]. Its increase of overall toughness over baseline commercial resin systems makes it a good candidate for a backing panel constituent.

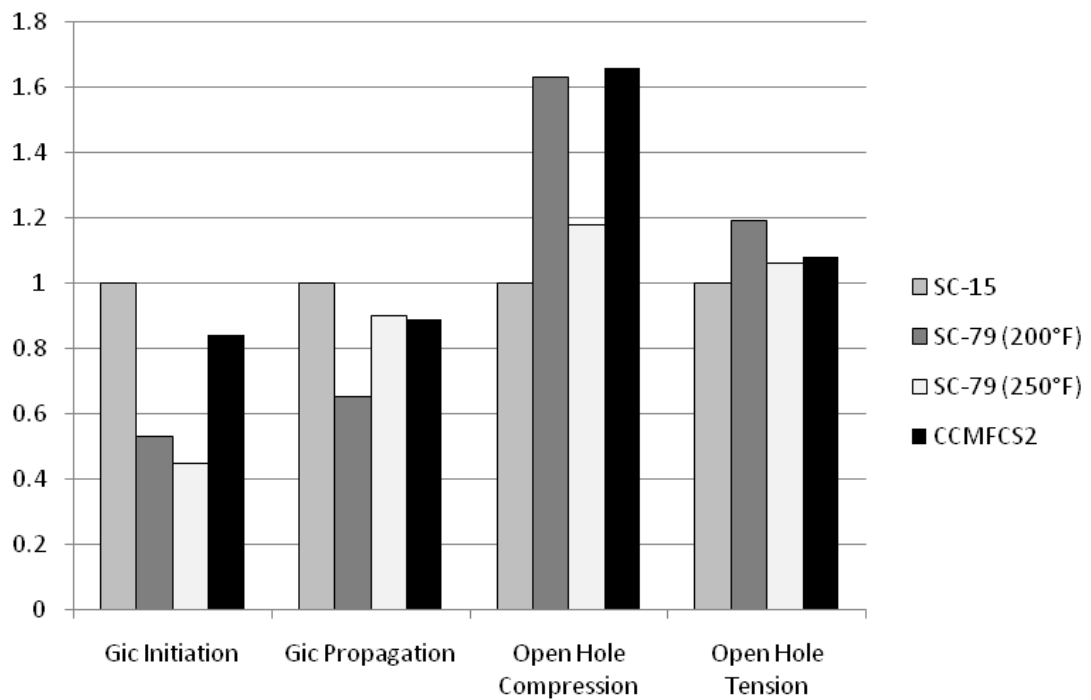


Figure 2.4 Relative toughness characteristics of CCMFCS2 to commercial resin system [37].

2.3.2 Fibers

Traditionally, aerospace composites have been composed of high-stiffness carbon fibers to maintain dimensional stability under high-performance application. As suggested in Chapter 1, this stiffness is often associated with a particular susceptibility to impact damage and a corresponding reduction of mechanical properties. However, such structures are expected to only encounter few unintentional impacts. Composite structures on military ground vehicles, on the other hand, are designed to absorb multiple high-energy impacts but have much fewer dimensional restrictions. Since softer materials tend to dissipate more energy during impact, a low modulus/high strength alternative would be well suited for backing panel composites. High-strength glass fibers, especially S-2, have been used for these applications since the 1980's.

The specific fiber preform used in this research is AGY's 758 *ZenTron* S-2 glass fiber roving. It consists of numerous L-filament (14 μm) continuous glass strands, gathered without mechanical twist in a single bundle and treated with an epoxy-compatible sizing. Table 2.3 gives typical mechanical properties for impregnated strands and single filaments of S-2 glass along with the properties of comparable fiber systems. It is easy to see that though the modulus of S-2 is much smaller than that of carbon and K-49, the strength is significantly higher. This along with a high strain to failure and toughness make S-2 glass well suited for repeated, high-energy absorption conditions. In addition to environmental resistance, S-2 glass composites also have a lower dielectric constant which can potentially provide more radar transparency than similar fiber systems. This presents obvious advantages for military vehicles.

Table 2.3 Mechanical properties of commercially available fiber reinforcements [36].

	S-2 Glass	E-Glass	K-49 Aramid	AS4 Carbon
Impregnated Strand (ASTM D2343)				
Tensile Strength (MPa)	3660-4280	1860-2690	2900-3620	3100-3790
Single Filament (ASTM D2101)				
Tensile Strength (MPa)	4590-4830	3450-3790	N/A	N/A
Tensile Modulus (GPa)	86-90	69-72	124-131	221-234
Strain to Failure	5.4-5.8%	4.5-4.9%	2.5-2.9%	1.5-1.6%
Toughness (MPa)	83-90	62-69	48-55	35-41

The S-2 glass was donated to this project by the Army Research Labs (ARL) in Aberdeen, Maryland USA. It was supplied as a 24oz/yd² plane-weave fabric mat seen in Figure 2.5 (5 yarns/in). To avoid potential effects of the weaving process, a cross-ply construction, $[0^\circ/90^\circ/0^\circ/90^\circ]_s$, was used for the material layup. 8 plies were used to achieve a target thickness suggested by the ASTM mechanical testing standards, which will be discussed later in Chapter 4.

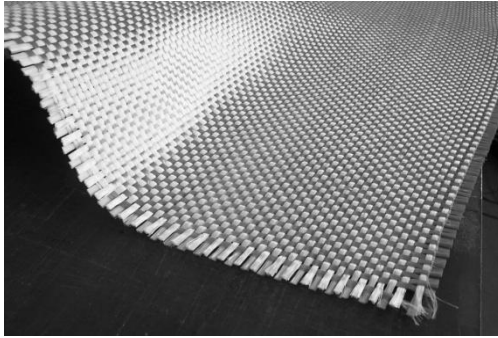


Figure 2.5 24 oz/yd plane-weave s-2 glass fiber mat.

2.4 Testing

This section will provide the relevant background information for the testing procedures used during the experimental portion of this study. The purpose of this research is to investigate the multiple impact response of a representative backing panel material. The influence of secondary impacts on the impact characteristics, damage formation, and residual properties will be explored using a variety of standardized tests. These tests will be modified to specifically suit the parameters of this study, but much of the original procedures will be unaltered to maintain the relevance of the results to the equations and definitions contained therein.

Only a single composite system composed of the materials described in Section 2.3 will be used in the following tests. The results from these tests are typically specific to the material and setup parameters used in the experiment. Since only a single material is used under specific conditions, the results from this study cannot be directly compared or scaled to the results from different configurations.

2.4.1 Impact

This test method covers the damage resistance of multidirectional polymer matrix composite laminated plates subjected to a drop-weight impact event. A flat, rectangular composite plate is subjected to an out-of-plane, concentrated impact using a drop-weight device with a hemispherical impactor. The damage resistance is quantified in terms of the resulting size and type of damage in the specimen. The test method may be used to screen materials for damage resistance, or to inflict damage into a specimen for subsequent damage tolerance testing [1].

Samples were impacted using an Instron Dynatup 8200 basic floor model impact tower, which has a variable weight crosshead of 0.7kg-13.6 kg and a maximum allowable drop height of 3m (Figure 2.6). The crosshead weight is adjusted with a series of lead weights centered above the tup within the crosshead assembly. The impact height is measured from the top of the crosshead at resting position on each sample. Data is recorded through an 8493 strain gauge load cell capable of reading a 89kN (20.0kip) maximum load. According to the standard for composite plate impact [1], a 5/8in diameter spherical-nosed impactor of hardened steel was attached to the load cell. The tup is connected to the data acquisition card through an Instron Impulse Signal Conditioning Unit (ISCU). Load-versus-time data is collected when the crosshead passes through the velocity flag, which also records the impact velocity. Compatible pneumatic rebound brakes were also installed to prevent unintentional secondary impacts and are triggered by delay from the velocity flag.

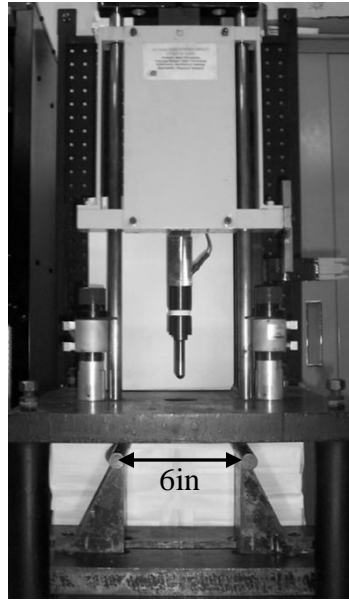


Figure 2.6 Experimental setup of the Instron drop-weight impact tester.

The samples were simply-supported on two-edges with a hardened steel fixture assembly. The diameter of the support noses is 0.75in and the span between their centers is 6in (Figure 2.7). The span length was chosen as a minimum area to include the damage zones of two distinctly separated impacts. The support span also simulates the global response of a larger structure. The samples were elastically held to the support noses to minimize the flexural resonance and specimen slap on the fixture, which could produce inconsistent results. The elastic constraints were such to allow rotation and sliding to preserve the simple-support boundary condition. Both the tup and noses were lubricated to minimize the inherent frictional effects, as were the crosshead guide rails.

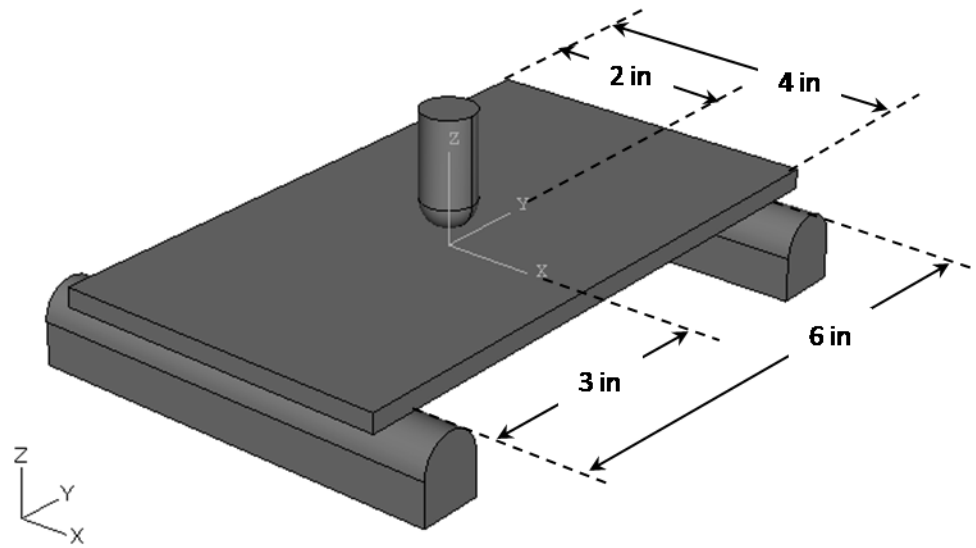


Figure 2.7 Setup of simple-support impact.

In order to determine the energy dissipated during the impact, an external video capture system was used to track the crosshead motion across a fixed scale. A standard 30fps camera was used to monitor the crosshead assembly. As a consequence, the maximum rebound height may occur between the recorded frames. Without compensating for this gap, the maximum error would occur when maximum height is achieved midway between two frames. This error, however, is less than 10% of the lowest expected total rebound height. On the other hand, basic ballistic trajectory equations can be used to approximate the crosshead behavior between the two frames.

This method however cannot distinguish the loss of energy due to friction effects, sample and tup resonance, or damage introduced during impact. As discussed in Section 1.1.1, the natural frequencies of the plate are excited during impact appear as oscillations in the loading curve and dissipate a portion of the incident energy. The Impulse

acquisition software is capable of calculating the total energy of the event and the displacement of the crosshead from the basic laws of motion and the load-vs.-time data. This data is not presented, however, since it was not verified with calibrated external equipment. The equations used to calculate the incident, elastic, and absorbed impact energies are given as follows:

$$Incident\ Energy = mgH = \frac{1}{2}mv^2$$

$$Elastic\ Energy = mgH_R \tag{2.2}$$

$$Absorbed\ Energy = (Incident) - (Elastic)$$

where m is the mass of the crosshead assembly, H is its initial height above the specimen, H_R is its rebound height, v is the velocity at impact, and g is the gravitational acceleration ($9.81\ m/s^2$). Table 2.4 gives the energy values for the single impact condition. Variation of the incident energy occurs from slight differences in the impact velocity. Greater variation may be expected for the absorbed energy, but the results show them to be distinct and repeatable for each incident level. This may correspond to distinct ranges of damage dimensions for each impact energy, which are evaluated as in the following section.

Table 2.4 The low, middle, and high impacts produced consistent incident and absorbed energy values with a low standard deviation (Stdev).

Energy Level	Incident Energy (N-m)		Absorbed Energy (N-m)	
	Average	Stdev	Average	Stdev
Low	18.90	0.03	5.09	0.14
Middle	25.33	0.04	6.85	0.18
High	31.74	0.04	10.23	0.50

2.4.2 Nondestructive Evaluation (NDE)

Material defects in composites can be introduced during the manufacturing process (voids) or by imparting damage through experimental techniques (cracks, delaminations). Depending on the translucency of the material these defects can be invisible to an unassisted observer. Thus, a number of non-destructive inspection techniques have been developed to locate the defects and potentially identify their type. These techniques include X-rays, thermal fields, optical, and in this study, ultrasonic.

Ultrasonic NDE uses focused acoustic energies that interact with the micro-structure of the material being analyzed [38]. Water is often used as a coupling media between the wave source and material as it is efficient at transmitting sound energy and creates a distinct, uniform interface with the material. Acoustic waves become reflected when they encounter variations in density such as those at the water/material interface and those caused by internal damage. Since the acoustic properties of air differ significantly than those of the surrounding material, defects within the material (i.e. voids, open cracks, delaminations, etc.) will reflect different wave characteristics. The resulting feedback includes the variations of wave amplitude and velocity, which are then translated into information regarding the material structure. Precision of such methods is limited in that the ultrasonic data cannot be easily attributed to specific flaw types. Ultrasonic techniques, however, have been developed extensively for isotropic materials and have been shown to accurately capture internal delaminations in a composite material.

In the present study, an ultrasonic technique known as C-scan was used to analyze damage in the impacted samples. C-scans are predominantly used as method to detect large defects within the material, such as inclusions and delaminations. In this method, a short-duration, large amplitude pulse is transmitted to a lithium sulphate transducer to create a 1MHz frequency wave with a 50mm focal length. The focused ultrasonic transducer is rastered over the specimen surface by a pair of encoded screw drives with a 1mm step size. The transducer emits a sound wave that is reflected by the material and received by the same transducer (pulse-echo mode). Generally, the echo characterization is used to highlight interlaminar defects. The amplitude signal is divided into ten discrete levels, each corresponding to a monotonically increasing shade of gray which forms the resulting C-scan image [38].

This technique cannot distinguish between the different types of damage within an impacted region, so the resulting image is typically regarded as a damage envelope. C-scans have been shown to be particularly sensitive to delaminations, however. Since delaminations tend to be the largest damage mechanism induced by impact, the resulting C-scan envelope is a maximum for the damaged region. Therefore, the envelope dimensions can be considered worst case for subsequent analyses.

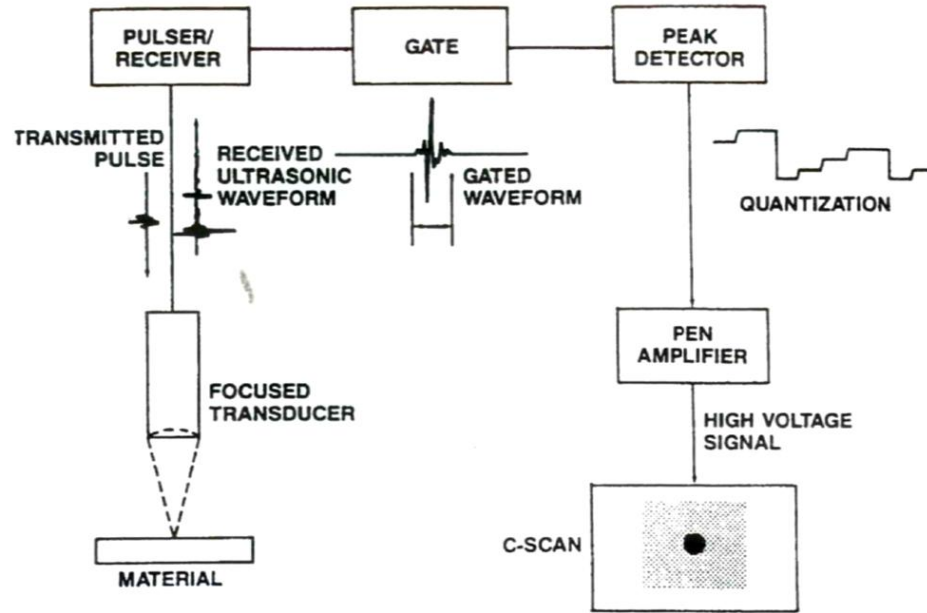


Figure 2.8 Schematic diagram of pulse-echo C-scan by peak amplitude analysis [24].

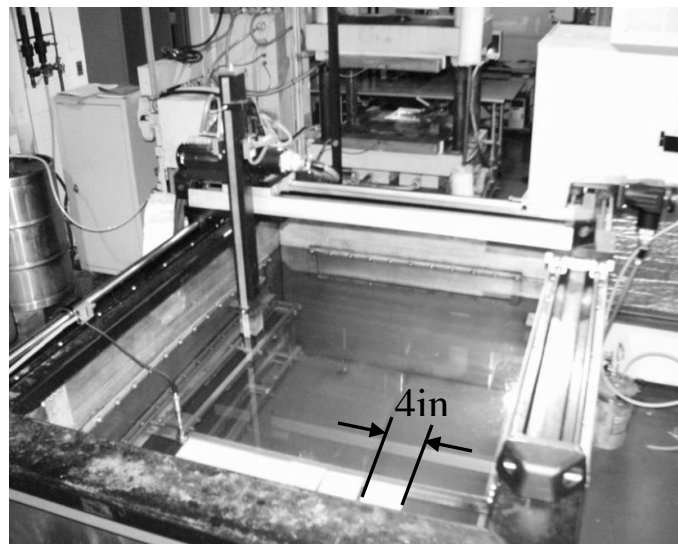


Figure 2.9 C-scan water tank mounted with perpendicular guide rail/drive assemblies to scan the transducer over the submerged samples.

Five samples are scanned simultaneously to reduce scanning time. They are slightly separated so that a distinct boundary appears between each sample. Both the front and back surfaces of each sample are scanned to ensure that the largest damage envelope is recorded. The samples are weighed before and after the scan to ensure that no water remains within the material prior to mechanical testing.

A commercially available image processing software was used to quantify the extent of the damage in the gray scale C-scan images. An image histogram was constructed from each scanned image that counts the number of pixels with the same numeric gray scale values. Figure 2.10 shows typical plots for the low and high single impact energy levels. Two modal distributions can be identified; the first and darker distribution is associated with the damaged area of the material. A Gaussian peak analysis was also performed on each histogram to generate approximate normal curves of the two distributions (Figure 2.11). A single best fit curve then connected the two distributions.

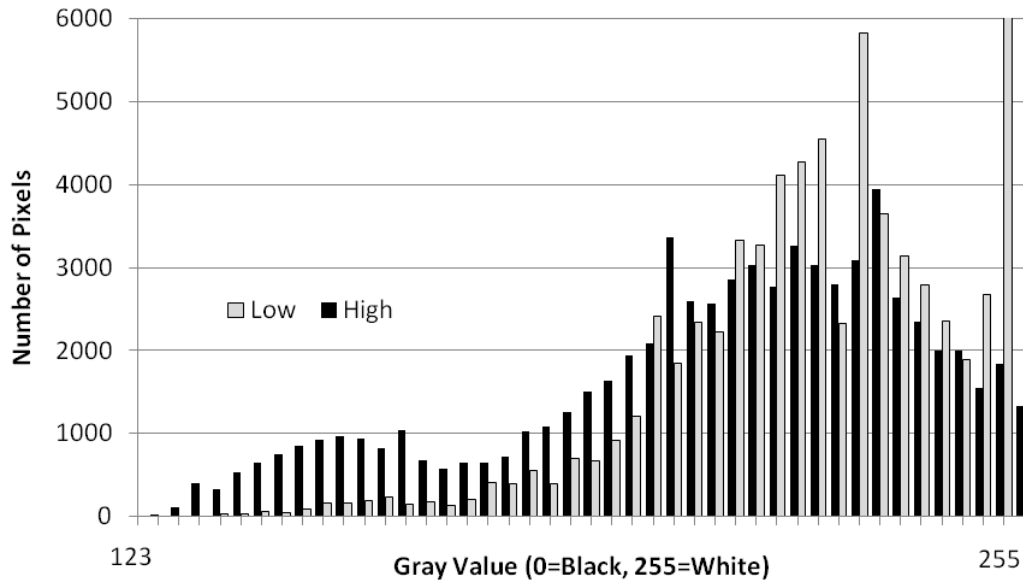


Figure 2.10 Image histogram for low and high impact energies.

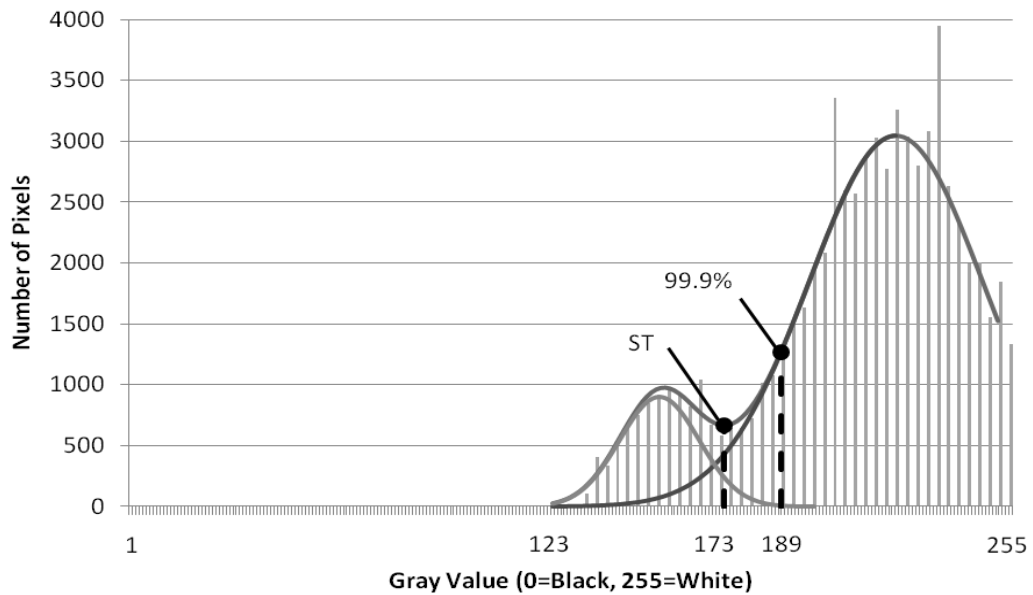


Figure 2.11 A Gaussian peak fit analysis was used to approximate the two modal shapes as normal distributions. Two threshold values were taken from each image according to these curves.

Typically, the slope transition (ST) between the two curves is regarded as a logical thresholding value. In order to account for potential transitional gray-values from the damage to the surrounding material, however, 99.9% of the damaged distribution was used to find the corresponding gray-value (99.9%). The distributions for each image produced their own particular threshold values, above which all values are considered white and below are considered black. Figure 2.12 shows typical results for the threshold images.

Since histograms of the undamaged scans contained only a single modal shape, 99.9% of its distribution was used to find the corresponding threshold value. An edge detection tool¹ was then used to highlight shapes in the threshold images. The largest contiguous area measured from the undamaged images was 37mm². Therefore, only contiguous areas with larger dimensions were recorded from the threshold images of the damaged samples. The maximum width (diameter) across the width (x-direction) of the sample is also recorded. Table 2.5 gives the average threshold values of the three impact energies at both the slope transition and 99.9% gray value. The percent difference between the areas associated with these points is also presented. The effect of this difference on the modeling results will be discussed in Chapter 4.

Scans of the unimpacted samples (Figure 2.12a) show good uniformity of the material; areas in the threshold images appear to be artifacts of the fabric weave. Along with the material quality verified by void content and FVF measurements, this uniformity suggests that the samples are suitable for further mechanical testing.

¹ Paint.NET v3.36; Released by dotPDN, LLC August 27, 2008.

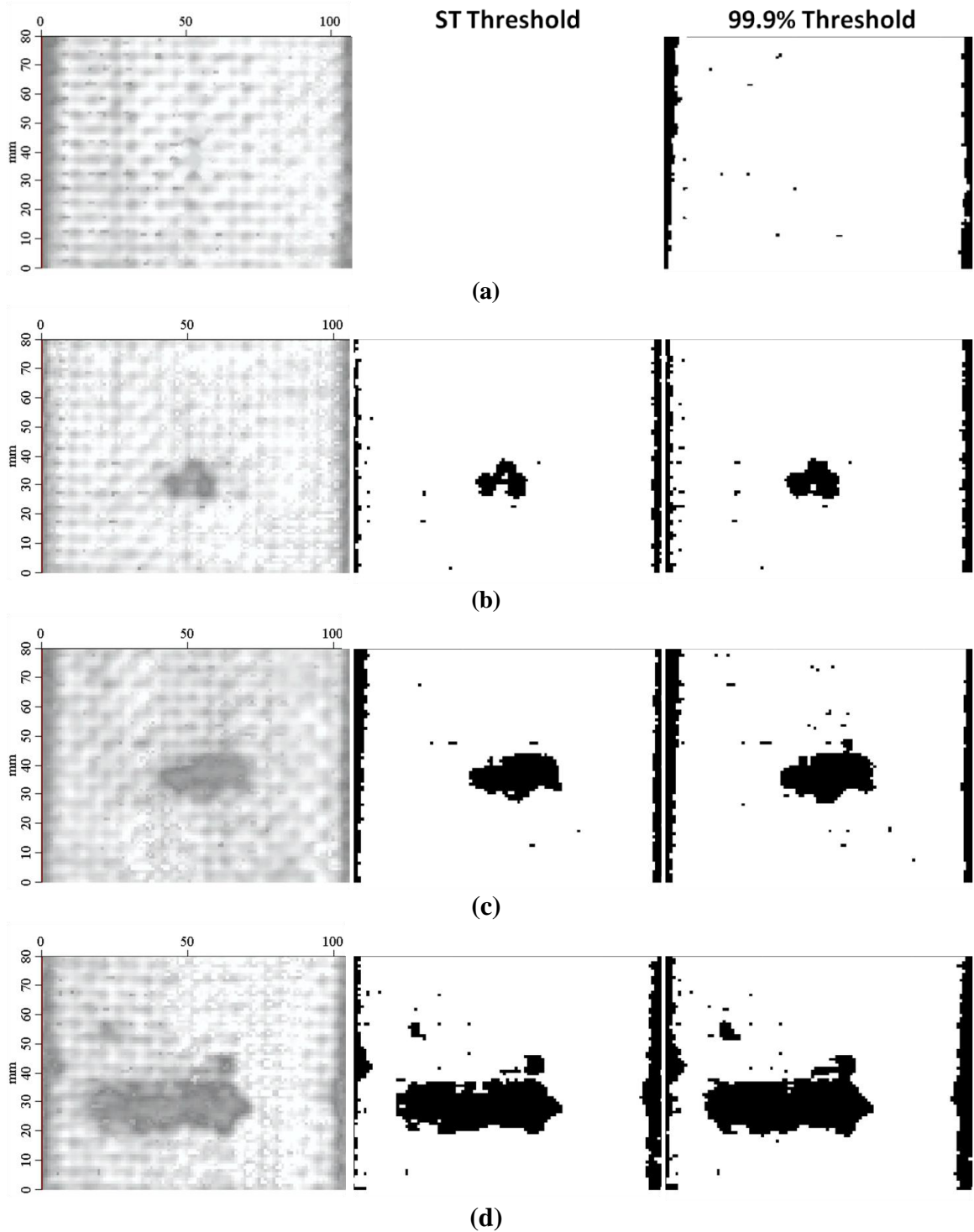


Figure 2.12 Typical C-scan images with the corresponding threshold areas for samples with (a) no, (b) low, (c) middle, and (d) high energy impacts.

Table 2.5 Threshold values with standard deviations and the percent difference between the areas associated with these values.

Incident Energy	Threshold		Percent Difference	
	Slope Transition	99.9%	Diameter	Area
Low	179 ± 3	188 ± 5	26.2 ± 12.0	26.9 ± 10.2
Middle	172 ± 5	181 ± 3	14.7 ± 12.3	23.0 ± 12.0
High	176 ± 9	183 ± 8	2.5 ± 1.9	11.8 ± 3.2

2.4.3 Compression after Impact (CAI)

An Instron 4484 universal testing machine was used for subsequent CAI testing (Figure 2.13) along with a fixture assembly that met the relevant specifications [18]. Samples were trimmed on a precision table grinder to meet the requirements of the fixture (Figure 2.14) and to ensure squareness of the loaded edges. A diamond coated circular blade was used so that residual stresses and machining defects were minimized. The dimensions of each sample were measured with calipers to verify compliance with the standard.



Figure 2.13 Experimental setup for CAI testing in an Instron 4484 universal testing machine.

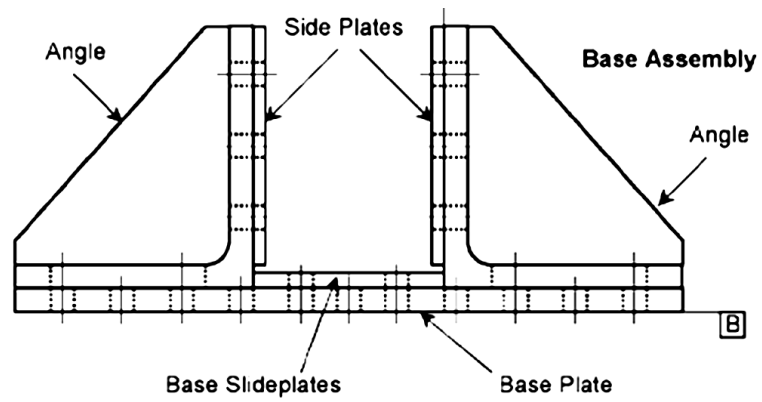


Figure 2.14 Adjustable fixture assemblies for CAI testing [18].

The compressive test fixture is designed with adjustable vertical knife-edge supports to inhibit buckling but not restrain local out-of-plane rotations of the specimen. If gaps occur between the specimen and side supports, errors may arise from sample bending or concentrated loading conditions at the top and bottom specimen surfaces. The fixture must also be carefully centered with the loading axis to ensure uniaxial displacement of the fixture/specimen assembly.

A constant crosshead displacement rate of 0.05in/min was applied until failure or until the load experienced a 30% drop off from its maximum. Applied force and crosshead displacement are recorded while loading. Since strain gauges were not attached to the specimen, residual compressive strength is the only property gathered from this test: peak load divided by the cross-sectional area. Figure 2.15 shows typical load-deflection curves for the samples damaged by a single impact.

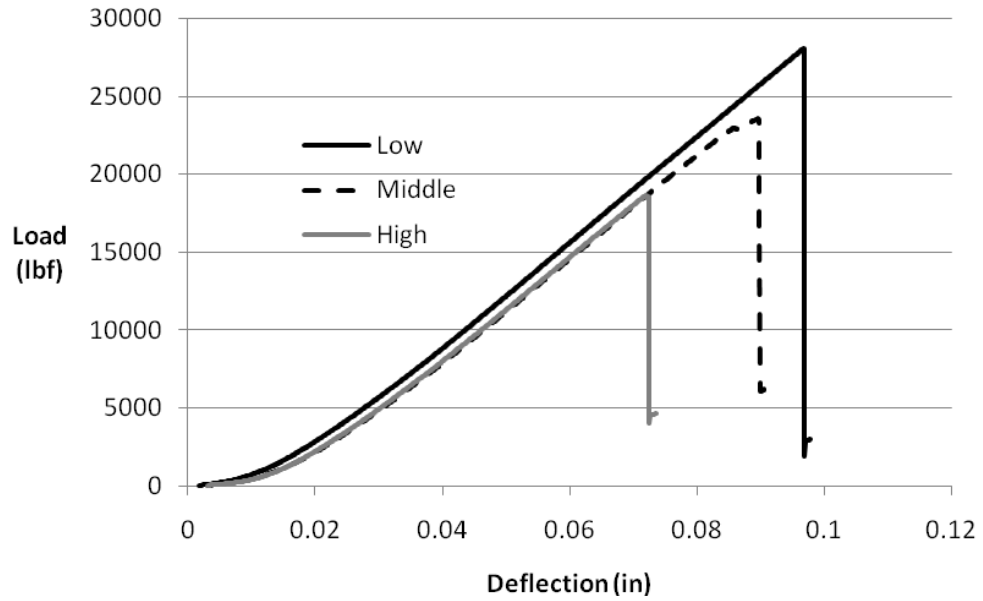


Figure 2.15 Typical CAI plots show that though the loading slopes appear similar there is a distinct difference in strength for various impact energies.

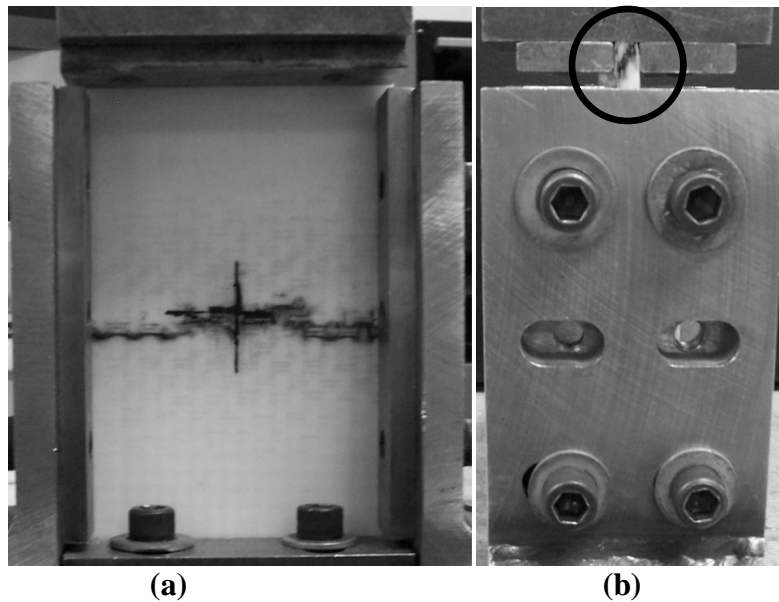


Figure 2.16 (a) Acceptable CAI failure typically occurs through the impact damage site. (b) Unacceptable failure can occur as a result of the loading concentration induced by the support fixture (end crushing).

Only data for samples with acceptable failure modes is recorded (Figure 2.16). These modes may pass through or initiate away from the damage site, especially when the extent of damage is small. Unacceptable failure modes are those related to load introduction by the support fixture, local edge support conditions, and specimen instability. This test method can be used to test undamaged polymer matrix composite plates, but have historically demonstrated a relatively high incidence of undesirable failure modes (end crushing).

An attempt was made to determine the nominal compressive strength of the sample composite using this method. Only a small percentage of the samples tested failed in an acceptable manner. The values of the properly failed samples were verified using a standard compression test [39].

With this test procedure, in-plane compression is applied through an IITRI fixture that contains a series of wedge-shaped grips. The fixture is loaded into the Instron 4484 testing machine (Figure 2.17). As the crosshead descends, shearing forces at the interface of the mating wedges transfer the compressive loads into the specimen. In order to avoid premature failure in the end grips and to have proper load introduction into the specimen, E-glass polymer matrix tabs are bonded to the specimen. Ultimate compressive strength is recorded from the maximum load carried prior to failure divided by the specimen's rectangular cross-sectional area.

Table 2.6 gives the average and standard deviation for the nominal compressive strength as well as the CAI strength of the single-impact samples. As expected, the residual compressive strength appears sensitive to the extent of the impact-induced

delaminations. Not only do the distributions not overlap, but their coefficients of variation (COV) range from 1-7%. This suggests that the CAI response is distinct and repeatable for each impact energy level. Due to the lack of research, however, the sensitivity of the FAI method is still relatively uncertain.

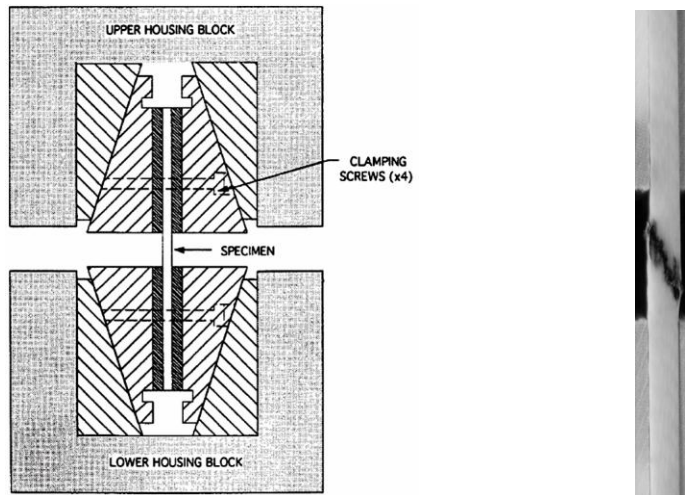


Figure 2.17 IITRI compression setup with typically failed sample.

Table 2.6 Strength values for the nominal material and samples damaged by a single impact.

Incident Energy	Compression Strength (ksi)	
	Average	Stdev
Nominal	36.20	0.46
Low	31.14	0.50
Middle	26.03	1.94
High	20.53	0.94

2.4.4 Flexure

Flexural tests were conducted using the same Instron 4484 universal testing machine as for the CAI testing, and will be referred to as FAI (flexure after impact). The equipment was used to measure load and deflection during four-point flexure. A four-point condition was used so that the maximum axial fiber stress is uniformly distributed over the area between the loading noses, where the damage sites will be situated. This will ensure that the stress path must interact with the damaged material.

Both the loading and support noses had a 0.75in diameter and were constructed, along with the entire assembly, of hardened steel. A load span of 3in was used to contain both separated damage areas between the loading noses. The center of the plate is centered between the loading and support noses. To use the equations directly from the flexure procedure [25] a load span-to-support span ratio of $\frac{1}{2}$ is used, so the support span was set to 6in (Figure 2.18). This gives a span-to-thickness ratio of approximately 27. Great care is taken to ensure that the load and support spans have a common center along the loading axis of the machine. A skewed assembly would affect the material response and render the standard equations inapplicable. Samples were not affixed to the supports in any way so that the conditions most nearly represent simple-support. The load and support noses are lubricated to reduce the effects of frictional contact with the material. A schematic of the experimental flexure setup is depicted in Figure 2.18.

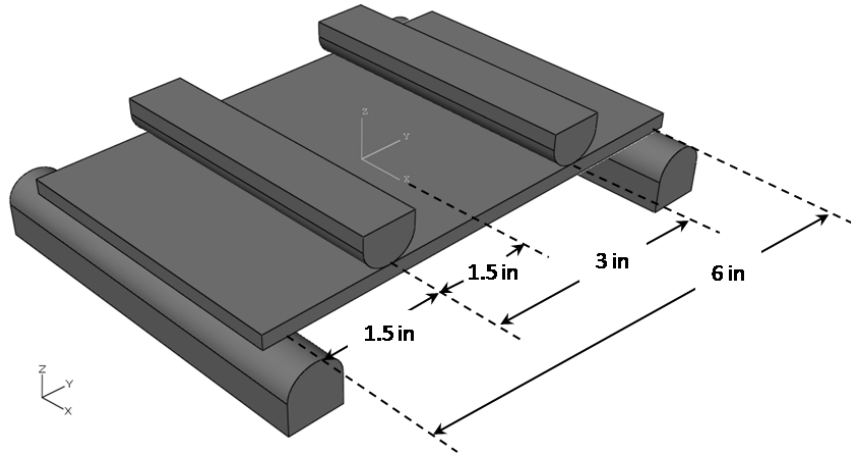


Figure 2.18 Fixture setup for four-point FAI testing.

The span is ultimately limited by the extent of the fixture, but a larger span also requires a larger deflection to fail the samples. The increase in support span may also negate the effects of the damage on the mechanical properties as the bending response tends to be more global with material contributions averaged over a larger area. Three span-to-thickness ratios are suggested in the related standard [25] but a common span with the impact setup, 6in, provides continuity between the measured properties. Samples are trimmed such that there is sufficient overhang of the support noses should excessive deflection cause the contact line with the material to fall within the span plane and slip from the supports.

The constant crosshead displacement rate for the test was determined by the following equation [25]:

$$R = 0.185 \frac{ZL^2}{d}, \quad (2.3)$$

where Z is the strain rate for the outer fibers and is typically set to 0.01(in/in)min. L is the length of the support span and d is the thickness of the beam. During the test the load and deflection are measured, which can be used to calculate the apparent bending modulus by

$$E_{app} = 0.17 \frac{L^3 m}{bd^3}, \quad (2.4)$$

where b is the beam width and m is the slope of the initial straight line portion of the load-deflection curve. The ASTM standard provides a particular equation to calculate the strength of samples that fail at a displacement greater than 10% of the support width caused by a span-to-thickness ratio greater than 16:

$$S_{FAI} = \left(\frac{3PL}{4bd^2} \right) \left[1 - \left(\frac{10.91Dd}{L^2} \right) \right], \quad (2.5)$$

where P is the load and D is the deflection. Typical load-deflection plots are given in Figure 2.19 and sample results for the above calculations are given in Table 2.7.

From Table 2.7 it is easy to see that the residual flexural properties are not sensitive to slight impact damage. There is only a 1% and 4% loss from the nominal modulus and strength, respectively. Significant overlap of the five-sample distributions also exists for both properties. At higher energies, however, the effect of damage becomes more distinct. The modulus loses 11% and 23% for the middle and high impact energies, respectively, while the strength loses 14% and 34%. The largest COV is 4% for the modulus and 7% for the strength, suggesting a repeatable method. But FAI, especially modulus, displays much less sensitivity to the extent of damage than the traditional CAI.

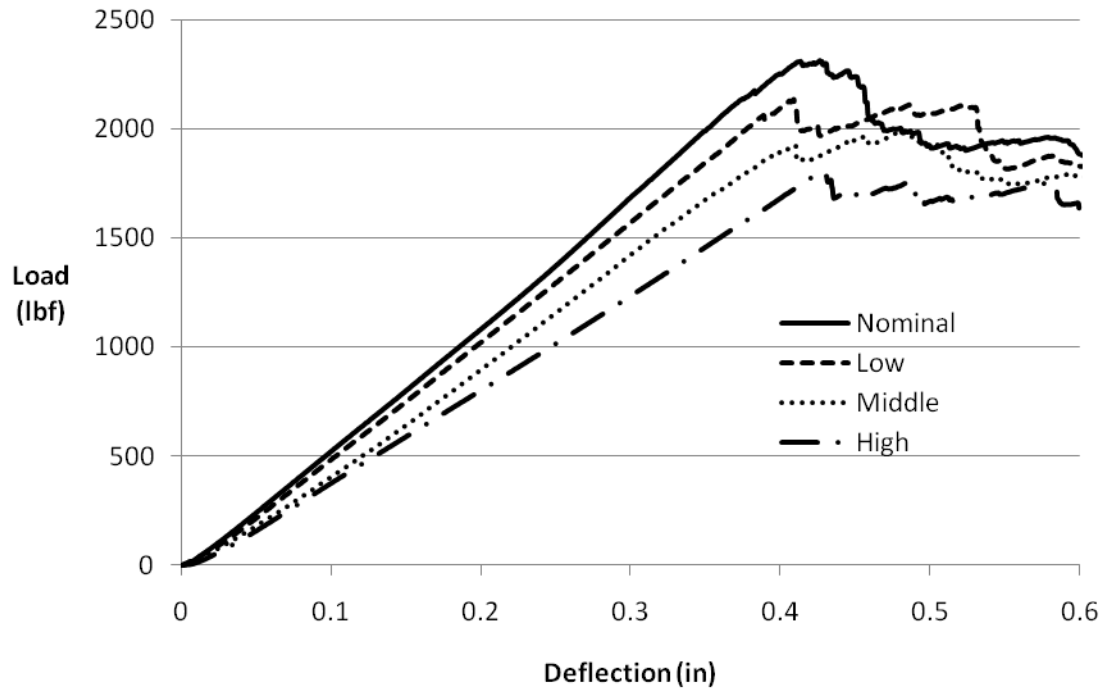


Figure 2.19 Flexural load versus deflection for the nominal material and samples damaged by a single impact.

Table 2.7 Flexural modulus and strength results for the nominal material and samples damaged by a single impact.

Incident Energy	Modulus, E_{app} (Msi)		Strength, S_B (ksi)	
	Average	Stdev	Average	Stdev
Nominal	4.28	0.17	50.76	2.70
Low	4.27	0.16	48.70	2.34
Middle	3.81	0.10	43.40	1.61
High	3.30	0.14	33.59	2.42

Significant displacement continued after the initial load drop-off to allow progressive failure mechanisms to accumulate. After a drop-off of approximately 30% from the peak load was achieved the test was ended. In all cases the load did not increase beyond the initial peak load, so it was this load used for the residual strength measurement. Figure 2.20 shows a flexural sample for which the failure was initiated on the loaded/compressive side but ultimately failing by fiber rupture on the back surface.

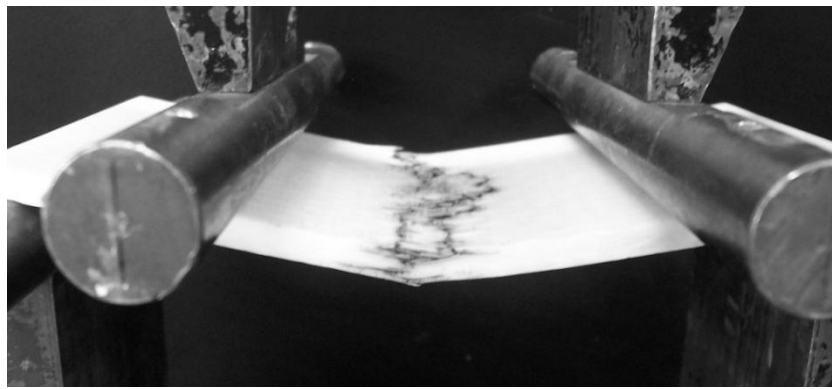


Figure 2.20 Typical failure modes for the flexural tests included compressive failure on the loaded surface and ultimate failure by fiber rupture.

By recording only enough data to determine the initial straight-line portion of the load-deflection curve the test remains elastic and the sample undamaged. For multiply impacted samples the modulus is elastically recorded after the initial impact to verify the damaged modulus. After the final impact, the samples are loaded to failure to access the residual modulus and strength data. Strength tests were also run on undamaged samples to determine the nominal bending modulus and strength of the material. As will be seen

in the following sections, these values will be used to normalize the data from the damaged samples to show a percentage loss in mechanical properties.

2.5 Summary

This chapter provides the background and procedures for the physical testing methods employed in this research. The samples for this study are manufactured with a CCMFCS2 epoxy resin system. It was selected for its ballistic performance and fracture toughness as well as processing characteristics that make it suitable for VARTM manufacturing. This resin showed comparable ballistic and toughness properties to commercially available systems, i.e. API SC-15, but allowed for room temperature infusion with a long gel time and simple, low-temperature post-cure.

The CCMFCS2 matrix is reinforced with S-2 glass fibers developed by AGY and coated with an epoxy-compatible chemical sizing. S-2 glass has a low modulus but high strength and strain to failure when compared to traditional aerospace carbon, which make it ideal for absorbing impact energy without failing.

The constituents are combined using standard VARTM manufacturing techniques to produce high quality S-2 glass/FCS2 panels from 24oz/yd² fabric. Since the parent panels from which samples were cut are manually processed, the void content and FVF are measured to evaluate the quality of the material. C-scans showed uniformity in the undamaged panels and microscopy was used to measure void contents less than 1%. FVF values in the range of 58% were recorded from the standard ignition loss method, confirming the high quality of the panels.

To investigate the multiple impact and post-impact response of this material, a series of standard tests were referenced and modified to accommodate the specific needs of this research. The samples were simply-supported along two opposing edges and impacted with an instrumented drop-weight impact tower. Load vs. time was recorded via strain gauge load cell and the rebound height was captured with an external video system. Velocity was also recorded just prior to contact.

To measure the damage resulting from the impact(s), and ultrasonic NDE method known as C-scan was used. In pulse-echo mode, C-scans are particularly effective at detecting delaminations but lack detail to identify other damage types. Using a commercially available image software, the total area and maximum width (diameter) of the damage is recorded in pixels and scaled to the appropriate dimensions.

To measure the residual properties, standard CAI and flexural tests were used. The flexural method (FAI) was modified to accommodate wide samples with a relatively short support span. The residual compressive strength, flexural strength, and apparent flexural modulus were calculated from the load vs. deflection data with the supplied equations.

Chapter 3

STRESS ANALYSIS OF CAI AND FAI SAMPLES

3.1 Introduction

For this research, a finite element (FE) elastic model will be created to explore the effects of an inclusion caused by an impact on the mechanical properties of a backing panel material. The chapter will outline the development of this model by first addressing the analytical case. The model will be verified using these solutions to ensure that the sensitivity of the model is comparable to known expressions. The in-plane case will first be explored, for which Lekhnitskii's solution [40] of an infinite anisotropic plate with an elastic inclusion has been generally accepted. This model has been simplified by Gillespie *et al.* [41] to give an approximate continuous solution for the distribution of stress near the boundary of a hole in a quasi-isotropic plate. Using failure criteria proposed by Whitney and Nuismer [42], the case of a finite-width plate with a hole is approximated by applying an appropriate correction factor. Both the infinite and finite dimension solutions will be used to validate the accuracy of the model.

In his work, Lekhnitskii also developed a complex variable solution for the bending of an infinite plate. A simple analytical solution analogous to the in-plane load case, though, has not been generally accepted. Therefore, the recent work of three research groups is presented in this chapter. An analytical model for the coupled

stretching-bending of an infinite anisotropic plate with an inclusion of arbitrary stiffness was presented by Cheng and Reddy [43]. Unfortunately, the mathematical solution is intensive and no simple expression has yet been developed. The limiting case of an anisotropic plate with a hole is independently addressed by Hsieh *et al.* [44]. They provide numerical results compared to Leknitskii's solution for an orthotropic plate with a circular hole. Both Cheng and Reddy and Hsieh *et al.* employ a Stroh-like formalism.

Bert and Zeng [45] present results based on Reissner's shear deformable theory on the bending response of a thin, infinite isotropic plate with a circular hole. The results of Bert and Zeng and Hsieh *et al.* are compared to the FE model. Since only recent developments have emerged, there is no consensus on the most applicable analytical flexural solution. Therefore, the data can only be used as a comparison for the model and the in-plane agreement holds as the basic verification method for mesh convergence of the FE model.

3.2 In-Plane Loading

Holes, inclusions, and cracks, intentional or otherwise, can significantly degrade the overall strength of a material structure but are common in most engineering designs and conditions. Analytical solutions have evolved to address these concerns for a variety of loading conditions. The basic solutions for in-plane tensile or compressive loading are generally attributed to the work of Leknitskii [40]. More advanced computer simulation software has since been developed and can reasonably approximate the exact solution with relatively little computation time. However, this finite element solution is inherently approximate and its accuracy can only be measured when compared to the exact solution.

A similar simulation will be generated in this research to approximate the in-plane response of a composite plate, infinite and of finite width, with multiple elliptical inclusions. The derivation of Leknitskii's solution will also be presented so that the computer model may be validated with the exact continuous solution.

3.2.1 Infinite Orthotropic Plate with Inclusion/Hole

Leknitskii's work [40] combines results for the stress state of an anisotropic plate with and without an elliptical hole, to solve the more general case of a plate containing an inclusion of arbitrary stiffness. Leknitskii employed a complex variable method to derive his solution. The inclusion is assumed to be small in comparison to the dimensions of the plate, of the same thickness, and perfectly bonded to the parent material. Arbitrary forces act at the mid-plane around the edges of the plate (Figure 3.1). A brief summary of Leknitskii's solution is initially presented by Monib *et al.* [24] and recapitulated here for convenience.

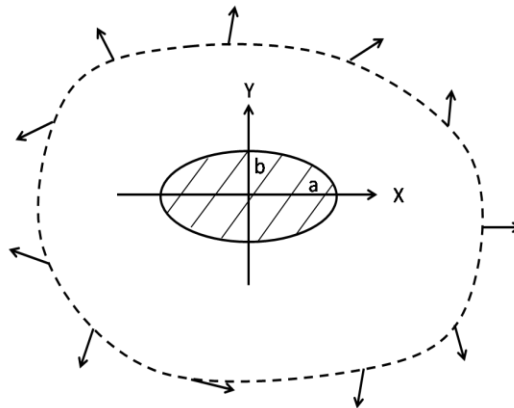


Figure 3.1 An infinite anisotropic plate of arbitrary shape contains an elliptical inclusion and is subjected to in-plane loads at infinity [24].

All variables related to the inclusion will be marked with a prime to distinguish them from the variables of the parent plate. The inclusion is considered to be elliptical and defined by

$$x = a \cos \vartheta, \quad y = b \sin \vartheta, \quad (3.1)$$

where a and b are the major and minor elliptical diameters, respectively, and ϑ is the counterclockwise rotation from the positive x-axis.

The generalized Hooke's law for the parent laminate can be written as follows:

$$\begin{aligned} \varepsilon_x &= a_{11}\sigma_x + a_{12}\sigma_y + a_{16}\tau_{xy}, \\ \varepsilon_y &= a_{12}\sigma_x + a_{22}\sigma_y + a_{26}\tau_{xy}, \\ \varepsilon_z &= a_{16}\sigma_x + a_{26}\sigma_y + a_{66}\tau_{xy}, \end{aligned} \quad (3.2)$$

where a_{ij} represents the elastic constants. Hooke's law for the inclusion is the same but with a_{ij} replaced by a'_{ij} .

Since deformations are assumed to be small, the solution can be approximated by superimposing the stresses of a plate with an elliptical opening. The stress functions for a plate with an inclusion are:

$$\begin{aligned} \sigma_x &= \sigma_x^0 + 2\text{Re}[\mu_1^2 \phi_1'(z_1) + \mu_2^2 \phi_2'(z_2)], \\ \sigma_y &= \sigma_y^0 + 2\text{Re}[\phi_1'(z_1) + \phi_2'(z_2)], \\ \tau_{xy} &= \tau_{xy}^0 - 2\text{Re}[\mu_1 \phi_1'(z_1) + \mu_2 \phi_2'(z_2)], \end{aligned} \quad (3.3)$$

where σ_x^0 , σ_y^0 , and τ_{xy}^0 represent the stress components for a plate with a hole, and z_1 and z_2 are complex variables of the form

$$z_1 = x_1 + iy_1, \quad z_2 = x_2 + iy_2. \quad (3.4)$$

Similarly, the displacement functions of a plate with an inclusion are:

$$\begin{aligned}
u &= u^0 + 2\text{Re}[p_1\phi_1(z_1) + p_2\phi_2(z_2)] - \omega y + u_0, \\
v &= v^0 + 2\text{Re}[q_1\phi_1(z_1) + q_2\phi_2(z_2)] + \omega x + v_0,
\end{aligned} \tag{3.5}$$

where u^0 and v^0 represent the displacement components for a plate containing a hole. The constants ω , u_0 , and v_0 characterize the rigid body displacements and

$$\begin{aligned}
p_k &= a_{11}\mu_k^2 + a_{12} - a_{16}\mu_k, \\
q_k &= a_{12}\mu_k + \frac{a_{22}}{\mu_k} - a_{26}, \\
&(k = 1, 2).
\end{aligned} \tag{3.6}$$

The functions ϕ_1 and ϕ_2 in (3.5) are functions of the complex parameters defined as:

$$\phi_i(z_i) = \frac{dF_i}{dz_i}, \tag{3.7}$$

where F_i is introduced to satisfy the equilibrium conditions. The function, $F(x, y)$, satisfies the differential equation obtained by expressing the deformations in terms of the stress components. μ_1 and μ_2 are the characteristic roots of the resulting equation and are called the complex parameters. The characteristic equation of the plate becomes:

$$a_{11}\mu^2 - 2a_{16}\mu^3 + (2a_{12} + a_{66})\mu^2 - 2a_{26}\mu + a_{22} = 0. \tag{3.8}$$

The complex parameters describe the degree of anisotropy of the material.

Just as for the parent plate, the elastic inclusion contains the stress function F' that is defined by the complex variables $z'_1 = x + \mu'_1 y$ and $z'_2 = x + \mu'_2 y$, where μ'_1 and μ'_2 are the complex parameters for the inclusion. Boundary conditions for the points on the inclusion contour surface can be written as (Figure 3.2):

$$X_n = -X'_n, \quad Y_n = -Y'_n,$$

$$u = u', \quad v = v', \quad (3.9)$$

where X_n and Y_n are external forces and X'_n and Y'_n are forces on the inclusion boundary.

The variables u, v , and u', v' define the rigid body displacements at the contour surfaces.

Transforming the boundary conditions (3.9) results in:

$$\begin{aligned} 2\text{Re}[\phi_1(z_1) + \phi_2(z_2)] &= \frac{\partial(F' - F^0)}{\partial x} + c_1, \\ 2\text{Re}[\mu_1\phi_1(z_1) + \mu_2\phi_2(z_2)] &= \frac{\partial(F' - F^0)}{\partial y} + c_2, \end{aligned} \quad (3.10)$$

$$2\text{Re}[p_1\phi_1(z_1) + p_2\phi_2(z_2)] = u' - u^0 + \omega y - u_0,$$

$$2\text{Re}[q_1\phi_1(z_1) + q_2\phi_2(z_2)] = v' - v^0 + \omega x - v_0.$$

The constants c_1, c_2, ω, u_0 , and v_0 are dependent on the shape of the plate and the force distribution.

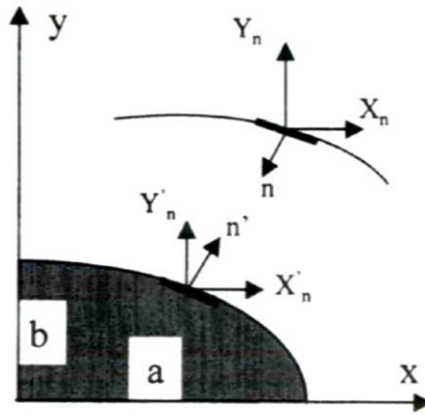


Figure 3.2 Boundary conditions at the inclusion boundary [24]

Solving the boundary conditions in Equation (3.10) allows the functions ϕ_1, ϕ_2 to be evaluated. In turn, the functions can be used to solve the stress and displacement distributions given in Equations (3.3) and (3.5). Figures 3.3 and 3.4 show Leknitskii's solution for a plywood plate containing orthotropic properties and an elliptical inclusion. Three inclusion stiffness values are considered: elastic ($2a_{ij} = a'_{ij}$), rigid ($a'_{ij} = 0$) and a hole ($a'_{ij} = \infty$). It is clear that while a hole contributes no radial stresses, its tangential stress distribution is the largest. By introducing an elastic inclusion, the maximum stress values are reduced and their distributions are altered.

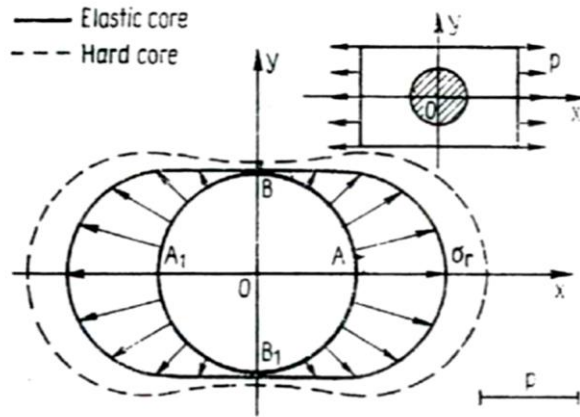


Figure 3.3 Radial stress distribution around a circular hole in a plywood plate under unidirectional tension [40].

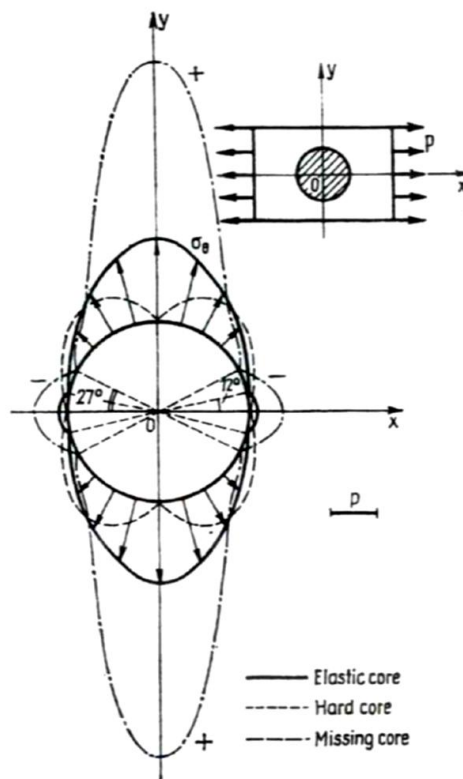


Figure 3.4 Tangential stress distribution around a circular hole in a plywood plate under uniaxial tension [40].

3.2.2 Stress Distribution in an Infinite Width Plate

Whitney and Nuismer [42] and Gillespie *et al.* [41] have shown that Leknitskii's equation for the normal stress distribution in an infinite isotropic plate with a circular hole can be used to derive a good approximation for an orthotropic plate. The stress distribution $\sigma_y^\infty(x, 0)$ ahead of the hole edge, with $x \geq R$ of an infinite orthotropic plate is,

$$\sigma_y^\infty(x, 0) = \frac{\bar{\sigma}_y}{2} \left[2 + \left(\frac{R}{x}\right)^2 + 3 \left(\frac{R}{x}\right)^4 - (K_T^\infty - 3) \left(5 \left(\frac{R}{x}\right)^6 - 7 \left(\frac{R}{x}\right)^8 \right) \right], \quad (3.11)$$

where $\bar{\sigma}_y$ is the far-field applied stress and K_T^∞ is the stress concentration factor for an infinite plate:

$$K_T^\infty = 1 + \sqrt{2 \left(\sqrt{\frac{E_y}{E_x}} - \nu_{yx} + \frac{E_y}{2G_{xy}} \right)}. \quad (3.12)$$

This solution will be used to verify the accuracy of the FE model, which will be later used to simulate the experimental results of both compression and flexure tests. The plate model is composed of shell elements with composite material parameters (Table 3.1). Despite being damaged, the inclusion region will likely retain its original architecture but will suffer degraded mechanical properties. Therefore, the inclusion is modeled as an elliptical shell with the same cross-ply layup and thickness as the parent material but with reduced elastic in-plane moduli. The mesh is composed of triangular elements ([24], [46]) and is refined in proximity of the hole to account for the complex distribution of the local stresses. A convergence analysis was conducted against known solutions in order to verify the accuracy of the mesh density. The average error fell below

3% and a four-fold increase in the number of elements improved the accuracy by only 1.5%.

Table 3.1 Composite properties used for the finite element model.

Ply Construction	Plane-weave
Layup	$[0^\circ/90^\circ/0^\circ/90^\circ]_s$
E_x, E_y	29.50 GPa
E_z	9.80 GPa
$\nu_{xy}, \nu_{yz}, \nu_{xz}$	0.28
G_{xy}, G_{yz}, G_{xz}	3.40 GPa

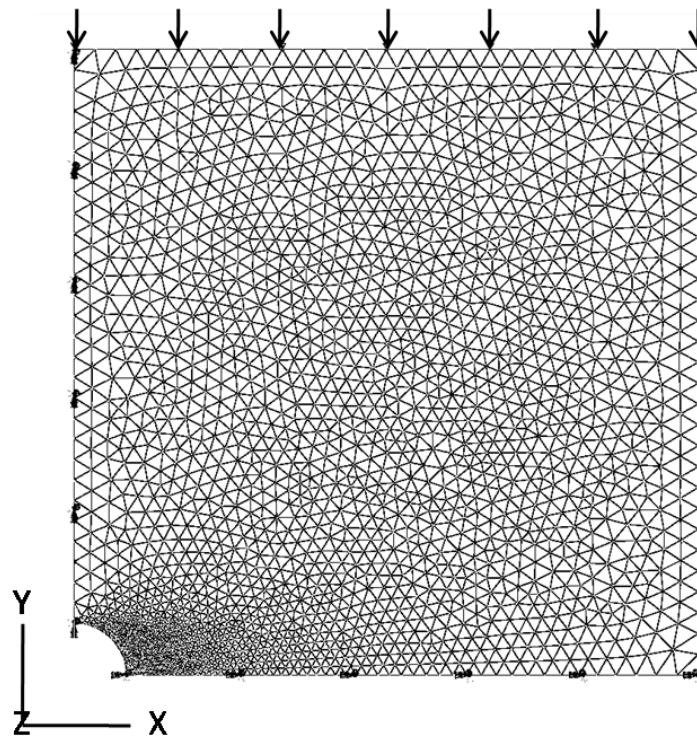


Figure 3.5 Quarter-symmetric in-plane model with refined triangular mesh at the inclusion and inclusion boundary.

The plate and inclusion are modeled in quarter-symmetry since the inclusion is assumed to be located at the center of the plate (Figure 3.5). Symmetric boundary conditions are placed on the x- and y-edges. These prevent translation along the y-axis and rotations about the z- and x-axes for the x-edges, and vice versa for the y-edges. The degrees of freedom along the inclusion boundary are constrained to those of the inner elliptical boundary of the plate. An in-plane edge load is applied to the upper edge of the plate in the negative y-direction to simulate the compressive stress (Figure 3.5).

To verify that the model is accurate, it will be compared to the solutions given for the case of an infinite plate weakened by a circular hole. An infinite plate is one with dimensions much larger than that of the hole, and shows no influence from the stress concentration effect at some distance from the hole. A series of width-to-diameter ratios were analyzed for a variety of hole diameters to determine the ratio at which the stress value at the edges of the plate are constant despite the size of the hole. This distance was found to be twelve times the diameter of the hole as was also used by Monib *et al.* [24]. Figure 3.6 compares the resulting stress distribution from the edge of the hole calculated from Equation (3.11) and the ABAQUS model for the experimental material. The model shows good agreement with the series solution, suggesting that it is suitable for use in further analysis.

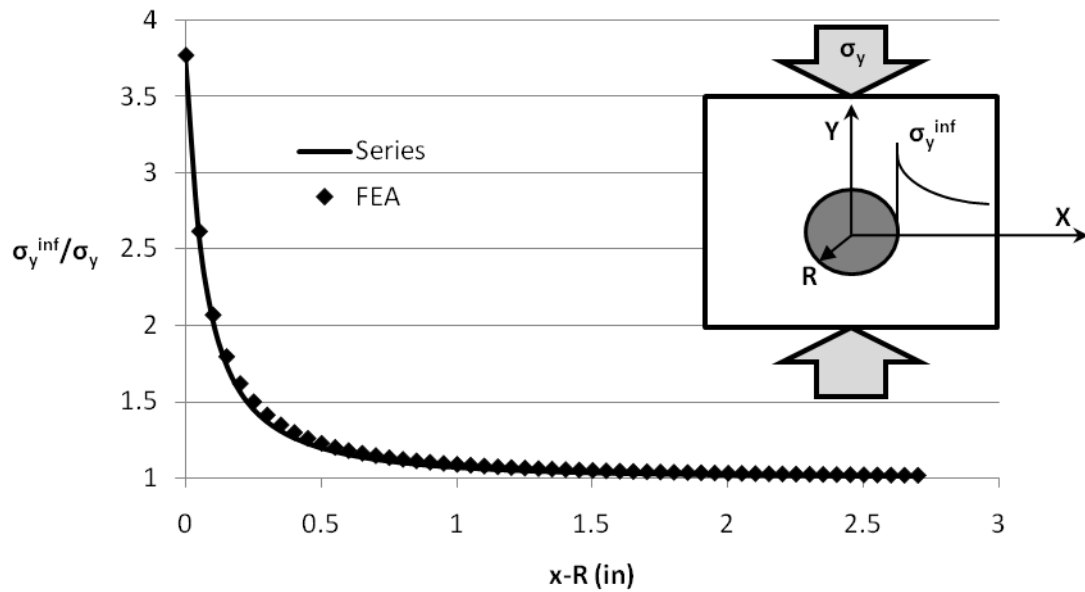


Figure 3.6 FE in-plane stress distribution for experimental backing panel material.

3.2.2 Notched Strength

There is no closed form solution available for the stress distribution in anisotropic plates of finite width with an elastic inclusion, even for the limiting case of an open hole or notch. Rather than using intensive numerical techniques, it is often common practice to apply analytical approximations developed under experimental data. A “finite width correction factor” has been proposed to bridge the gap between experimental strength results and analytical stress fracture criteria.

One common finite width correction factor (FWC) relates notched strength, σ_N , of infinite width plates to that of plates with finite width. This correction simply involves multiplying σ_N by a the factor $\frac{K_T}{K_T^\infty}$, so that:

$$\sigma_N^\infty = \sigma_N \frac{K_T}{K_T^\infty}, \quad (3.13)$$

where K_T is the stress concentration factor in a plate of finite width. K_T^∞ is the stress concentration factor in a plate of infinite width and is dependent on the material properties alone (Equation (3.12)). The finite width correction factor is given by the following approximation:

$$\frac{K_T}{K_T^\infty} = \frac{2 + \left(1 - \frac{D}{W}\right)^3}{3 \left(1 - \frac{D}{W}\right)}. \quad (3.14)$$

Whitney and Nuismer [42] developed a point stress failure criterion (PSC) that suggests failure occurs when the normal stress at some characteristic distance, d_0 , from the hole edge equals the unnotched failure strength of the plate. When this condition is satisfied, the far-field stress is defined as the notched strength, σ_N . Mathematically, the point stress criterion can be written as:

$$\frac{\sigma_N}{X_c} = \frac{\frac{2K_T^\infty}{K_T}}{2 + \xi^2 + 3\xi^4 - (K_T^\infty - 3)(5\xi^6 - 7\xi^8)}, \quad (3.15)$$

where

$$\xi = \frac{R}{R + d_0}. \quad (3.16)$$

The PSC model has been shown to give good agreement with experimental results. Whitney and Nuismer also concluded that the characteristic distance ahead of the hole may depend on the hole dimensions. However, Equations (3.15) and (3.16) logically predict a continuous decrease in notched strength with an increase in hole radius, or as $\xi \rightarrow 1$. Thus for large holes, the characteristic distance can be considered negligible

compared to the radius and the notched strength equals the unnotched strength divided by the FWC (Equation (3.15)).

3.2.3 Finite Orthotropic Plate with Hole

Equation (3.13) assumes that the stress profile of a finite width plate scale with the parameter $\frac{K_T}{K_T^\infty}$. Thus, the distribution of a finite plate is simply scaled from the solution for an infinite plate:

$$\frac{\sigma_y(x, 0)}{\sigma_y^\infty(x, 0)} = \frac{K_T}{K_T^\infty} = \text{constant}. \quad (3.17)$$

Using Equation (3.11) and (3.17) yields the approximate stress distribution near the hole:

$$\frac{\sigma_y^\infty(x, 0)}{\bar{\sigma}_y} = \frac{1}{2} \frac{K_T}{K_T^\infty} \left[2 + \left(\frac{R}{x}\right)^2 + 3 \left(\frac{R}{x}\right)^4 - (K_T^\infty - 3) \left(5 \left(\frac{R}{x}\right)^6 - 7 \left(\frac{R}{x}\right)^8 \right) \right], \quad (3.18)$$

where $\bar{\sigma}_y$ is the far-field applied stress on the finite width panel.

Since the samples used in this research are of finite width containing a region of damaged material, the substantiated infinite model will be reduced to a finite width plate. An approximate closed-form solution for the stress distribution in a finite width plate with a hole is given in Equation (3.18). The stress concentration factor, K_T , of the experimental material for various holes sizes is presented in Figure 3.7. For finite widths, K_T is larger than K_T^∞ (3.77), but decreases asymptotically to K_T^∞ as the hole size diminishes (for a constant width). Figure 3.7 also shows the infinite plate threshold value of $W/D = 12$. A finite width model composed of the experimental material is verified against the analytical solution for a plate width-to-diameter ratio of 3, $W/D = 3$. Figure

3.8 shows that the FE model matches the analytical solution well, so it is with confidence that the developed model can be applied to the current study.

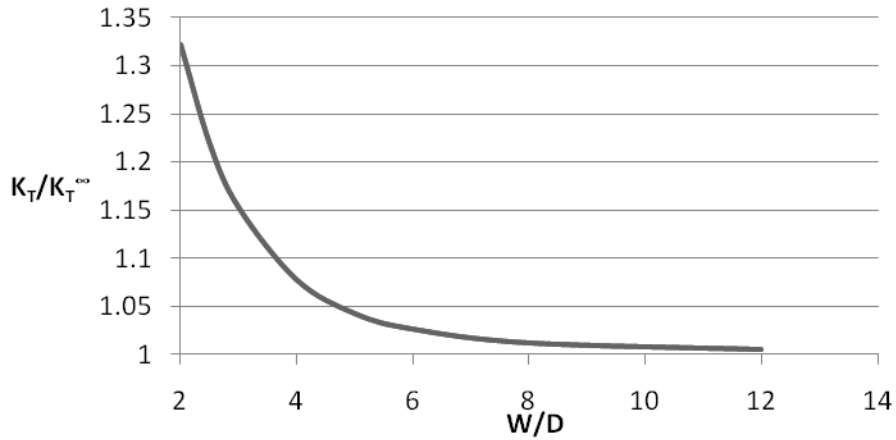


Figure 3.7 The effect of hole diameter on the stress concentration in a finite plate containing the experimental material.

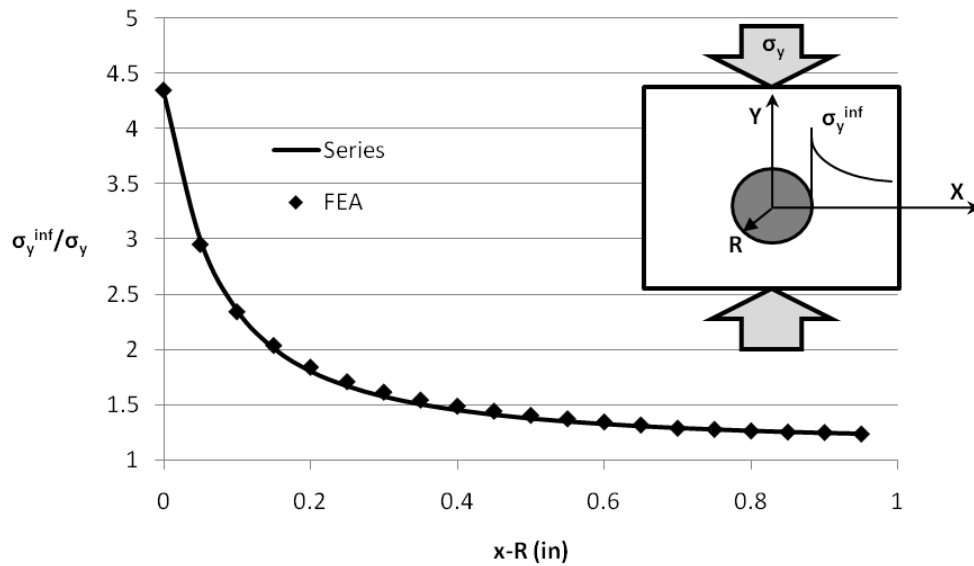


Figure 3.8 Stress distribution of finite width experimental material composite material: $W/D=3$.

3.2.4 Finite Orthotropic Plate with Orthotropic Inclusion

While Leknitskii has generated an exact solution for the in-plane stresses of an infinite plate with an elastic inclusion, there exists no solution for an inclusion within a finite width plate. To compensate, the finite element model validated above will be used to visualize the effects of the inclusion diameter-to-plate width ratio and inclusion stiffness on the stress distributions of a finite plate.

The damage region induced by the out-of-plane impact loading is idealized as an elliptical orthotropic inclusion. The inclusion is assumed to retain a fraction of the undamaged material stiffness. In the case of an open hole the inclusion has zero stiffness and the solution reduces to the analytical solution for an open hole given above. Figure 3.9 is constructed to explore the effect of inclusion diameter and stiffness on the stress concentration in a finite plate. For small inclusion diameters, however, the parent plate may be considered infinite. If the inclusion has no stiffness, then the stress concentration at the edge of the hole becomes K_T^∞ for small diameters. From Figure 3.9 this value is 3.77, which is also shown in Figure 3.6. As the inclusion stiffness increases, however, its load carrying capacity distributes the stress. The stress becomes uniformly distributed when the inclusion stiffness is equivalent to that of the parent plate, eliminating the stress concentration. For larger inclusion sizes, the finite distance between the edge of the inclusion and the edge of parent plate begins to affect the stress distribution. The resulting concentration is larger than for an infinite plate with the same inclusion. The magnitude of this concentration, however, is similarly influenced by the inclusion

stiffness: maximum concentration will occur for a hole, and there will be no concentration for an inclusion stiffness equal to that of the parent plate.

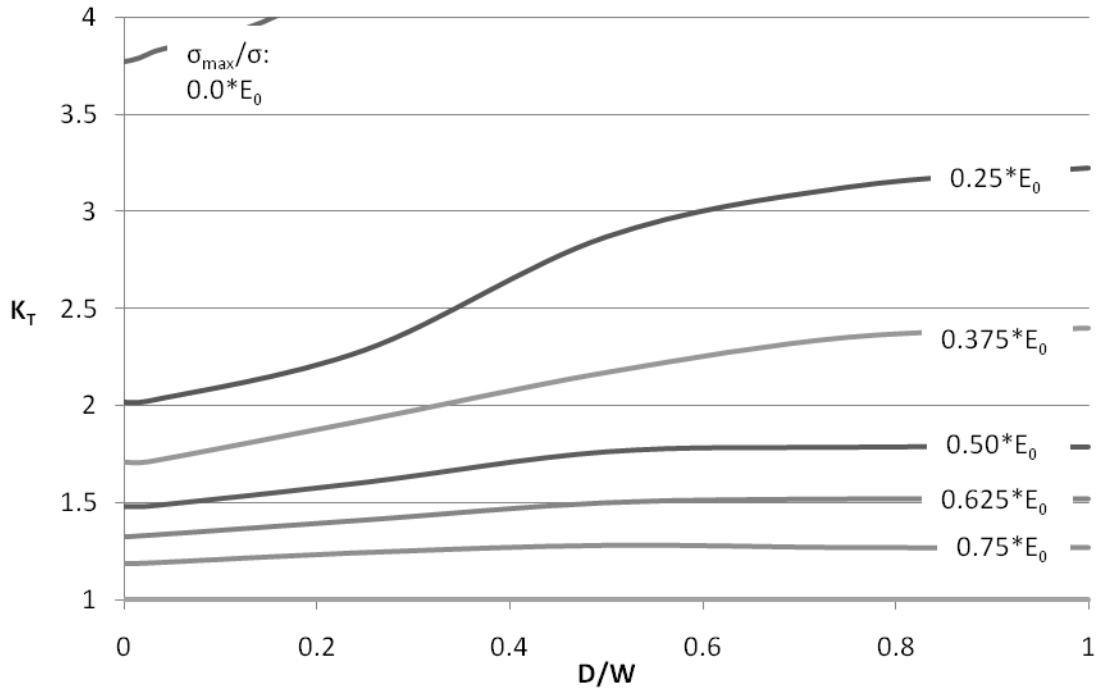


Figure 3.9 Effect of inclusion stiffness and damage width on the in-plane stress concentration of a finite width plate with a central inclusion.

In addition to size and stiffness, it is expected that the proximity of multiple inclusions will influence the stress distribution in a finite plate. Figure 3.10 plots the concentration of stress against the distance between the centers of the inclusions. The inclusions were assumed to have the same size and stiffness, so a quarter-symmetry model was again used. It is clear for large separation distances that the stress concentration shows little variation. As the inclusions begin to overlap, however, the

stress distributions begin to interact and the concentrations rapidly increase. This is true for inclusions with no stiffness (hole) and stiffness 75% of the parent plate. Intermediate stiffness values follow the same trend with proportional rates of change.

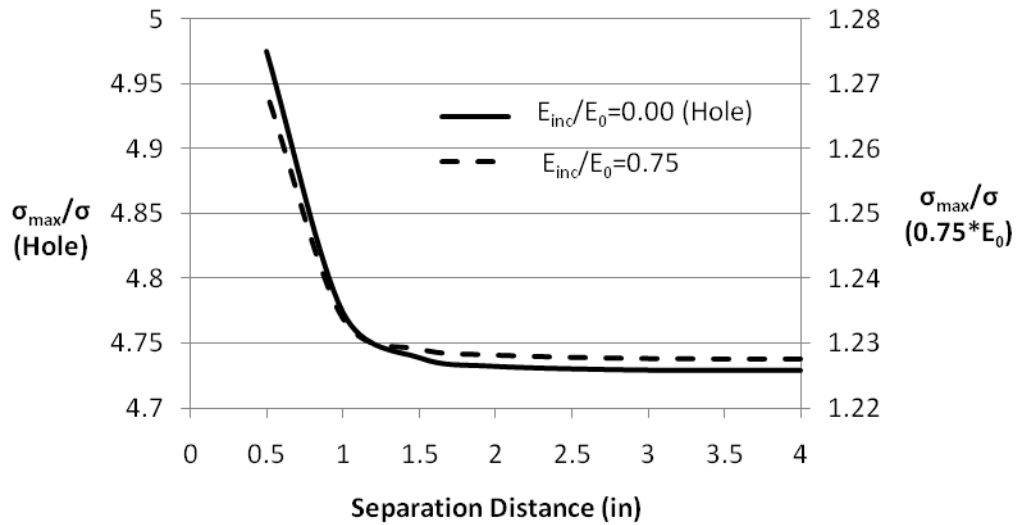


Figure 3.10 As the inclusions approach one another the maximum in-plane stress concentration at their edges begins to significantly increase.

A 2in separation distance was chosen for experimental testing to produce multiple damage sites that do not interact. A design chart similar to Figure 3.9 is constructed to investigate the effect of size and stiffness of multiple inclusions on the distribution of stress in a finite plate. When compared to the central inclusion (Figure 3.9), the stiffness curves in Figure 3.11 experience a more drastic transition slope as they approach higher stress concentrations. It can be expected that with more material in the plate with reduced properties, the surrounding parent material is forced to distribute the additional stress. For low-stiffness inclusions, much of the area between the inclusions will transmit little

stress. However, the load carrying capacity of the plate is less sensitive to the diameter of the hole in the length direction than it is in the width direction. So, the concentration factors for the central inclusion and separated inclusions may not be expected to differ drastically (Figure 3.12).

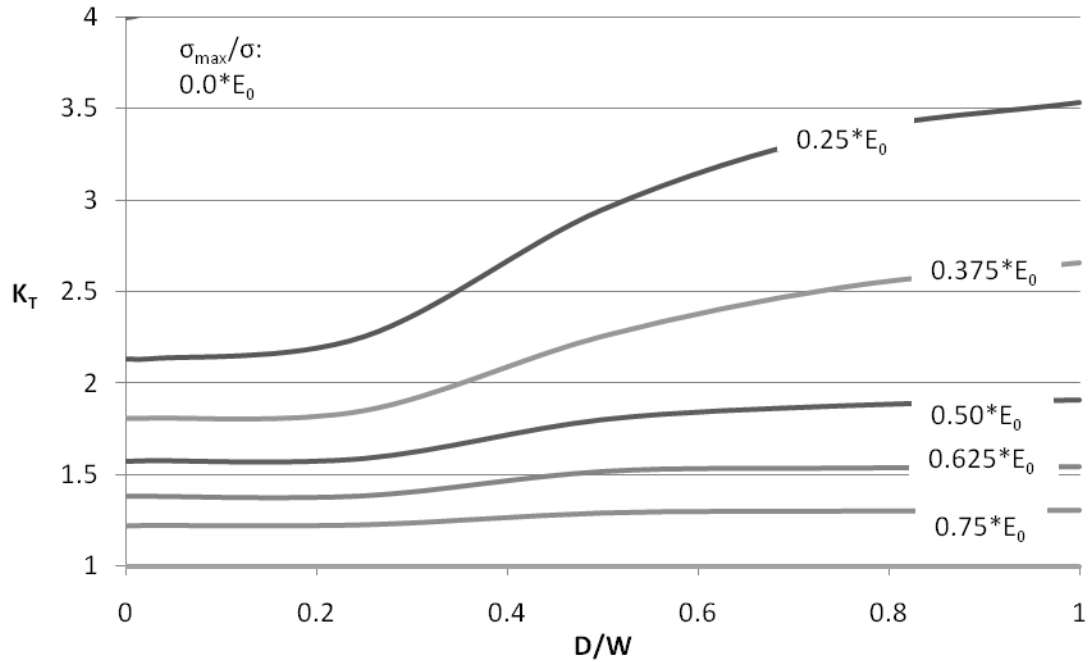


Figure 3.11 Effect of inclusion stiffness and damage width on the in-plane stress concentration of a finite width plate with two inclusions separated by 2in.

Figure 3.12 gives the in-plane stress contour plot for a single and multiple holes with $W/D = 4$. It is easy to see that stress magnitude at the edge of the displaced hole is only slightly larger than that of the central hole (15.0% difference), and that much of the area below the displaced hole transmits little load. The effective modulus of both cases is

simply the in-plane stress divided by the longitudinal strain; the longitudinal strain is defined as the change in length divided by the length of the plate in the y-direction (6in). The modulus of the single hole is approximately 2.20Msi (versus the no-hole baseline of 2.50 Msi), whereas the modulus of the separated holes is 2.01Msi. This represents a percent difference of only 9%. Considering that the actual damage site will likely retain some mechanical stiffness, it appears sensible to have not measured the effective compressive modulus during the experimental tests.

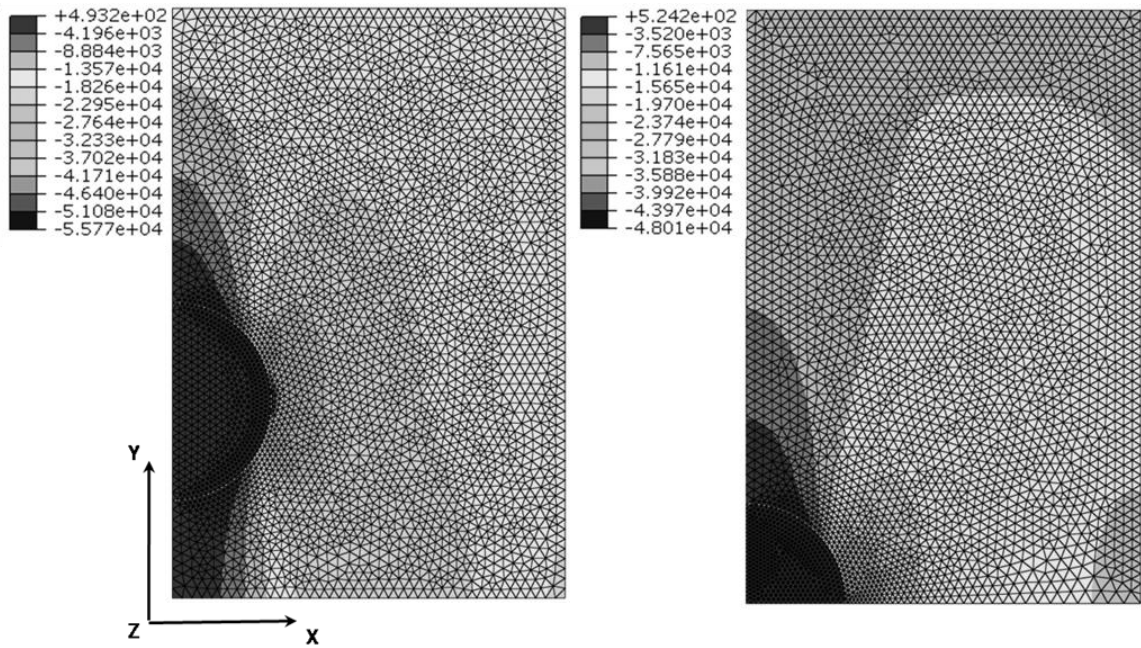


Figure 3.12 The in-plane stress concentrations and moduli for samples with a single central inclusion and symmetrically displaced inclusions are similar.

The FE model developed in this section will also be used to visualize the effect of an idealized damaged inclusion on the response of a finite composite plate during FAI.

Experimental values will be used to determine the inclusion stiffness and its relationship to the diameter. The particular combination of stiffness and diameter will produce stress concentrations that may reasonably approximate the strength loss during the actual flexural tests. Converting these models into in-plane conditions will also extrapolate FE results that may be compared to experimental CAI values. If a reasonable correlation exists, it may be possible to model complex composite damage as a simple elastic elliptical inclusion and reasonably predict the post-impact mechanical response.

3.3 Bending Loads

Although the hole/crack/inclusion problems are very important in engineering applications, most of the analytical solutions are devoted to the two-dimensional case. Very few analytical solutions are found in literature for bending considerations, the most predominant of which is the work of Leknitskii [40]. In 1968 Leknitskii presented his work on the bending of an orthotropic plate weakened by a circular hole, and little progression from his work or otherwise has been developed. Since the boundary conditions for the hole problem is not easily satisfied with the conventional methods of plate bending theory, Leknitskii employed a complex variable method. Advancement in methodology came when Leknitskii's formulation in anisotropic elasticity was connected to a formalism independently developed by Stroh [47]. However, recent contributions remain limited.

3.3.1 Infinite Orthotropic Plate with Orthotropic Inclusion

Most existing two-dimensional analyses are devoted to plane stress, generalized plane strain, or pure bending problems of an anisotropic plate with a stress singularity ([40], [47]). Recently, Cheng and Reddy [43] have established an octet formalism for coupled stretching and bending deformations of an inhomogeneous and laminated anisotropic elastic thin plate. The new formalism is shown to possess many of the elegant properties that have been found in the Stroh sextic formalism for generalized plane strain problems ([47], [48]).

The through-thickness orthotropic elliptic inhomogeneity is contained in a composite laminated thin plate subjected to uniform loading at infinity. The generalized displacement vector and the stress function vector have the following solution,

$$u \equiv af(z), \quad \phi \equiv bf(z), \quad (3.19)$$

where f is an arbitrary function of $z = x_1 + px_2$. a and b are eigenvectors with eigenvalue p are determined by the standard eigenrelation

$$\begin{bmatrix} N_1 & N_2 \\ N_3 & N_1^T \end{bmatrix} \begin{bmatrix} a \\ b \end{bmatrix} = p \begin{bmatrix} a \\ b \end{bmatrix}. \quad (3.20)$$

The matrix N composed of N_1 , N_2 and N_3 is same as the fundamental elasticity matrix in Stroh's sextic formalism for generalized plane strain problems.

Because four pairs of complex conjugates for the eigenvalue, p , can be solved, the associated eigenvectors are also four pairs of complex conjugates. If each pair are distinct, the general solution for the generalized displacements and stress functions are obtained by superposing eight solutions as

$$u = \sum_{K=1}^4 \{a_K f_K(z_K) + \bar{a}_K f_{K+4}(\bar{z}_K)\}, \quad (3.21)$$

$$\phi = \sum_{K=1}^4 \{b_K f_K(z_K) + \bar{b}_K f_{K+4}(\bar{z}_K)\},$$

where f_K and f_{K+4} are eight arbitrary functions of their arguments, $z_K = x_1 + p_K x_2$. For a given boundary value problem, the unknown functions $f_K(z_K)$ and $f_{K+4}(\bar{z}_K)$ remain to be determined by the boundary conditions.

In this work, the coupled stretching and bending deformations of an anisotropic plate containing an elliptic inhomogeneity are investigated. It is assumed that $N_{\alpha\beta}$, $M_{\alpha\beta}$, $e_{\alpha\beta}$ and $\kappa_{\alpha\beta}$ are known. When the membrane stress resultants at infinity ($N_{\alpha\beta}$) and bending moments ($M_{\alpha\beta}$) are uniform, the in-plane strains ($e_{\alpha\beta}$) and curvatures ($\kappa_{\alpha\beta}$) are also uniform. The inclusion is defined by the tangential vector n and normal vector m of the elliptic boundary Γ (Figure 3.13).

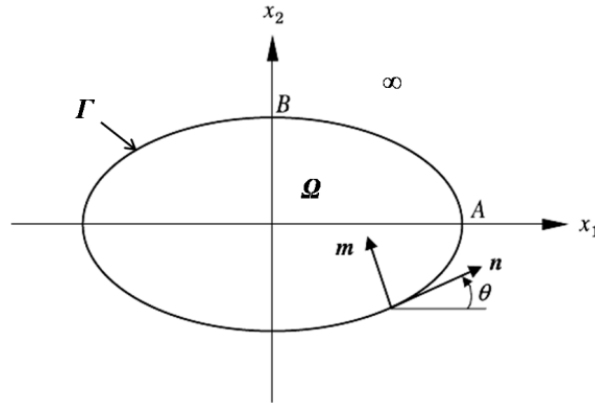


Figure 3.13 Coordinates at the inclusion boundary of an anisotropic plate under coupled bending-stretching [43].

The solution outside the elliptic inhomogeneity is assumed to be

$$\begin{bmatrix} u \\ \phi \end{bmatrix} = x_1 \begin{bmatrix} \varepsilon_1^\infty \\ t_2^\infty \end{bmatrix} + x_2 \begin{bmatrix} \varepsilon_2^\infty \\ -t_1^\infty \end{bmatrix} + 2\text{Re} \begin{bmatrix} A\langle z_* \rangle B^T & A\langle z_* \rangle A^T \\ B\langle z_* \rangle B^T & B\langle z_* \rangle A^T \end{bmatrix} \begin{bmatrix} \varepsilon_1^\infty \\ t_2^\infty \end{bmatrix}, \quad (3.22)$$

where A and B are matrices composed of the eigenvectors a and b , respectively. The solution inside the inhomogeneity is assumed as

$$\begin{bmatrix} u^\Omega \\ \phi^\Omega \end{bmatrix} = x_1 \begin{bmatrix} \varepsilon_1^\Omega \\ t_2^\Omega \end{bmatrix} + x_2 \begin{bmatrix} \varepsilon_2^\Omega \\ -t_1^\Omega \end{bmatrix}, \quad (3.23)$$

where ε_1 and ε_2 are functions of the in-plane strains and curvatures and t_1 and t_2 are composed of the applied in-plane loads and moments. Superscript ∞ refers to the loading at infinity. Superscript Ω refers to the inside of the ellipse, where the membrane stress resultants and bending moments are uniform. This is consistent with the uniformity property of the Eshelby [48] inclusion problem in three-dimensional elasticity. The real vectors g , h , ε_1^Ω and t_2^Ω (or ε_2^Ω and t_1^Ω) are determined by the continuity condition across the elliptic boundary.

An important limit case is when the elliptic inhomogeneity becomes an elliptic hole. Rewriting (3.23) at the elliptic boundary, the displacement and stress functions at the edge of the hole can be found. From them, the hoop bending moment is found to be

$$\begin{aligned} M_{nn}^r &= -[0 \quad n^T] \frac{\partial \phi}{\partial x_2^*} \Big|_r \\ &= \cos \theta [0 \quad n^T] \left[t_1^\infty + G_1(\theta) t_2^\infty + \frac{b}{a} G_3(\theta) t_1^\infty \right] \\ &\quad + \sin \theta [0 \quad n^T] \left[t_2^\infty - G_1(\theta) t_1^\infty + \frac{a}{b} G_3(\theta) t_2^\infty \right]. \end{aligned} \quad (3.24)$$

If the plate is subjected to M_{22}^∞ only, $t_1^\infty = 0$ and $t_2^\infty = M_{22}^\infty i_4$, then the concentration factors of hoop bending moment at points A and B (Figure 3.13) are

$$\frac{M_{nn}^A}{M_{22}^\infty} = 1 + \frac{a}{b} \left[G_3 \left(\frac{\pi}{2} \right) \right]_{44}, \quad \frac{M_{nn}^B}{M_{22}^\infty} = [G_1(0)]_{34}. \quad (3.25)$$

where the functions $G_1(\theta)$ and $G_3(\theta)$ are related to the fundamental elasticity matrix, N , through a series of matrix conversions.

Cheng and Reddy provide an exact closed-form solution for an elliptic inhomogeneity in a laminated anisotropic elastic thin plate subjected to remote uniform membrane stress resultants and bending moments. Displacements, slopes, surface and hoop stress resultants along the elliptic boundary are readily obtained in a real form.

Although the properties of this formalism resemble that of Stroh's, plate bending problems cannot be solved by the Stroh formalism. The Stroh formalism is applied to an elastic body with a thickness approaching infinity, which considers generalized plane strain. Mathematically, it is exact within the context of elasticity theory for classical Cauchy medium. Cheng and Reddy's work applies to a thickness approaching infinitesimal and is exact within the context of the classical plate theory. However, both formalisms are approximate from the viewpoint of a higher-order elasticity theory [43].

3.3.2 Infinite Orthotropic Plate with Hole

Hsieh *et al.* [44] developed a Stroh-like formalism that considers an infinite anisotropic plate with an elliptical hole. This is presented as the limiting case of inclusion with no stiffness. The governing equation combines the Kirchhoff plate assumptions,

equilibrium equations, constitutive laws, and the kinematic relations. It can be expressed in terms of the mid-plane lateral deflection w as [49]

$$D_{11} \frac{\partial^4 w}{\partial x^4} + 4D_{16} \frac{\partial^4 w}{\partial x^3 \partial y} + 2(D_{12} + 2D_{66}) \frac{\partial^4 w}{\partial x^2 \partial y^2} + 4D_{26} \frac{\partial^4 w}{\partial x \partial y^3} + D_{22} \frac{\partial^4 w}{\partial y^4} = q, \quad (3.26)$$

where q is the lateral load distribution and D_{ij} is the bending stiffness of the plate. The deflection w can be determined by solving this partial differential equation and satisfying the relevant boundary conditions. After finding the deflection, all the other physical values such as the in-plane displacements (u, v), bending moments (M_x, M_y, M_{xy}), transverse shear forces (Q_x, Q_y), and internal stresses ($\sigma_x, \sigma_y, \tau_{xy}$) can all be obtained through the use of their relations with the deflection.

In order to solve the problems with hole/crack/inclusion boundaries, a Stroh-like complex variable formalism for the bending theory of anisotropic plates will be used. In this formalism, the general solution satisfying the governing Equation (3.26) can be expressed as follows

$$w = w_0 + 2\text{Re}\{c_1 w_1(z_1) + c_2 w_2(z_2)\}, \quad (3.27)$$

where Re stands for the real part of a complex number. w_0 is a particular solution of Equation (3.26), whose form depends on the load distribution q over the plate surface, and $w_1(z_1)$ and $w_2(z_2)$ are arbitrary analytic functions of complex variables.

By introducing the stress function vector ϕ and the slope vector α and using the general solution (3.27), a Stroh-like formalism has been developed as

$$\phi = \phi_0 + 2\text{Re}\{Aw'(z)\}, \quad \alpha = \alpha_0 + 2\text{Re}\{Bw'(z)\}, \quad (3.28)$$

where ϕ_0 and α_0 are the particular solutions related to the lateral load distribution q .

Consider an unbounded anisotropic plate weakened by an elliptical hole subjected to out-of-plane bending moments $M_x = \hat{M}_x$, $M_y = \hat{M}_y$, and $M_{xy} = 0$ at infinity (Figure 3.14). There is no load around the edge of the elliptical hole. Thus, the boundary condition can be expressed in terms of the stress function as

$$\begin{aligned}\phi &= -\hat{M}_x i_2 - \hat{M}_y i_1 \quad \text{at infinity,} \\ \phi &= 0 \quad \text{along the hole boundary.}\end{aligned}\tag{3.29}$$

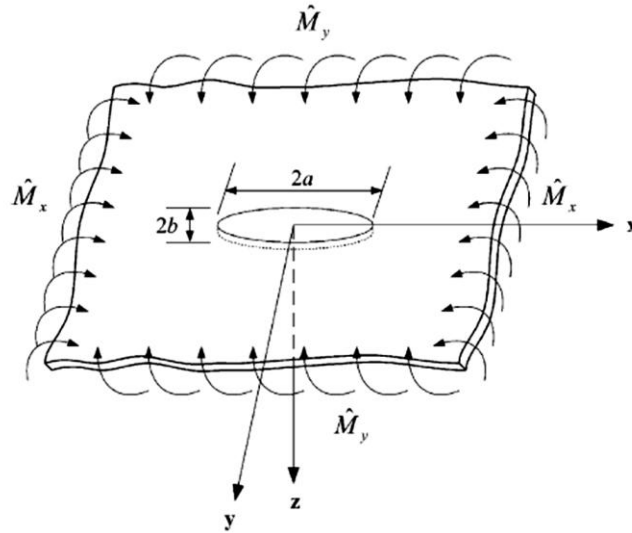


Figure 3.14 Biaxial bending of an infinite anisotropic plate with an elliptical hole [44].

Since there is no lateral load applied on the plate, i.e., $q = 0$, the particular solutions ϕ_0 and α_0 are zero. By satisfying the free edge condition the derivative of the displacement

function can be found. With this expression, the explicit solution of the present problem can be expressed as

$$\begin{aligned}\phi &= \phi^\infty + \operatorname{Re}\{A\langle\zeta_k^{-1}\rangle A^{-1}(a\widehat{M}_y i_1 + ib\widehat{M}_x i_2)\}, \\ \alpha &= \alpha^\infty + \operatorname{Re}\{B\langle\zeta_k^{-1}\rangle A^{-1}(a\widehat{M}_y i_1 + ib\widehat{M}_x i_2)\},\end{aligned}\quad (3.30)$$

where ϕ^∞ and α^∞ are added to satisfy the boundary conditions at infinity. The explicit solution found in (3.30) can be used to determine the deflection, bending moments, and transverse shear forces in response to the applied moments.

To obtain the explicit solutions for the moments around the elliptical hole boundary, the stress and slope functions must be differentiated with respect to s and n :

$$\begin{aligned}\phi_{,s} &= 0, \\ \phi_{,n} &= -\widehat{M}_x \left\{ \cos \theta E_1 \left(\theta - \frac{\pi}{2} \right) + \sin \theta \left[I + \frac{b}{a} F_1 \left(\theta - \frac{\pi}{2} \right) \right] \right\} i_2 \\ &\quad + \widehat{M}_y \left\{ \sin \theta E_1 \left(\theta - \frac{\pi}{2} \right) + \cos \theta \left[I + \frac{a}{b} F_1 \left(\theta - \frac{\pi}{2} \right) \right] \right\} i_1,\end{aligned}\quad (3.31)$$

where $E_1(\theta)$ and $F_1(\theta)$ are matrices composed of the fundamental elastic matrices, $N_i(\theta)$.

While no explicit closed form solution has been found for the above case, Leknitskii presented a solution for the special case of an orthotropic plate weakened by a circular hole [40]. So, for an anisotropic plate weakened by a circular hole with radius a subjected to $M_x = \widehat{M}$, $M_y = M_{xy} = 0$, the explicit solution (48) can be reduced to

$$\begin{aligned}\phi &= \phi^\infty - a\widehat{M}\operatorname{Im}\{A\langle\zeta_k^{-1}\rangle A^{-1}\}i_2, \\ \alpha &= \alpha^\infty - a\widehat{M}\operatorname{Im}\{B\langle\zeta_k^{-1}\rangle A^{-1}\}i_2.\end{aligned}\quad (3.32)$$

These functions can be used to find the expression for the derivative of the deflection, w . Through simple integration, the result is found to be identical to that shown by Leknitskii [40].

Leknitskii's work was used to verify the solution for the moment distributions by considering the special case of an orthotropic plate with a circular hole. To show the generality of the solution, results were obtained for anisotropic plates of different ply orientations with a circular hole. Figure 3.15 shows the moment distributions for each ply angle. It can be noted that the maximum value of M_t occurs at points on the hole edge through an axis perpendicular to the fiber direction. Moreover, the maximum value of M_t decreases when the fiber orientation increases.

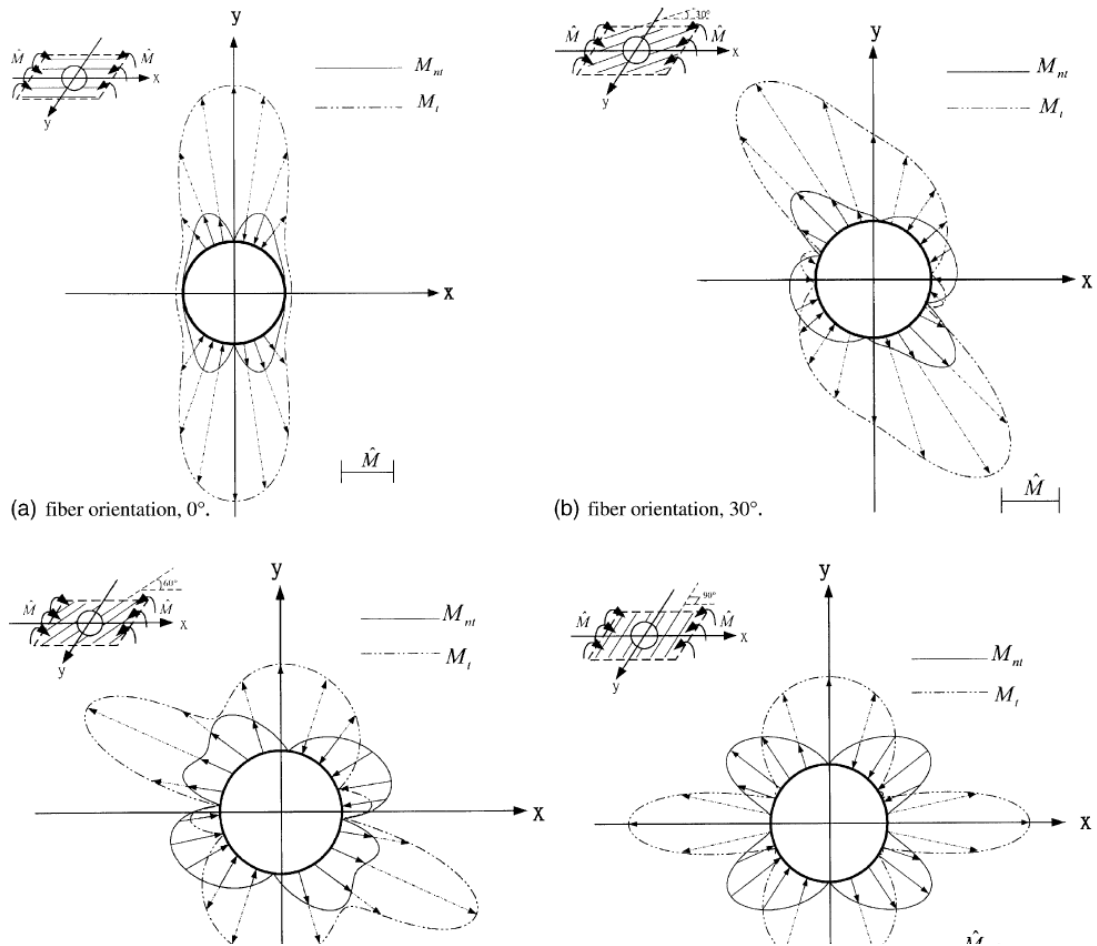


Figure 3.15 Distribution of moment component concentrations around a circular hole in a orthotropic plate under uniaxial bending for fiber orientations of (a) 0°, (b) 30°, (c) 60°, and (d) 90° [44].

Though no accessible closed-form solution is given, numerical results are presented by Hsieh *et al.* [44] for the above condition. These values can be compared to the results of the in-plane FE model validated in Section 3.2 in order to gauge its usability as a flexural model. To accommodate the flexural conditions, a uniaxial edge moment is applied to the plate boundary to simulate the bending load at infinity. Hsieh *et al.* present

the concentration factors of the tangential bending components around the boundary of a hole in an infinite orthotropic plate loaded by out-of-plane bending moment, M_x . The exact plate properties considered are given in Table 3.2. At angles 0° and 90° from the y-axis, the tangential bending component becomes M_y and M_x , respectively. It is at these points the FE model can be verified (Table 3.3). Their results were also compared to the solution provided by Lekhnitskii [40].

Table 3.2 The orthotropic properties used by Hsieh *et al.* [44] are applied to the FE model to compare the results.

Ply Construction	Unidirectional
Layup	0°
Plate Thickness, h	3 mm
E_1	181 GPa
E_2	10.3 GPa
ν_1	0.28
G	7.17 GPa

Table 3.3 Tangential moment concentration for an infinite orthotropic plate around the boundary of a circular hole [44].

Angle ψ	M_t/M_x		
	Hsieh	Lekhnitskii	Current Model
0°	0.1370	0.1369	0.1354
15°	0.1508	0.1507	
30°	0.2112	0.2112	
45°	0.4170	0.4170	
60°	1.1192	1.1193	
75°	2.5062	2.5062	
90°	3.0568	3.0566	3.1511

Table 3.3 shows the FE model to have good agreement with the Hsieh and Lekhnitskii solutions. The significance of this result is limited since only two locations could be verified and the material properties are different than those used throughout this research. Thus, while encouraging, this correlation cannot be solely used to argue the accuracy of the model.

3.3.3 Infinite Isotropic Plate with Hole

Reissner [50] developed a bending theory of elastic plates that accounts for transverse shear deformation effects, which is neglected in classical thin plate theory. He discussed the problem for a hole in a large isotropic plate. Zeng and Bert ([51], [45]) have developed a solution that addresses an infinite isotropic plate with a circular elastic inclusion.

The elastic inclusion is also considered shear-deformable with the same thickness as the plate. Let subscripts 1 and 2 refer to the plate and the inclusion, respectively. The governing system of equations for the problem is

$$\begin{aligned} D\nabla^4 w &= 0, \\ \nabla^2 \chi - \lambda^2 \chi &= 0, \end{aligned} \tag{3.33}$$

where w is the out-of-plane deflection and χ is a shear deformation function that satisfies three boundary conditions along the edge of the plate instead of two Kirchhoff conditions.

Bert and Zeng also considered generalized bending with principal moments M_x and M_y , the ratio of which is defined as $B = M_y / M_x$. For uniaxial bending and balanced biaxial bending, $B = 0$ and 1, respectively. Polar coordinates were used to account for the

inclusion geometry with radius a (Figure 3.16). At infinity, the plate is subjected to biaxial bending moments M_x and M_y , which in polar coordinates gives

$$M_r = \frac{M_x}{2} [(1+B) + (1-B) \cos(2\theta)]; \quad M_{r\theta} = -\frac{M_x}{2} (1-B) \sin(2\theta); \quad Q_r = 0. \quad (3.34)$$

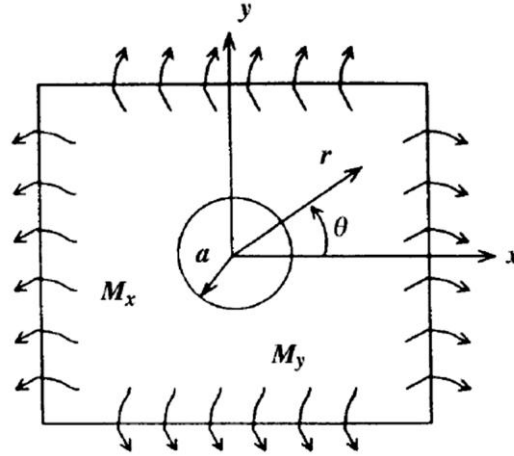


Figure 3.16 Generalized bending of an infinite isotropic plate with a circular hole [51].

Applying these conditions to the governing equations gives the general solution outside the inclusion.

$$w_1(r, \theta) = c_1 + c_2 \ln\left(\frac{r}{a}\right) + c_3 \frac{r^2}{a^2} + \left(d_2 \frac{a^2}{r^2} + d_3 \frac{r^2}{a^2} + d_4\right) \cos(2\theta), \quad (3.35)$$

$$\chi_1(r, \theta) = C_0 K_0(\lambda r) + [C_2 \cos(2\theta) + G_2 \sin(2\theta)] K_2(\lambda r).$$

Regularity conditions require that moments be finite at the center of the inclusion ($r = 0$). Therefore, the solutions inside the inclusion are

$$w_2(r, \theta) = c'_1 + c'_3 \frac{r^2}{a^2} + \left(d'_1 \frac{r^4}{a^4} + d'_3 \frac{r^2}{a^2} \right) \cos(2\theta), \quad (3.36)$$

$$\chi_2(r, \theta) = A'_0 I_0(\lambda r) + [A'_2 \cos(2\theta) + B'_2 \sin(2\theta)] I_2(\lambda r),$$

where I_m and K_m are the first and second kinds of modified Bessel function with order m .

The coefficients and constants can be determined by satisfying the boundary conditions at the inclusion-plate interface, $r = a$:

$$\begin{aligned} w_1 &= w_2, \quad \phi_{r1} = \phi_{r2}, \quad \phi_{\theta1} = \phi_{\theta2}, \\ M_{r1} &= M_{r2}, \quad M_{r\theta1} = M_{r\theta2}, \quad Q_{r1} = Q_{r2}. \end{aligned} \quad (3.37)$$

Assuming no initial deflection of the inclusion before the bending loads are applied (i.e., let $c'_1 = 0$) results in 13 unknowns and 13 independent equations. Therefore, all the constants can be determined. Among the solutions, A'_0 , C_0 , A'_2 , and C_2 are zero. After simplifying, the radial and circumferential bending moments at the interface in the plate and inclusion can be expressed

$$\begin{aligned} M_{\theta1} &= \left\{ \frac{D_1}{a^2} [c_2(\nu_1 - 1) - 2c_3(\nu_1 + 1)] \right\} \\ &+ \left\{ \frac{1}{a^2} [2D_1(3d_2 + d_3)(\nu_1 - 1) + d_4] \right. \\ &\left. + \frac{1}{\mu^2} \left[4G_2 K_2(\mu) (\mu K K(\mu) - 1) + \frac{48d_4 D_1}{a^2} \right] \right\} \cos(2\theta), \end{aligned}$$

$$\begin{aligned}
M_{\theta 2} = & \left\{ \frac{-2k_D D_1 c_3'}{a^2} (v_2 + 1) \right\} \\
& - 2 \left\{ \frac{1}{a^2} [k_D D_1 (d_3' (v_2 - 1) + 6d_1' v_2)] \right. \\
& \left. + \frac{1}{\mu^2} \left[2B_2 I_2(\mu) (\mu I I(\mu) - 1) - \frac{24d_1' k_D D_1}{a^2} \right] \right\} \cos(2\theta).
\end{aligned} \tag{3.38}$$

For an inclusion with no stiffness, a hole, the conditions at boundary $r = a$ are

$$M_r = M_{r\theta} = Q_r = 0, \tag{3.39}$$

allowing c_2 , d_2 , d_4 , and G_2 to be solved. The nonzero coefficients become c_2 , c_3 , d_2 , d_3 , d_4 , G_2 , and c_1 , which can be any constant. Therefore the solution for $\chi(r, \theta)$ can be further simplified as

$$\chi(r, \theta) = G_2 K_2(\lambda r) \sin(2\theta). \tag{3.40}$$

Properly applying the characteristic functions can determine the stress concentration factor, $K = M_{\max} / M_x$, which becomes

$$K = \frac{M_{\theta} \left(a, \frac{\pi}{2} \right)}{M_x} = \frac{4 + 2\nu(1 - B) + (1 + B)N_1}{N_3}. \tag{3.41}$$

The concentration factors for a plate with Poisson's ratio, $\nu = 0.25$, under uniaxial bending, $B = 0$, are presented in Table 3.1. Results are compared to the exact three-dimensional elasticity solutions developed by Ablas [52] for an infinite isotropic plate with a hole.

Table 3.4 Stress concentration results for uniaxial bending of an infinite plate with $\nu=0.25$ compared to exact values of three-dimensional elasticity [51].

a/h	Ablas	Zeng
0	-	3.0
0.5	2.268	2.242
1	2.045	2.038
1.5	1.960	1.956
2	1.914	1.912
2.5	1.896	1.884
∞	1.769	1.769

It is noted that for small values of a/h , the stress concentration factor for an infinite isotropic plate with a circular hole subjected to an in-plane stress is achieved. Actually, Bert states that “in the limit of a very thick plate (large plate thickness/hole radius), K (stress concentration factor) for bending approaches that for in-plane loading” [45].

Bert and Zeng [45] also present numerical results for various cases considered in their model. Figure 3.17 shows the results of an infinite isotropic plate under uniaxial bending for various Poisson’s ratios and hole radius-to-thickness ratios. The FE model was updated with isotropic properties so that the results may be compared. As in the previous section, the in-plane FE model is modified to incorporate a uniaxial edge moment to induce a bending load. The isotropic properties of the plate are defined by an elastic modulus of $E = 69$ GPa. It is interesting to note in Figure 3.17 that as the damage diameter increase, relative to the thickness, the moment concentration reduces for each Poisson’s ratio. This is in contrast to the in-plane loading of an infinite isotropic plate where the stress concentration is constant and independent of Poisson’s ratio.

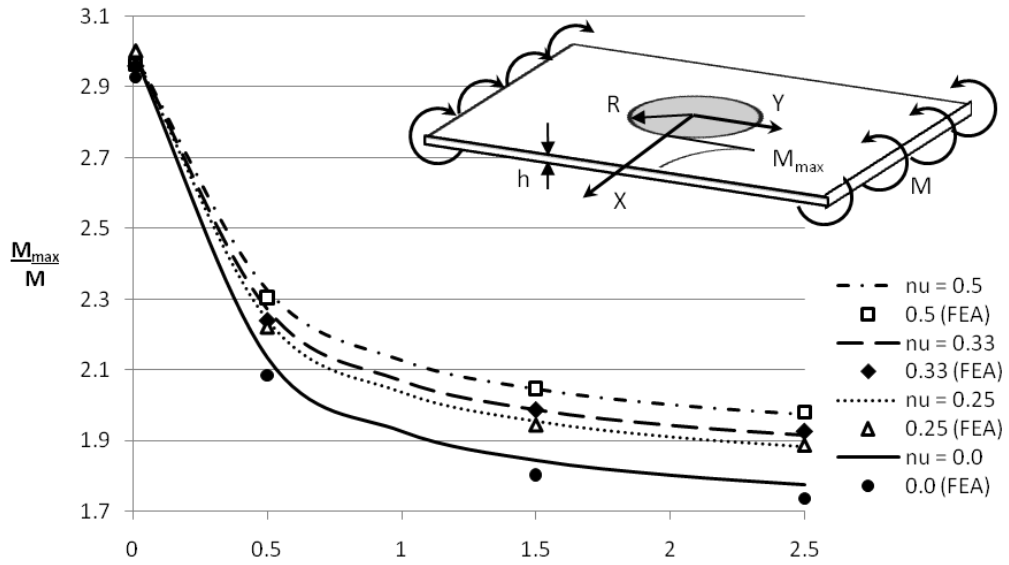


Figure 3.17 Moment concentrations for an infinite isotropic plate with various hole diameters and Poisson's ratios from out-of-plane bending [45].

Figure 3.17, however, accounts for a particular case of plate bending that is not wholly relevant to the present research. FAI testing considers a finite composite material containing a damage region that retains a fraction of the original undamaged properties. The size and stiffness of this inclusion will likely influence the moment concentration at its edge, which may be associated with the loss of flexural strength. Figure 3.17 instead suggests that the in-plane model developed in Section 3.2 may be converted into a bending simulation and possibly achieve reasonably accurate results. Thus, while Figure 3.17 is encouraging, it cannot solely justify the application of the FE model.

3.3.4 Bending of a Finite Orthotropic Plate with Hole

Complicated stress resultants arise from the introduction of an elliptical cutout to the bending of a plate, especially of finite width. Only a few researchers have addressed the problem of a finite plate analytically and have, in general, utilized complex potential theory. Typically, the pure bending and twisting deformations can be uncoupled, just like in-plane extension and shear. As a result, the in-plane and bending responses are completely uncoupled and the complex potential theory can be applied separately. Thus, only two complex potentials are required in the analysis to solve the responses independently.

Shuart and Prasad [53] solved the bending problem for a symmetrically laminated plate with finite length and width. The problem considered an elliptical cutout in a plate subjected to edge moments using their formulation for an infinite plate width. They combined a Laurent series approximation for the stresses and displacements with a boundary collocation method, minimized by a least-squares process.

Chen [54] formulated a solution for a plate with finite dimensions and a cutout and subjected to bending and twisting moments. He combined a Laurent series approximation with an energy method to eliminate the need for a boundary collocation method to determine the series constants.

Madenci *et al.* [55] developed a complex potential-variational method to model finite unsymmetric laminated plates with an elliptical cutout subjected to arbitrary edge loads. They used the complex potentials to reduce the potential energy of a plate to a contour integral. The equilibrium is expressed in variational terms and applied to the

potential energy. The solution of the resulting system of linear equations yields the stress and displacement fields for the given loading conditions.

These methods are computationally expensive and are not presented with accessible solutions, so their derivations are not recapitulated in this paper. To address the need for a finite width solution, the FE model developed in Section 3.2.4 will be extended to the case of uniaxial bending.

3.3.5 Bending of a Finite Orthotropic Plate with Orthotropic Inclusion

To model the effect of an elastic inclusion on the bending response of a composite plate with finite dimensions, the FE analysis software ABAQUS was used, just as in the in-plane scenario. The closed-form in-plane solutions were used to verify that the model produced accurate results. This mesh convergence study was assumed to provide comparable accuracy for the bending condition. Both the Leknitskii solution for an infinite plate and the Gillespie solution for the stress distribution in a finite plate were used to verify the results gathered from ABAQUS. The finite element solution seemed to correlate well for the experimental material given in Table 3.1.

Since no generally accepted and accessible closed-form expression exists for the bending of a laminate with an elastic inclusion, the model cannot be verified with analytical solutions. Therefore, the model developed under the in-plane loading case will be used also for the bending problem. Though stresses invoked by bending loads are more complex than in-plane, the accuracy at which the model approximates the analytical solutions provides confidence in its capacity to approximate the flexural response. The good correlation of numerical results to the modified FE models in Sections 3.3.2 and

3.3.3 also lends confidence to the applicability of the in-plane model validated in Section 3.2.

To simulate the bending conditions used in the experimental study, the model is updated to include the loading and support noses used for the four-point bending. The noses were modeled as discrete rigid circular cylinders with rectangular shell elements. The support noses were fixed in position and angle and the loading noses were constrained only to translate perpendicular to the plane of the plate. Again, quarter symmetry was used to reduce computation time. The loading noses were prescribed a load and the resulting deflection was used to calculate the modulus since the model is entirely elastic. Each layer of the experimental laminate contains the same plane-weave fabric; therefore the mechanical properties used for the in-plane model may also be applied to the bending case (Table 3.5) since there is no significant stacking sequence effect on the flexural response.

Table 3.5 Composite properties used for the out-of-plane bending model.

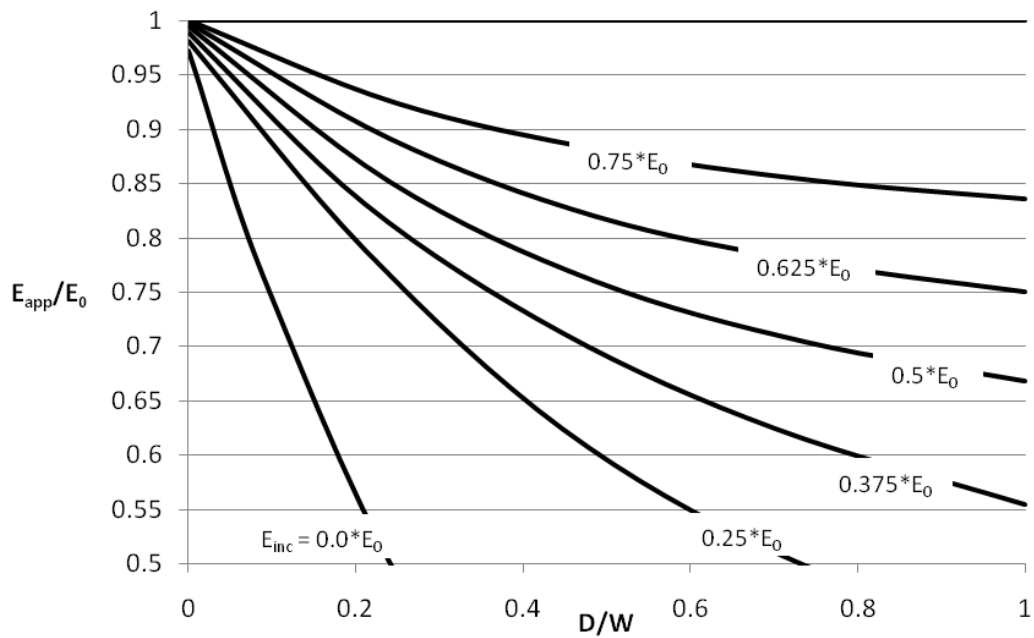
Ply Construction	Plane-weave
Layup	$[0^\circ/90^\circ/0^\circ/90^\circ]_s$
$E_0 = E_x, E_y$	29.50 GPa
E_z	9.80 GPa
$\nu_{xy}, \nu_{yz}, \nu_{xz}$	0.28
G_{xy}, G_{yz}, G_{xz}	3.40 GPa

Similar to the in-plane model, a design chart is developed to visualize the effects of damage width and inclusion stiffness on the response of the plate. For a plate of

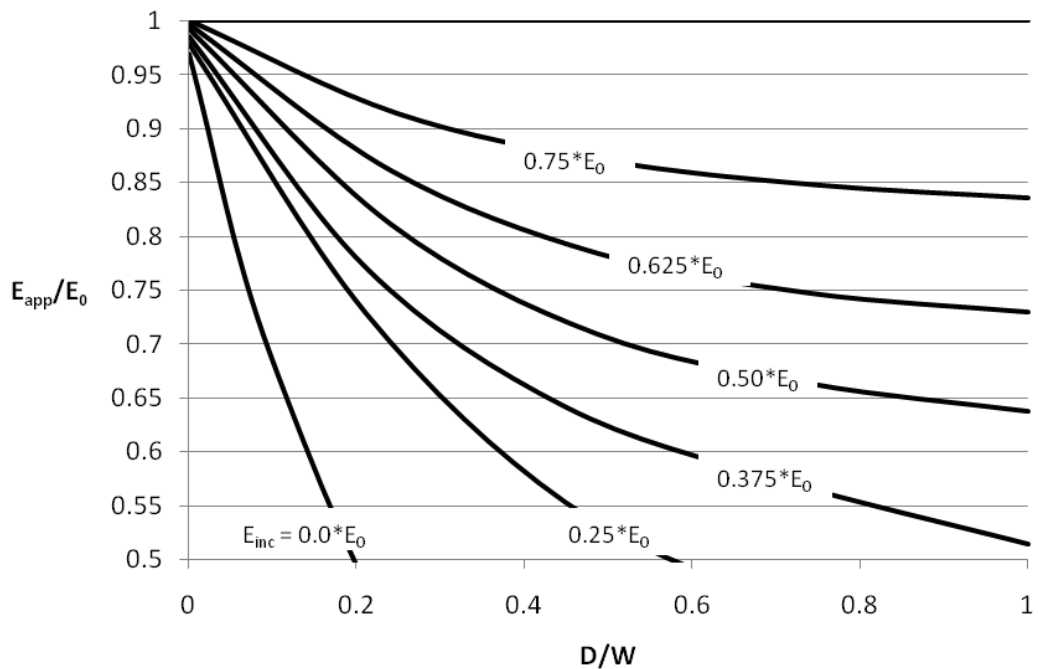
constant width (W), the inclusion diameter (D) is varied for a series of degraded inclusion stiffness values. The inclusion is assumed to have the same material architecture as the parent plate but with a fraction of the in-plane Young's modulus, E_0 . Figure 3.18 shows the effect of the inclusion on the residual apparent flexural modulus, E_{app} . As the inclusion diameter increases for a particular inclusion stiffness, the apparent flexural modulus is reduced. For the separated inclusions, the increasing diameter allows the inclusions to interact with each other. As the gap between the inclusions closes, there is a greater loss of overall stiffness. Comparing Figures 3.18a and 3.18b, the curves of the 2in separated inclusions fall lower on the $x = 1$ axis than the single inclusion curves.

The maximum moment concentrations for the 2in impacts (Figure 3.19b), however, also fall lower on this axis than for the single inclusions (Figure 3.19a). For very small inclusion diameters (infinite plate) with low stiffness, a trend emerges similar to Figure 3.17: the moment concentration diminishes as the diameter increases. Again, as the inclusions begin interacting with each other and the edge of the plate, the stress concentration rises. Higher inclusion stiffness, on the other hand, distributes the stress more evenly across the plate. When the stiffness is equivalent to the parent plate, the stress concentration is eliminated.

Experimental data will be overlaid onto these design charts to gauge the effect of damage width on the mechanical properties of an impacted composite plate.

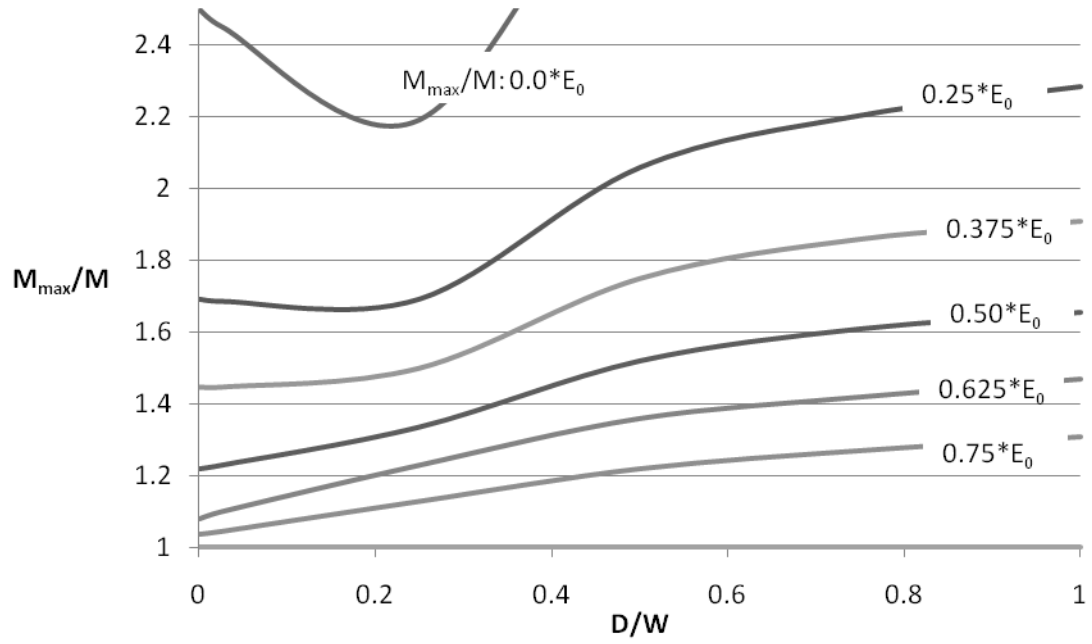


(a)

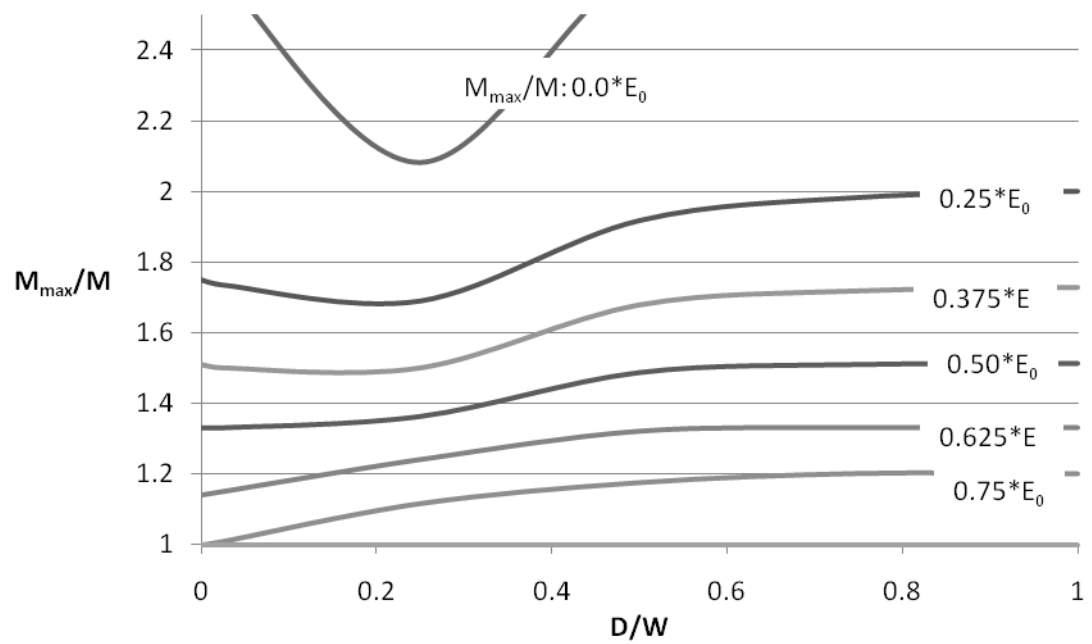


(b)

Figure 3.18 Effect of inclusion width and stiffness on the apparent flexural modulus of a finite plate containing (a) a centrally located inclusion and (b) two identical inclusions separated by $2i_n$.



(a)



(b)

Figure 3.19 Effect of inclusion width (D) and stiffness on the moment concentration at the edge of the inclusion within a finite plate of finite width (W) for (a) a centrally located inclusion and (b) two identical inclusions separated by $2i_n$.

3.4 Summary

In this chapter, the work of various researchers is presented in order to develop and validate both an in-plane and out-of-plane loading model. Using a complex variable method, Leknitskii [40] developed an exact closed-form analytical solution for the stress distribution of an infinite orthotropic plate containing an elastic inclusion. The inclusion is assumed to have the same composition as the parent plate, but with reduced mechanical properties. This solution was modified by Gillespie *et al.* [41] to account for finite-width effects of a hole employing a point-stress failure criterion suggested by Whitney and Nuismer [42]. These expressions were used to validate a finite element model composed in the ABAQUS analysis software. The ABAQUS results matched well with both the infinite and finite-width plate solutions for the experimental material. Since no exact expression exists for the effect of an elastic inclusion on the stress distribution of a finite plate, the model was used to plot the effect of inclusion size and stiffness on the in-plane response of the composite plate.

Unlike CAI, FAI is a relatively undeveloped topic. Only recent experimental and analytical work has been done to explore the effect of a hole/inclusion on the stress distribution of a plate in bending. While Leknitskii also provided a solution for the bending case, the evolution of his work is sparse with no accessible expression and no general consensus on an appropriate solution. Therefore, the work and numerical results of several researchers is presented to provide an accuracy basis for comparison. Good correlations to different results lend some confidence in the model to simulate the

bending response. Combined with its accuracy to the in-plane solutions, the model may be considered suitable for simple elastic analysis.

As in the in-plane case, a series of design charts were constructed to display the effect of inclusion width and stiffness on the stress concentration and stiffness of the plate. Both the apparent modulus and stress concentration show significant sensitivity to both inclusion diameter and stiffness, which is desirable for experimental testing.

Combining the model with experimental results will provide insight into the relationship between inclusion dimensions and stiffness, and the particular effect of damage on the flexural strength of an impacted plate.

Chapter 4

EXPERIMENTAL STUDY OF CAI AND FAI

4.1 Introduction

The goal of this research is to understand the impact and post-impact response of a composite material subjected to multiple non-coincident impacts. Samples are impacted under a drop-weight tower on a simple-support fixture to induce both local and global responses to the out-of-plane loading. A series of three impact energy values are selected to explore the relationship between absorbed energy and damage size and the effect of damage size on the residual mechanical properties. The internal damage is visualized with an ultrasonic C-scan procedure and the resulting images are measured with a commercially available image software. The residual compressive strength is calculated with a standard CAI method (see Chapter 2). A standard flexural method is modified to record the residual flexural strength and apparent flexural modulus (see Chapter 2). The ABAQUS FE software developed in Chapter 3 is used to model the post-impact flexural response of damaged samples in order to approximate the stiffness of the damaged inclusion based on its size.

Two of the energies tested for single impact will be used to generate multiple impact damage sites. These sites are separated by two distances to investigate the effect of proximity on the impact and post-impact characteristics of the material. A 2in

separation distance is used to produce two distinct but similar damage areas; a 0.5in separation allows the damage regions to overlap. Again the samples are scanned and measured to quantify the extent of the internal damage. The elastic flexural modulus is measured after each impact to monitor the accumulation of damage effects. The residual compressive and flexural strengths are evaluated after the second impact. FE methods are again used to model the flexural response. The implications of the results are discussed in Chapter 5.

4.2 Samples

Samples were composed of S-2 glass fibers in a 24oz/yd plane-weave fabric (Figure 4.1) infused with a CCMFCS2 epoxy resin matrix. The fabric was oriented in a cross-ply layup to avoid potential effects of the weaving process. S-2 glass and CCMFCS2 were chosen for the exceptional impact characteristics (Figure 2.4 and Table 2.2). Six parent panels were created using VARTM processing from which the individual samples were cut. All of the panels were prepared in a 72°F environment with 32% humidity. As discussed in Section 2.2.2, after the fabric layers were completely infused the injection line was clamped to create a resin-lean composite with a high FVF. After a 48 hour cure, the panels were post-cured at 200°F for eight hours according to the processing guidelines for the resin [37].

The dimensions of the samples were chosen with reference to the relevant experimental methods [18]. The target specimen thickness specified by CAI procedure is 0.20in, but with an acceptable range of 0.16in-0.24in [18]. Therefore, eight fabric plies were used to achieve a final average part thickness of $0.225\text{in} \pm 0.002\text{in}$. As designated

by the CAI method, a 4in width was used for each sample. The samples are initially cut to 8.5in to allow a 2in separation between impact events along a 6in impact support span. After the samples are impacted, however, they are trimmed to the required 6in so that the damage is centered in the plate.

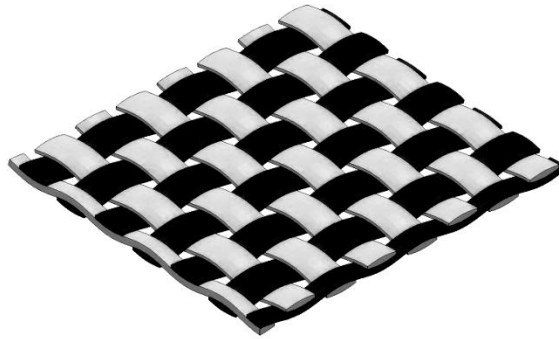


Figure 4.1 Plane-weave fiber construction used in the experimental material.

Panel quality was confirmed by measuring the void content, FVF, and thickness using standard test methods discussed in Section 2.2.3 ([33], [34], [35]). Samples for each method were taken from the center and edges of the panels. The void content was measured using both microscopy and standard techniques. Though microscopy is considered more reliable since the densities of the constituents were not independently measured, both reported a volume percentage less than one. Table 4.1 shows the results for each panel. Neither FVF nor thickness measurements showed any directional dependence, especially in regard to the infusion flow.

Table 4.1 Quality characteristics for the parent panels from which samples were cut.

Panel #	Thickness (in)	FVF	Void Content
1	0.225	55%	< 1%
2	0.226	57%	< 1%
3	0.223	58%	< 1%
4	0.226	55%	< 1%
5	0.224	58%	< 1%
6	0.227	57%	< 1%

4.3 Single Impact

4.3.1 Impact

The ASTM standard impact test [1] utilizes a constant impact energy normalized by specimen thickness. A series of three impact energies was selected to determine a trend between the impact characteristics and damage (Table 4.2). Ten samples were tested at each energy level. Peak load, contact duration, absorbed energy, and damage formation are the predominant characteristics of an impact event (Table 4.3). After each impact, NDE is used to evaluate the resulting damage. An ultrasonic C-scan method is used to determine the total area of the damage as well as its maximum length (diameter) along the unsupported width direction. The dimensions referenced in this section, as well as the following sections, correspond to the 99.9% threshold value. At this value the damage dimensions are typically larger and thus more conservative. The diameter will be used as the primary damage descriptor since it is more consistent across threshold values and within the ten replicates of each impact energy. The damage diameter, D , will typically be presented as a fraction on the plate width, W , in which it is contained.

Table 4.2 Impact parameters for the three energies used in single impact.

Impact Energy	Normalized Energy (in-lbf/in)	Mass (lbf)	Height (in)	Velocity (in/s)
Low	750	9.295	18 1/8	118.4
Middle	1000	9.295	24 3/16	136.7
High	1250	9.295	30 1/4	152.8

Table 4.3 Impact characteristics for ten samples at three incident energy levels

	Sample ID	Damage Area (mm ²)	Diameter (mm)	Peak Load (kN)	Duration (ms)	Absorbed Energy (N-m)
Low	L-1	76.69	11.92	11.17	9.44	4.79
	L-2	178.14	13.19	11.07	9.55	5.07
	L-3	275.97	11.62	11.15	9.47	5.08
	L-4	203.50	15.89	11.42	9.23	5.13
	L-5	42.87	6.60	10.85	9.84	5.33
	L-6	97.22	7.12	11.11	9.59	5.00
	L-7	121.98	12.97	11.28	9.49	5.14
	L-8	179.95	18.52	10.89	9.72	5.22
	L-9	59.18	9.22	11.15	9.61	5.06
	L-10	138.29	21.66	11.36	9.48	5.11
	Average	137.38	12.87	11.14	9.54	5.09
	Std Dev	72.75	4.79	0.18	0.17	0.14
Middle	M-1	160.02	16.94	9.88	10.57	6.93
	M-2	16.30	6.07	10.27	10.68	6.69
	M-3	199.88	17.99	10.15	10.64	6.63
	M-4	240.94	17.69	10.36	10.16	6.81
	M-5	71.86	9.82	10.09	11.20	6.70
	M-6	127.42	17.99	10.01	10.87	6.79
	M-7	433.57	32.23	9.77	10.66	7.23
	M-8	533.82	35.68	10.38	10.87	6.85
	M-9	417.27	26.46	10.02	10.80	7.07
	M-10	378.62	46.78	10.21	10.76	6.76
	Average	257.97	22.77	10.11	10.72	6.85
	Std Dev	173.27	12.46	0.20	0.27	0.18
High	H-1	1114.13	43.33	8.17	12.37	9.78
	H-2	1403.38	67.99	8.20	12.27	10.50
	H-3	1343.00	69.04	8.33	12.08	11.12
	H-4	1032.00	57.65	8.25	12.45	10.21
	H-5	1316.43	71.66	8.16	12.15	10.24
	H-6	834.54	47.30	8.23	12.14	9.71
	H-7	496.98	34.41	8.53	11.90	9.63
	H-8	1134.66	67.69	8.26	12.21	10.89
	H-9	823.67	46.78	8.62	12.03	9.95
	H-10	1105.68	73.01	8.27	11.88	10.26
	Average	1060.45	57.89	8.30	12.15	10.23
	Std Dev	278.65	13.90	0.16	0.19	0.50

Figure 4.2 compares the average peak load, contact duration, absorbed (dissipated) energy, and resulting damage size of the three impact energies; damage size will be discussed in the following section and representative images for each energy level will be presented. The magnitudes of these characteristics are normalized against the largest average of the three energy levels, i.e. the energy level that produced the largest peak load will have a value of one and the other values are scaled from its magnitude. It is easily seen that the highest incident energy produces the largest damage diameter and therefore the largest absorbed energy. This is also associated with the lowest peak load, which may not be expected. But, when the damage is created the overall stiffness of the material is reduced, as will be seen in Section 4.3.3. This compliance allows the contact force to occur over a greater period of time thereby reducing its maximum value. This is also supported by the fact that the opposite is true for the lowest energy.

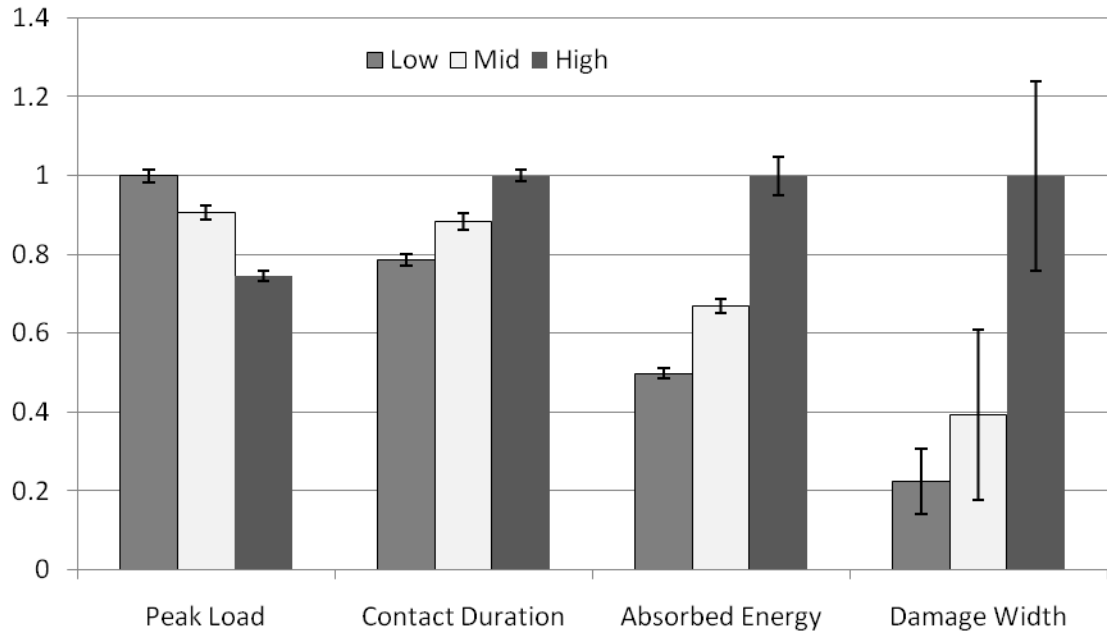


Figure 4.2 Normalized impact characteristics for three impact energies.

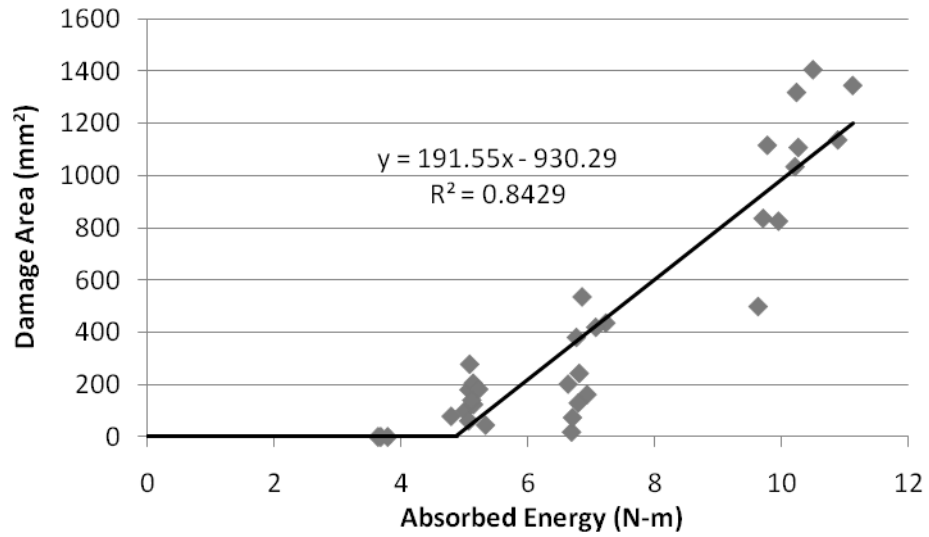


Figure 4.3 Linear relationship of damage area to absorbed energy. Energy absorbed increases with incident energy (Figure 4.2).

Figure 4.3 shows the relationship between absorbed energy and damage width. There appears to be a threshold energy value below which minimal damage is formed. This feature is confirmed by Zhang *et al.* [26] (as well as many others) and its value appears to be different for various materials. It also appears that the damage varies linearly with energy, which can also be observed in numerous studies ([26], [28], [29]). Though there is a significant amount of scatter in the raw data, the R^2 value suggests a reasonably good fit with the linear trendline.

4.3.2 Damage Evaluation

In order to assess the damage inflicted on the samples, a C-scan method as described in Section 2.4.2 was used. Each impacted sample was submerged in water and a 1MHz transducer scanned over the part in pulse-echo mode. Each sample was weighed before submersion and after drying to ensure that no water remained in the part for post-impact testing. The resulting gray-scale image depicts the scope of the damage. A Gaussian curve fit was performed on the image histograms to identify two suitable threshold gray values. An edge detection tool was used to highlight the damage region in the threshold images (Figure 4.4). Results for threshold values and the associated area and diameter are given in Table 4.4 for the three impact energies.

Table 4.4 Area and diameter measurements of threshold images for each impact energy.

	Sample ID	Slope Transition			99.9% Confidence Interval			% Difference	
		Threshold	Area mm ²	Diameter mm	Threshold	Area mm ²	Diameter mm	Area	Diam
Low	L-1	177	57.4	9.8	189	76.7	11.9	28.8	19.3
	L-2	179	115.9	11.1	190	178.1	13.2	42.3	17.3
	L-3	183	213.8	8.7	187	276.0	11.6	25.4	28.8
	L-4	180	166.7	13.0	189	203.5	15.9	19.9	20.3
	L-5	174	26.6	5.8	189	42.9	6.6	47.0	12.0
	L-6	177	83.3	4.7	177	97.2	7.1	15.4	40.5
	L-7	179	100.2	7.6	191	122.0	13.0	19.6	51.6
	L-8	181	143.7	15.4	195	180.0	18.5	22.4	18.1
	L-9	175	47.7	6.9	188	59.2	9.2	21.5	28.8
	L-10	180	105.7	16.1	182	138.3	21.7	26.7	29.4
		Avg	179	106.1	9.9	188	137.4	12.9	26.9
	Std Dev	3	57.2	3.9	5	72.7	4.8	10.2	12.0
Mid	M-1	178	141.3	15.1	181	160.0	16.9	12.4	11.7
	M-2	168	10.3	4.7	176	16.3	6.1	45.5	25.0
	M-3	173	160.6	14.1	179	199.9	18.0	21.8	24.3
	M-4	171	173.9	17.5	181	240.9	17.7	32.3	1.3
	M-5	170	68.2	9.0	189	71.9	9.8	5.2	8.8
	M-6	165	103.3	12.4	177	127.4	18.0	20.9	36.5
	M-7	177	366.5	31.0	181	433.6	32.2	16.8	4.0
	M-8	176	436.6	34.6	182	533.8	35.7	20.0	3.0
	M-9	168	348.4	24.9	181	417.3	26.5	18.0	6.0
	M-10	177	260.3	35.7	182	378.6	46.8	37.1	26.9
		Avg	172	206.9	19.9	181	258.0	22.8	23.0
	Std Dev	5	140.4	11.0	4	173.3	12.5	12.0	12.3
High	H-1	176	922.7	42.1	187	1114.1	43.3	18.8	3.0
	H-2	181	1217.4	64.8	193	1403.4	68.0	14.2	4.9
	H-3	189	1225.2	66.9	177	1343.0	69.0	9.2	3.2
	H-4	171	911.2	56.1	183	1032.0	57.6	12.4	2.8
	H-5	174	1163.0	70.3	193	1316.4	71.7	12.4	1.9
	H-6	169	763.3	47.1	179	834.5	47.3	8.9	0.5
	H-7	167	449.9	33.9	165	497.0	34.4	9.9	1.5
	H-8	171	1028.4	67.2	185	1134.7	67.7	9.8	0.8
	H-9	168	757.2	43.9	182	823.7	46.8	8.4	6.3
	H-10	191	963.2	72.7	185	1105.7	73.0	13.8	0.4
		Avg	176	940.2	56.5	183	1060.4	57.9	11.8
	Std Dev	9	240.9	13.8	8	278.6	13.9	3.2	1.9

The largest percent difference between the dimensions of the threshold images occurs for the lowest impact energy: 26.9% for the area and 26.6% for the diameter. This is primarily due to the relatively small magnitudes of both area and diameter. Relatively slight changes between them will represent a large percentage of their averages. The effect of this disparity on further analysis will be discussed in Section 4.3.4.

While it may be expected for the damage to occur symmetrically, subtle variations in local material structure, impactor centricity, and sample/support assembly can contribute to variability. It seems, however, that the delaminations tend to extend predominantly along the axis of the induced bending (x-axis), across the plate width (see Figure 2.7) (x-axis). This may be expected as the maximum stress during a three-point bending simulation with simple-supports will occur across the unsupported width (x-axis) below the loading site. Figure 4.4 shows the progression of damage size with the incident energy. While the middle and lower energies display a more circular, symmetric damaged region the larger energy tends to appear more elliptical. The major axes of the ellipses consistently stretch across the width of the plate, in the x-direction.

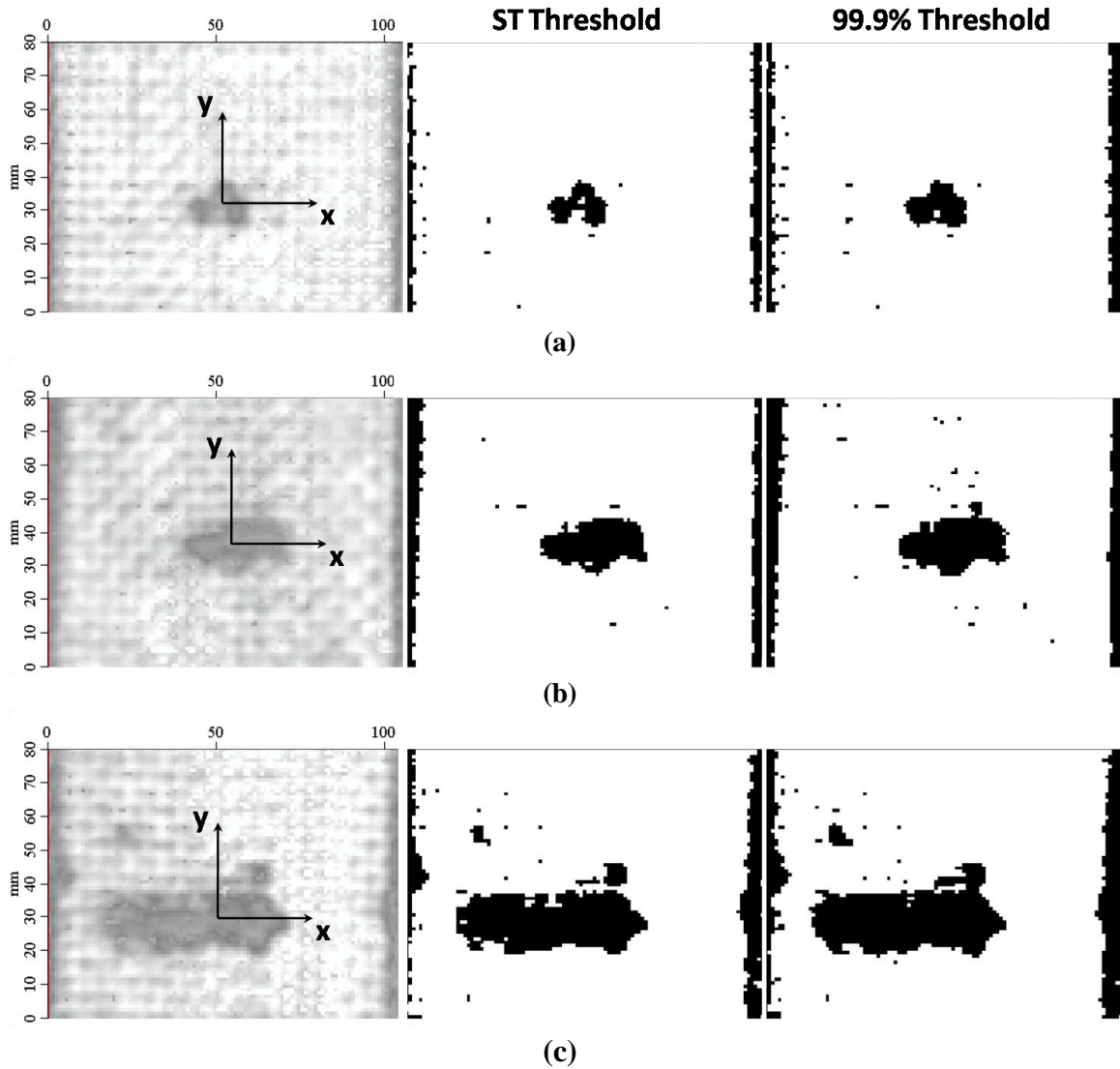


Figure 4.4 Typical C-scan images with the corresponding threshold areas for samples with (a) no, (b) low, (c) middle, and (d) high energy impacts.

Generally, damage caused by impacts in composite material contains the damage modes and overall shape depicted in Figure 4.5. To view this, destructive inspection was also used on representative samples to develop a view of the internal damage. The samples were sectioned along the two major axes to determine their relative extents. It

can be seen in Figure 4.6 that the obvious types of failure are delaminations and matrix cracking. The damage width appears to increase in width further from the impacted surface, creating a roughly conical shape. The largest delaminations occur farther from the impacted surface, as do the majority of the matrix cracks. The majority of the delaminations, however, occurred closer to the impacted surface where the material experiences compressive stresses, especially for the lower energies. For the low energy, the delamination appears to occur between the first two plies from the impacted face, 7-6 (Figure 4.5). The middle energy also contains delaminations between plies 6-5. The high energy appears to have delaminations between almost all of the ply interfaces, and appear to be similarly shaped. These delaminations are likely due to transverse and interlaminar shear stresses. During impact, a flexural wave through the material may induce peel forces between adjacent plies that produce cracks and may propagate into delaminations. As such, they can be found in the vicinity of matrix shear cracks.

While tensile matrix cracking occurs throughout the thickness, it is mostly concentrated above the lower surface. This is due to the fact that the impact event can be regarded as a bending load for which the lower surface carries the tensile stresses. Though these cracks appear to extend beyond the width of the delaminations, they are not captured by the ultrasonic scan. C-scans have been shown to be predominantly sensitive to the presence of delaminations, thus the dimensions of the damage are dependent on the size of the largest envelope of delaminated edges. The widths of the damage measured along the x- and y-axes from the sections were compared to the 99.9% threshold C-scan images. A maximum discrepancy of 6% for the high energy damage was recorded. Due

to the higher threshold value, the C-scan measurements were larger than those taken from the sectioned views. Since the damage will be later modeled as a through-thickness circle or ellipse, the results will likely be conservative. This seems suitable given the novel nature of this testing and assumptions used in the FE model.

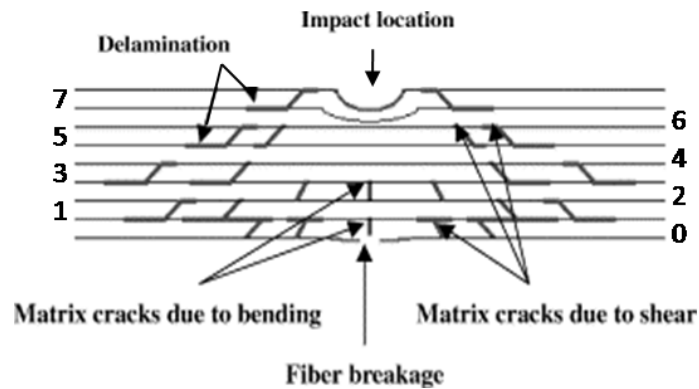


Figure 4.5 Damage by out-of-plane impact in composites typically contains delaminations and matrix cracking. The larger delaminations are typically further from the impacted surface creating an overall conical shape [56].

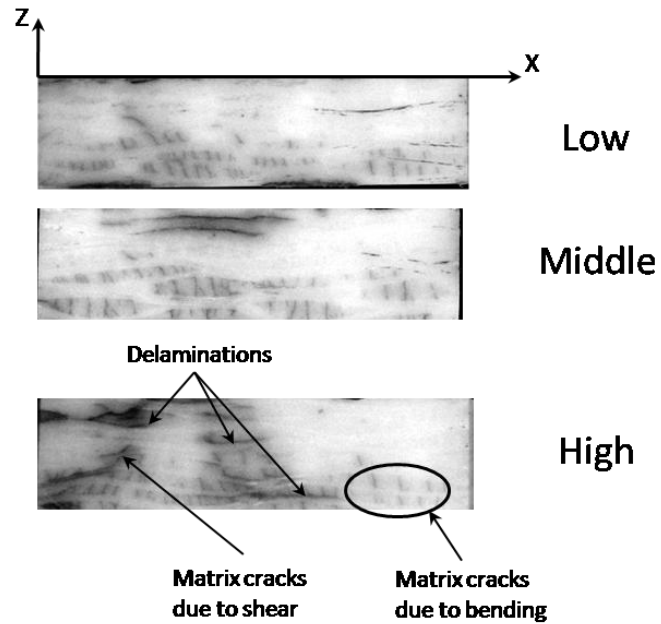


Figure 4.6 Representative samples were sectioned and polished to visualize the extent of the damage through the thickness and to gauge the accuracy of the C-scan images (3x magnification).

As discussed in Section 1.1.2 the residual compressive strength tends to be most sensitive to the presence of delaminations. Failure is typically induced by the unstable propagation of delaminations or stress concentrations in the undamaged ligaments adjacent to the impact damage. Therefore, the size and perhaps number of delaminations will likely affect the residual properties. Similarly, flexural failure can be achieved through delamination propagation and stress concentration on the compressed surface, as well as fiber rupture. Not only may the delaminations at the loaded surface cause a stress concentration, but matrix cracking on the lower face may impair the load carrying capability of the plate. For the following post-impact flexural experiments, the plate will be loaded on the impacted face.

4.3.3 Post-Impact

After the damage width and area were recorded for the impacted specimens, their residual properties are measured. Two methods: CAI and FAI are used to determine the influence of damage on the post-impact performance of the material. CAI has been extensively used to gauge the damage tolerance of comparable composite material systems. It was developed with a drop-weight impact method because it is particularly sensitive to the presence of delaminations introduced by such impacts. Limited research has been published on the influence of damage on flexural properties.

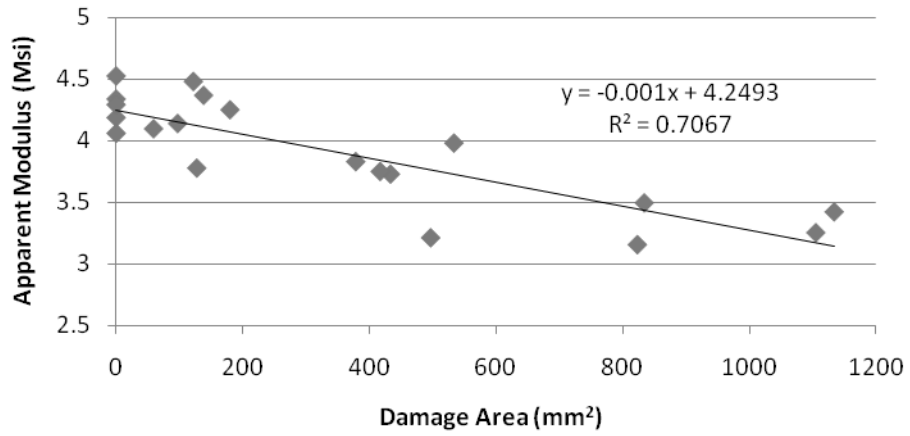
While CAI is the most widely accepted standard for damage tolerance, it requires extensive fixturing and does not simulate intended loading scenarios. A series of strain gauges are also necessary if compression modulus is relevant to the designer. Flexure, however, represents a load commonly associated with many applications. Only simple fixtures are needed and the recorded data provides strength and modulus information without additional gauging. Since CAI is an established standard it can be used as a comparative basis for the results of the FAI method. Results of both post-impact tests are tabulated in Tables 4.5 and 4.6. Their values are also plotted against the damage area in Figure 4.5.

Table 4.5 Residual compressive properties of five samples as each impact energy.

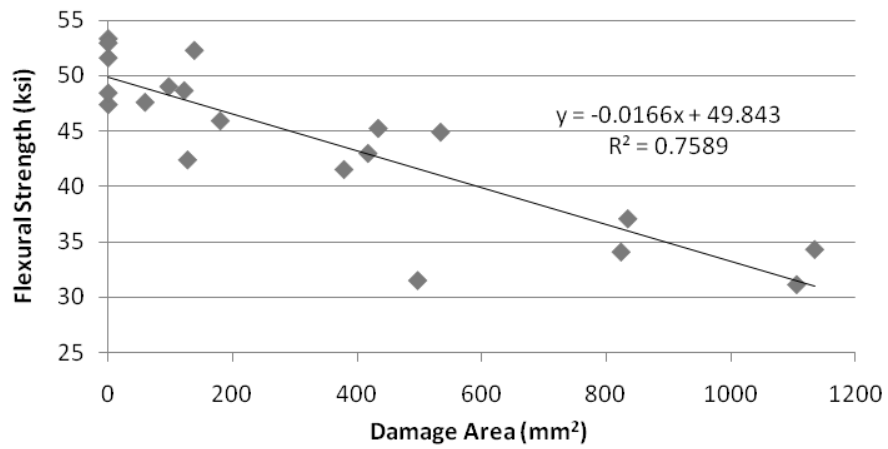
CAI			
Impact Energy	Sample ID	Max Load (lbf)	Strength (ksi)
Nominal	N-1	8287	36.80
	N-2	7943	35.66
	N-3	8095	36.21
	N-4	8210	36.49
	N-5	8036	35.84
	Avg Std Dev	8114 137	36.20 0.46
Low	L-1	28113	31.24
	L-2	28442	31.60
	L-3	28276	31.42
	L-4	27272	30.30
	L-5	28026	31.14
	Avg Std Dev	28026 450	31.14 0.50
Middle	M-1	20439	22.71
	M-2	24366	27.07
	M-3	23356	25.95
	M-4	24750	27.50
	M-5	24202	26.89
	Avg Std Dev	23422 1744	26.02 1.94
High	H-1	18678	20.75
	H-2	17566	19.52
	H-3	17619	19.58
	H-4	19378	21.53
	H-5	19126	21.25
	Avg Std Dev	18473 842	20.53 0.94

Table 4.6 Flexural results for five samples at each impact energy.

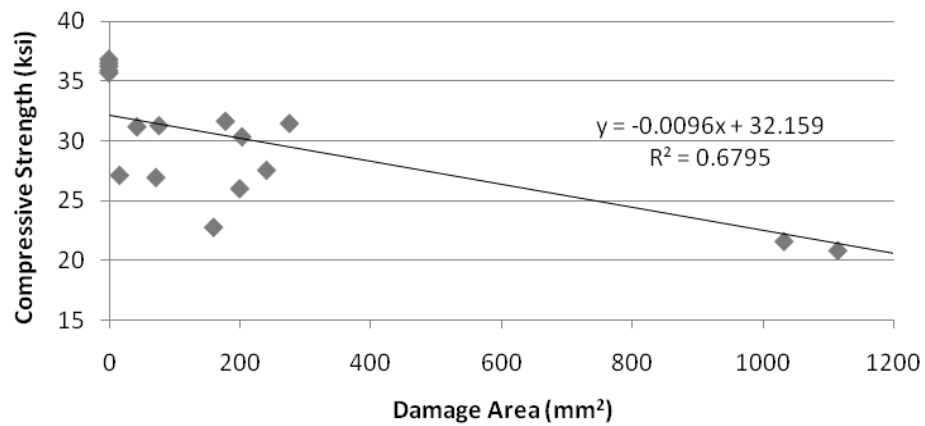
FAI					
Impact Energy	Sample ID	Max Load (lbf)	Deflection @ Max Load (in)	Apparent Modulus (Msi)	Strength (ksi)
Nominal	N-6	2258	0.422	4.52	51.63
	N-7	2068	0.461	4.18	47.40
	N-8	2336	0.408	4.34	53.36
	N-9	2319	0.411	4.29	52.97
	N-10	2115	0.451	4.06	48.45
	Avg	2219	0.431	4.28	50.76
	Std Dev	121	0.024	0.17	2.69
Low	L-6	2144	0.424	4.14	49.02
	L-7	2128	0.427	4.48	48.66
	L-8	2005	0.454	4.25	45.93
	L-9	2080	0.437	4.09	47.61
	L-10	2292	0.397	4.37	52.30
	Avg	2130	0.428	4.27	48.70
	Std Dev	105	0.021	0.16	2.34
Middle	M-6	1853	0.435	3.77	42.39
	M-7	1981	0.407	3.73	45.24
	M-8	1965	0.410	3.98	44.89
	M-9	1879	0.429	3.75	42.98
	M-10	1813	0.445	3.83	41.52
	Avg	1898	0.425	3.81	43.40
	Std Dev	72	0.016	0.10	1.61
High	H-6	1624	0.388	3.49	37.05
	H-7	1373	0.459	3.21	31.47
	H-8	1500	0.421	3.42	34.28
	H-9	1489	0.423	3.15	34.05
	H-10	1356	0.465	3.25	31.10
	Avg	1469	0.431	3.30	33.59
	Std Dev	109	0.031	0.14	2.42



(a)



(b)



(c)

Figure 4.7 The residual (a) modulus, (b) flexural strength, and (c) compressive strength tend to decrease with increasing damage area.

CAI is traditionally known to be sensitive to the size of impact-induced damage, i.e. delaminations. Despite significant scatter for the smaller damage sizes, the residual compressive strength in Figure 4.7c shows a marginally strong relationship with the damage area. The R^2 value of the linear regression line (0.68) indicates the strength of the relationship between the residual property and damage area; the slope ($m = -0.010$) indicates its sensitivity to increasing damage sizes. As such, the residual flexural strength (Figure 4.7b) displays a good relationship ($R^2 = 0.76$) with the damage area and a similar sensitivity as the CAI results ($m = -0.017$). For example, the CAI and FAI strength decrease by 40% at the largest damage area.

The modulus regression line in Figure 4.7a cannot be compared directly with the strength results. The 25% stiffness loss to the largest damage, on the other hand, can be compared to the 40% loss of strength. This suggests that the modulus is relatively much less sensitive to damage size. The marginal strength of the data ($R^2 = 0.71$), however, suggests that a distinguishable relationship exists between the stiffness and damage area. Given the scatter of the original impact and damage data, these results are encouraging. Considering both the flexural strength and modulus data, it may be feasible to employ FAI as a post-impact damage tolerance test.

Figure 4.8 presents a side-by-side comparison of the residual mechanical properties. Nominal (unimpacted) values were measured in flexure and compression and used to normalize the damaged values. Just as in the impact characteristics plot (Figure 4.2), the average and standard deviation for each property is normalized by the largest average of the nominal values; thus, the average for each nominal property is one. Figure

4.8 shows a clear degradation in strength for both methods as the incident impact energy increases. This is attributed to the fact that the larger energies produced larger damaged areas. While CAI showed distinct sensitivity to the delaminations introduced by the lowest energy, the reduction of flexural properties is much less but still significant. At the middle and high energies both the flexural and compressive properties are distinctly reduced. Compressive failure of the damaged samples predominantly occurred across the undamaged ligaments adjacent to the damaged inclusion, as opposed to the unstable propagation of the inclusion delaminations. This is consistent with the analytical model referenced in Chapter 3. Whitney and Nuisimer [42] established a PSC that predicts the nominal maximum compressive strength to occur at a distance from the edge of a hole due to its inherent stress concentration. This provides further confidence in the FE model which depicts such a concentration but has no regard to the instability of the inclusion.

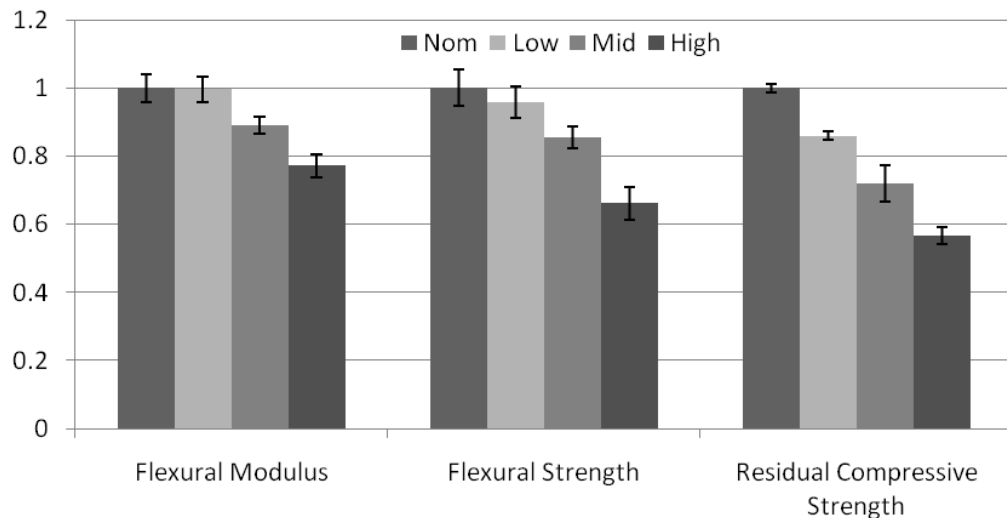


Figure 4.8 Normalized residual mechanical properties after a central, three-point impact of varying energy.

As is confirmed by Zhang and Richardson [26], the residual flexural strength appears slightly more sensitive to the damage than modulus. Failure was initiated on the loaded/compression side of the samples. Stress concentrations introduced by the damaged regions may be attributed the gradual strength loss with increasing damage size. Coupled with greater back-surface matrix cracking at the higher impact energies, this may contribute to the loss of flexural stiffness. Significant displacement prior to failure during the tests may be attributed to the relatively high-strength, low-modulus S-2 glass fabric reinforcement. Typically failed samples are shown in Figure 4.9. Since the samples damaged by the different impact energies failed in a similar manner, only one example CAI and FAI sample is given. The residual flexural and compressive properties will be modeled in the following section.

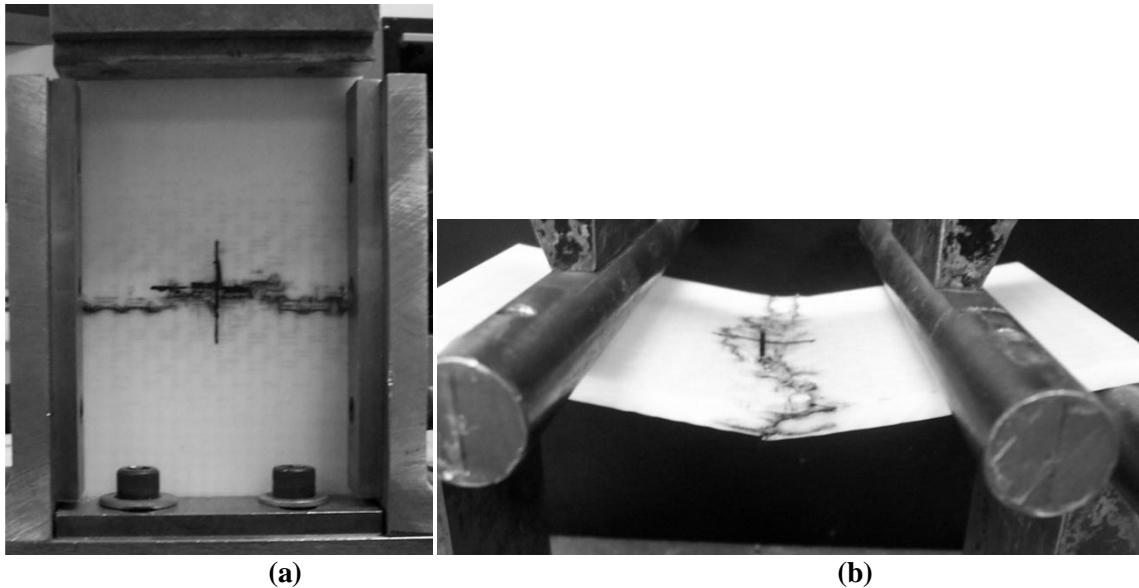


Figure 4.9 Samples damaged by the three impact energies failed similarly in (a) compression and (b) flexure.

4.3.4 FEA of Post-Impact Performance

Explored by Monib *et al.* [24], the damage size in an impacted material can be assigned reduced properties that would result in overall residual properties similar to those measured experimentally. They investigated this method with good results for CAI and so it will be extended in this research to FAI. While there are several papers concerned with the exact analytical solution of an anisotropic material with an inclusion under bending [43], they are mathematically intensive and their utility to a designer or technician would be minimal. Thus, a finite element program, ABAQUS, will be used to approximate the effects of an inhomogeneous inclusion on the global properties of a composite material.

The model used in this method is defined in Sections 3.2.4 and 3.3.5, where its validity is also established. The damaged areas will be idealized as circles or ellipses depending on the measurements taken from the C-scan images; the low and middle impact energies tended to produce more circular damaged zones. If there is a strong correlation between the area and maximum diameter, then the damage is modeled as a circle:

$$0.85 * D \leq \sqrt{\frac{4 * A}{\pi}} \leq 1.15 * D \quad (4.1)$$

where D and A are the maximum damage diameter and area, respectively, measured from the C-scan images. Or, in other words, if a circle containing the maximum measured diameter has an area greater than the measured area, then the damage is modeled as an ellipse. For instance, sample L-2 from Table 4.4 has a measured diameter of 13.19mm

and area of 178.14mm. This area corresponds to a circle with diameter 15.06mm, which is 1.14 times the measured diameter. So, the damage in sample L-2 is modeled as a circular inclusion of diameter 15.06mm. Sample M-10, however, has a measured diameter of 46.78mm and circular diameter of 21.96mm, which is $0.47*D$. Therefore, the damage is modeled as an elliptical inclusion with a 46.78mm major diameter.

The minor diameter is defined so as to produce an area equivalent to that of the measured image. The highest impact energy most consistently produced and elliptical-type damage formation.

The elliptical dimensions are applied to the finite element inclusion within the parent plate of undamaged material. The in-plane elastic modulus of the inclusion (E_{inc}) was reduced until the global bending moduli measured during the experiments are attained. The definition of bending modulus is given by Equation 4.2 and is applied identically to both experiments and numerical results of the FAI test. Figure 4.9 shows the normalized inclusion stiffness as a function of damage diameter. It is easily seen that as the damage size increases it is associated with a larger reduction in inclusion stiffness. Comparing this trend to Figures 4.6, more damage in the form of cracks and delaminations corresponds to increasing impact energy. However, a bilinear trend can be applied to Figure 4.9 by intersecting the regression line of the middle and low energies with the horizontal trend line of the high energy. This suggests that as damage size increases, the geometrical effect of the inclusion overcompensates for the loss of inclusion stiffness. In other words, after a certain size the reduction of the apparent modulus can be achieved by larger damage dimensions with the same inclusion stiffness.

This can also be seen in Figure 3.14. Along the lines of constant inclusion stiffness, the apparent modulus decreases with increasing damage diameter.

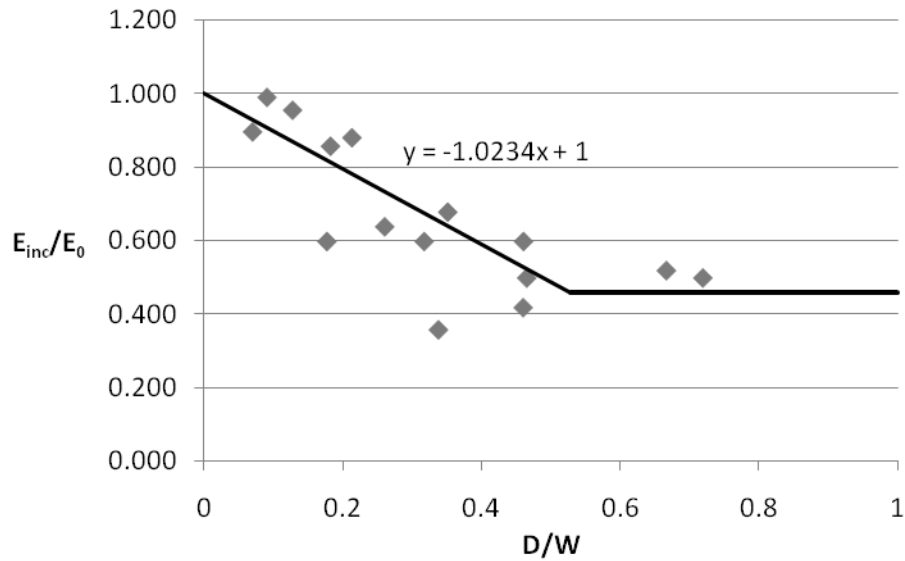


Figure 4.10 As damage width increases the inclusion stiffness begins to plateau, creating a bilinear-type trend ($W = 4$ inches)

The experimental data from the previous section can be overlaid onto Figures 3.8, 3.14, and 3.15. Since the experimental modulus values were used to determine the inclusion stiffness based on damage size, the inclusion stiffness values read from the design chart (Figure 4.11) match those given in Figure 4.10; each experimental data point is labeled with the inclusion stiffness measured from the FE model. Figure 4.11 also shows the effect of impact energy on the inclusion stiffness and apparent modulus. While the damage sizes (D/W) may overlap, the higher impact energies correspond to a larger degradation of inclusion stiffness. The lower inclusion stiffness (for the same damage

size) in turn reduces the global apparent modulus of the plate. The combination of inclusion size and stiffness also influences the concentration of stress at its edges, which may be a good indicator to the strength loss of the corresponding sample. Thus, elastically measuring the residual flexural modulus and damage size not only provides insight into the particular inclusion properties but also the residual strength characteristics.

To investigate this further, Figure 4.12 compares the experimental strength results with the FE stress concentrations. As discussed for Figure 3.14, the constant inclusion stiffness lines are calculated from the moment concentrations in the FE model (M_{\max}/M). The experimental values are calculated as the fraction of nominal flexural strength to the residual (S_0/S_{FAI}). The surface stress that causes failure in bending is essentially Mc/I , where c is the distance from the neutral axis to the surface and I is the moment of inertia. Since c/I is constant in this study, the ratio of moments is equivalent to the ratio of the failure stress. Therefore, the FE results may be expected to be equivalent to the experimental. Though the data points do not fall exactly on the corresponding inclusion curves, there appears to be good agreement between the experimental and FE results. This correlation is displayed more clearly in Figure 4.13.

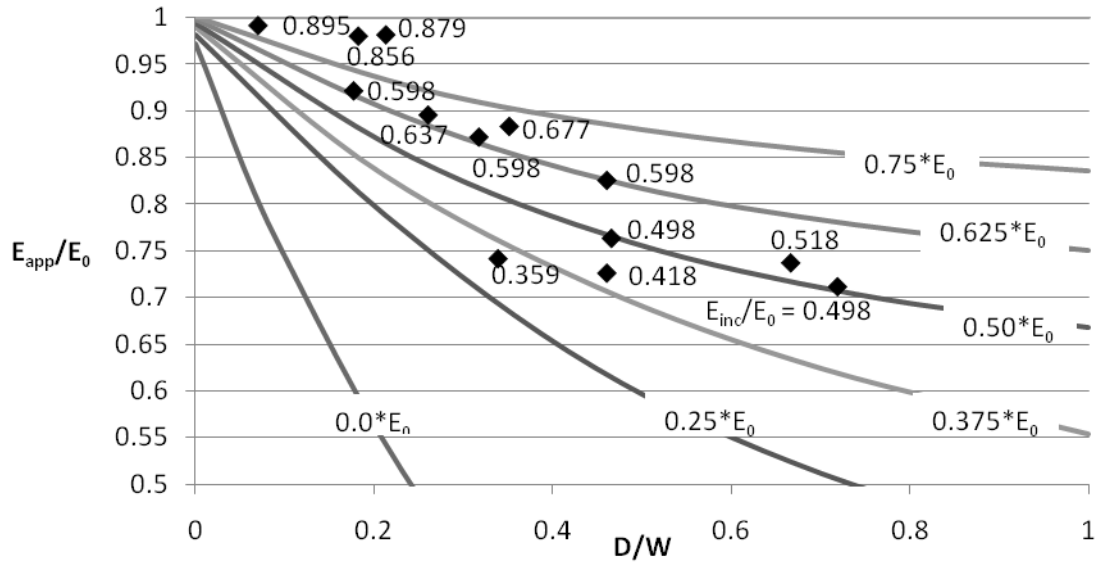


Figure 4.11 The particular inclusion stiffness suggests that estimating the damage that a hole may be unnecessarily conservative.

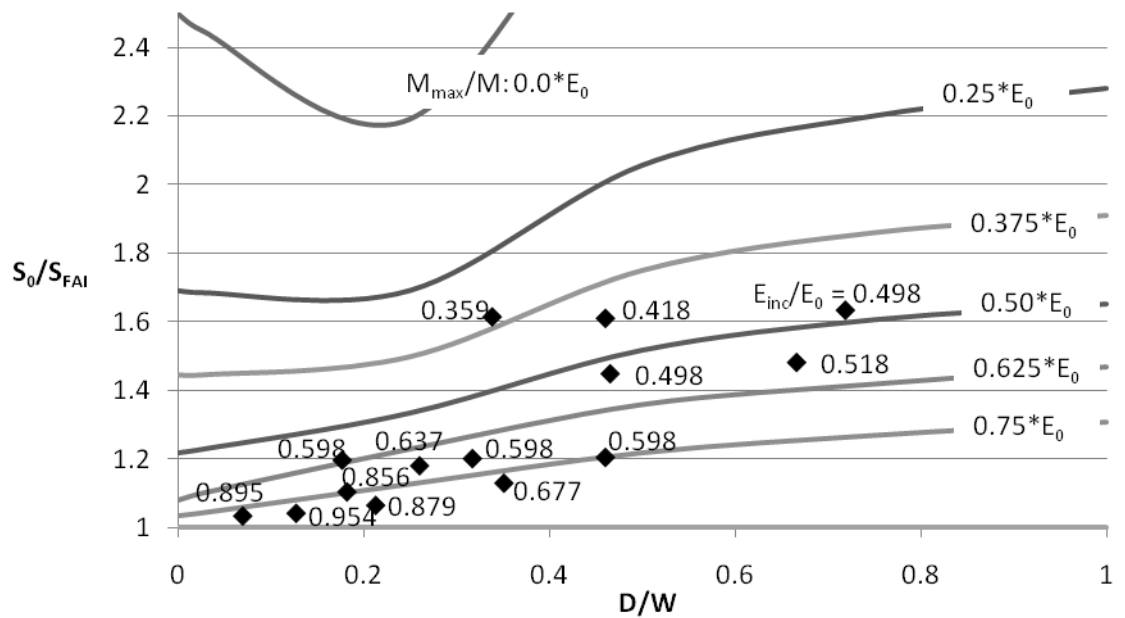


Figure 4.12 While the inclusion values do not exactly match, the moment concentrations predicted by the model may be similar to the experimental strength ratios.

Figure 4.13 plots the FE stress concentrations ($K_M = M_{\max}/M$) against the experimental strength ratios, S_0/S_{FAI} ; where S_0 is the undamaged flexural strength and S_{FAI} is the residual strength. If the FE stress concentration exactly predicted the residual strength, the slope of the regression line would be one and pass through the point (1, 1). The actual slope in Figure 4.13, however, is 1.04 and the data strongly fits this trend ($R^2 = 0.95$); the average percent difference of the FE results from the experimental data is $-1.5 \pm 4.0\%$. This suggests that the FE model consistently, if only slightly, overestimates the residual strength. Therefore, it is possible to reasonably approximate the residual flexural strength by simply measuring the damage dimensions and apparent modulus.

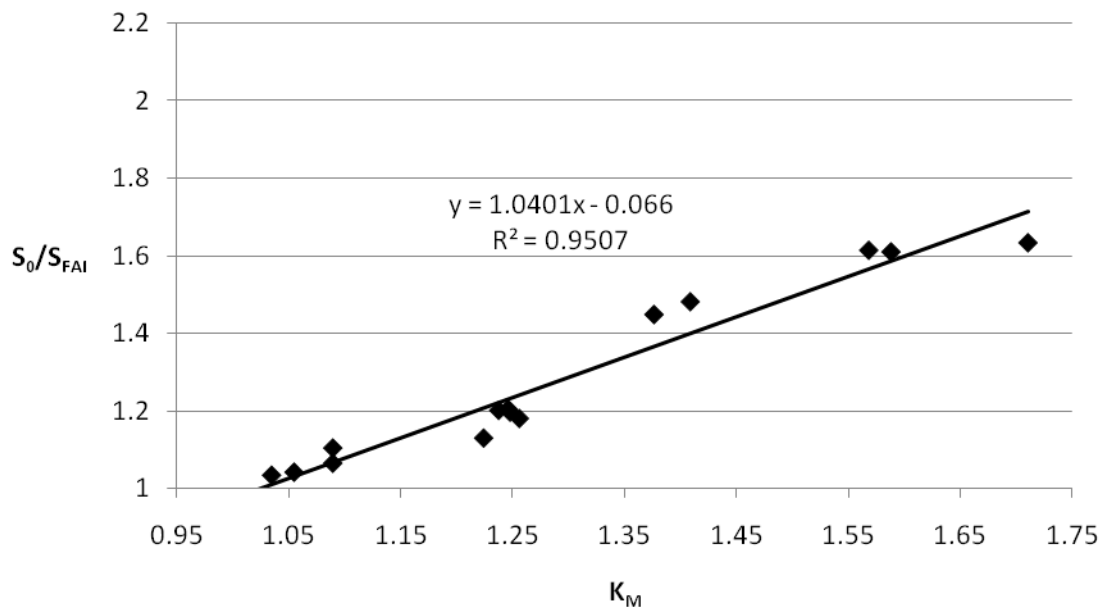


Figure 4.13 Plotting the experimental and FE stress concentrations against their shared damage diameters shows a good correlation of the FE model.

It may also be possible to predict the residual compressive strength using the FE model. Recall that stiffness loss in the CAI samples is not tested as part of the standard; thus, the inclusion stiffness is not calculated. Stiffness values can be extrapolated, however, from the modulus data for the known damage sizes in the CAI samples. The regression lines constructed in Figure 4.10 are used to calculate the stiffness of the CAI inclusions according to their diameters. Just as in Figures 4.11 and 4.12, the experimental data is labeled with the corresponding stiffness and overlaid onto Figure 3.8 (Figure 4.14). The inclusion values are less accurate than for the flexural data, especially at the lower inclusion sizes far away from the assumed plateau region. As the inclusion size increases, however, most of the points fall in the vicinity of their respective inclusion curves. This may be attributed to the noticeable scatter in the stiffness plateau (Figure 4.10) combined with the scatter of the original damage and CAI data. Had the modulus been measured for the CAI samples, the accuracy may have improved.

The FE and experimental correlation is more clearly displayed in Figure 4.15. The stress concentrations ($K_T = \sigma_{\max}/\sigma$) are plotted with the experimental strength ratios, $\sigma_0/\sigma_{\text{CAI}}$; where σ_0 is the undamaged strength and σ_{CAI} is the residual compressive strength measured by CAI. The data strongly correlates ($R^2 = 0.87$) to a regression line with slope $m = 0.71$; the percent difference of the FE results from the experimental data is $6.3 \pm 9.4\%$. Had the model exactly predicted the experimental strength reductions, the slope of this line would be 1. Thus, the FE model appears to consistently underestimate the residual strength, which may be suitable where conservative approximations are best.

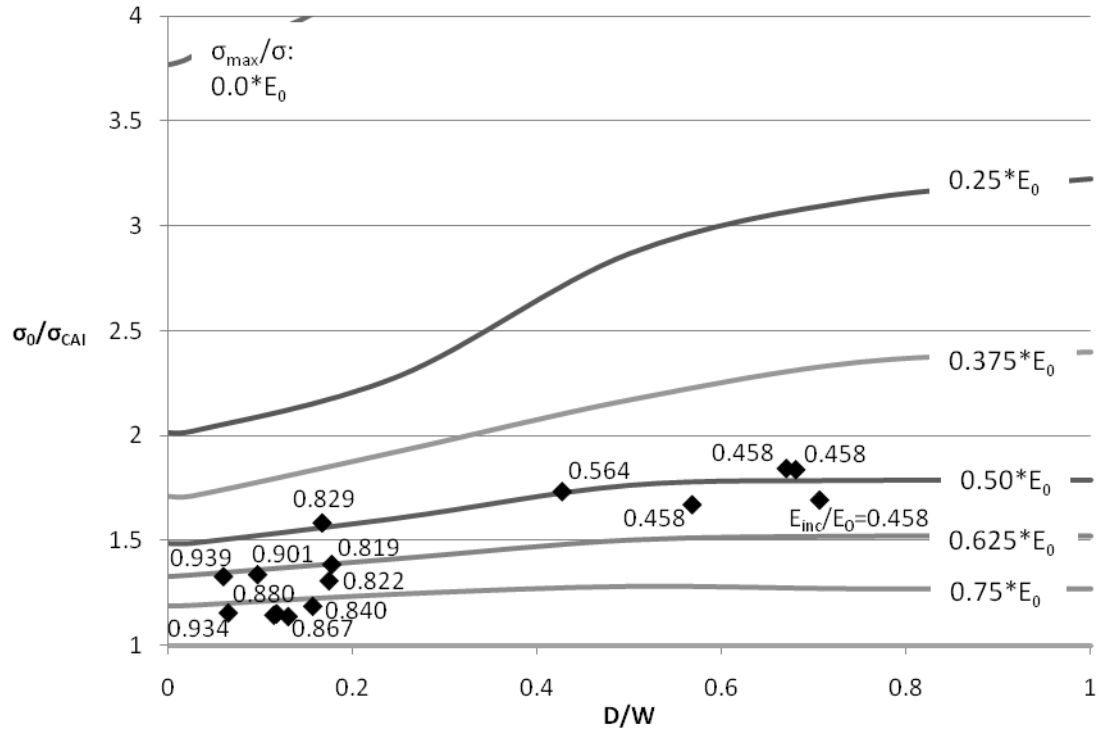


Figure 4.14 Though the exact inclusion stiffness is not known for the CAI samples, the stiffness values read from the chart are comparable to those from the flexural models.

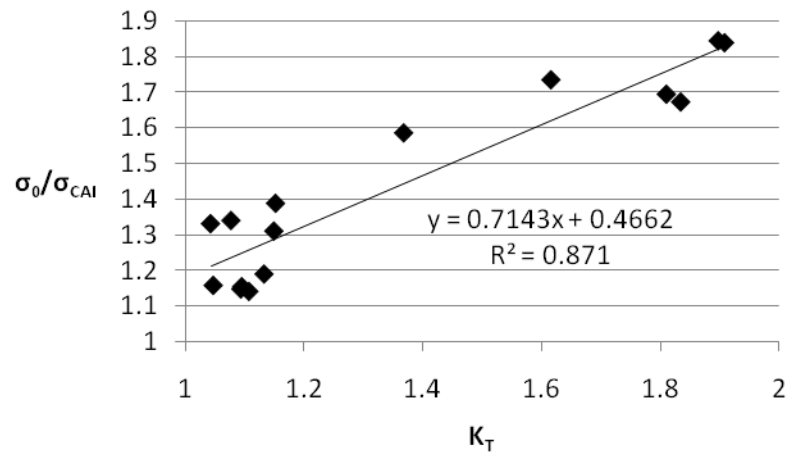


Figure 4.15 Similar trends emerge when comparing the in-plane concentrations of the flexural models and the experimental strength ratios.

4.4 Multiple Impacts

Much of the research involving multiple impacts concerns repeat events at a single location. However, during application it is unlikely that a structural backing panel will be impacted multiple times at the same location. More likely to occur is an impact at a location in the vicinity of a previous event. The questions that arise are discussed in Section 1.2. When a material is impacted, an area of reduced properties is created. This localized area also influences the global properties of the structure, so its response to multiple impact events may also be affected. The goals of this experimental series are to determine the effects of the number of impacts on a material stiffness and strength as a function of proximity. Each of the impacts will occur at center-span to ensure the consistency of the loading scenario and structural response. The samples were cut to 8.5in so that the impacts may occur at center-span while separated by a finite distance. Two separation distances were chosen to explore the effect of vicinity on the impact and post-impact response of the material, 2in and 0.5in. Using the results of the single impact as a reference, the middle and high energies were chosen to produce distinct damage sizes and shapes. Since the maximum width of the damage along the span direction fell between 1in-1.25in, a separation distance of 2in was selected to produce distinct impact sites and damage areas. A separation distance of 0.5in was also selected to establish the effect of overlapping damage areas.

4.4.1 Impact

As mentioned in the previous section, both separated impacts occur at center span. After the initial impact, the sample is repositioned such that the second impact

occurs 2in or 0.5in from the location of the first and centered between the support noses. After the first impact, the sample is C-scanned to measure the resulting damage area and is tested to determine the residual modulus. These results will be displayed in the following sections. Results for the multiple impact tests are given in Tables 4.8-4.10.

Table 4.7 Impact characteristics of the first middle-energy impact at two separation distances.

First Impact, Middle Energy							
Impact Energy	Separation	Sample ID	Area (mm ²)	Diameter (mm)	Peak Load (kN)	Duration (ms)	Absorbed Energy (N-m)
Middle	2in	M(2in)-1	561.59	35.46	10.30	10.70	7.23
		M(2in)-2	671.50	46.03	10.07	10.85	7.46
		M(2in)-3	375.00	36.73	9.79	10.84	7.13
		M(2in)-4	447.46	26.69	9.63	10.85	8.16
		M(2in)-5	374.40	30.96	9.63	10.70	7.38
		M(2in)-6	310.39	27.74	9.51	10.76	8.85
		M(2in)-7	269.32	20.61	9.70	10.83	7.95
		M(2in)-8	351.45	37.78	10.05	10.63	7.55
		M(2in)-9	536.84	45.73	10.08	10.24	7.42
		M(2in)-10	200.48	24.59	9.95	10.42	7.46
		Avg	409.84	33.23	9.87	10.68	7.66
	Std Dev	144.68	8.63	0.26	0.20	0.52	
	0.5in	M(.5in)-1	298.91	24.06	9.46	12.34	6.86
		M(.5in)-2	147.34	12.14	10.46	12.55	6.86
		M(.5in)-3	208.33	17.69	10.50	12.70	7.02
		M(.5in)-4	200.48	18.22	11.09	12.57	7.74
		M(.5in)-5	396.74	31.71	10.55	12.13	7.13
		M(.5in)-6	22.34	6.37	10.51	12.19	6.90
		M(.5in)-7	123.19	15.89	9.84	12.22	7.09
		M(.5in)-8	417.27	34.63	10.72	12.39	6.92
		M(.5in)-9	390.70	37.78	9.96	12.08	6.93
		M(.5in)-10	243.96	28.04	10.47	12.10	6.86
Avg		244.93	22.65	10.36	12.33	7.03	
Std Dev	130.86	10.28	0.47	0.22	0.27		

Table 4.8 Impact characteristics of the first high-energy impact at two separation distances.

First Impact, High Energy								
Impact Energy	Separation	Sample ID	Area (mm ²)	Diameter (mm)	Peak Load (kN)	Duration (ms)	Absorbed Energy (N-m)	
High	2in	H(2in)-1	641.33	41.56	7.76	10.91	9.66	
		H(2in)-2	346.02	23.11	7.70	11.04	10.05	
		H(2in)-3	205.92	18.52	7.89	11.00	9.77	
		H(2in)-4	563.41	32.76	7.82	10.77	10.22	
		H(2in)-5	500.00	35.98	7.70	11.01	11.82	
		H(2in)-6	948.67	65.07	7.75	10.70	9.89	
		H(2in)-7	679.35	40.48	7.78	10.55	10.90	
		H(2in)-8	1724.03	83.81	8.20	10.30	9.99	
		H(2in)-9	1197.46	71.89	8.20	10.27	11.36	
		H(2in)-10	1046.50	60.04	8.60	12.47	11.22	
		Avg	785.27	47.32	7.94	10.90	10.49	
		Std Dev	451.82	21.73	0.30	0.62	0.77	
		0.5in	H(.5in)-1	1124.40	57.65	8.49	12.61	9.78
			H(.5in)-2	1282.61	63.72	8.48	11.30	9.28
			H(.5in)-3	787.44	43.33	8.80	11.35	9.19
			H(.5in)-4	866.55	51.80	8.58	11.04	10.29
			H(.5in)-5	1491.55	86.43	8.60	12.12	9.69
			H(.5in)-6	1586.96	83.81	8.34	11.97	11.27
			H(.5in)-7	942.63	57.87	8.35	12.04	11.02
			H(.5in)-8	1286.84	71.66	8.36	12.61	10.25
			H(.5in)-9	1402.17	78.04	8.52	12.01	10.39
			H(.5in)-10	1655.80	84.26	8.44	12.45	10.26
	Avg	1242.69	67.86	8.50	11.95	10.14		
	Std Dev	304.20	15.16	0.14	0.55	0.68		

Table 4.9 Impact characteristics of the second middle-energy impact at two separation distances.

Second Impact, Middle Energy							
Impact Energy	Separation	Sample ID	Area (mm ²)	Diameter (mm)	Peak Load (kN)	Duration (ms)	Absorbed Energy (N-m)
Middle	2in	M(2in)-1	389.49	29.46	10.34	10.72	7.15
		M(2in)-2	484.90	30.96	9.73	10.81	7.55
		M(2in)-3	314.01	22.49	9.74	10.88	7.44
		M(2in)-4	986.71	66.64	9.86	10.82	7.43
		M(2in)-5	336.96	24.89	9.86	10.65	7.37
		M(2in)-6	211.96	18.74	9.70	10.80	7.18
		M(2in)-7	353.86	33.06	9.83	10.68	7.64
		M(2in)-8	341.18	43.63	9.82	10.53	8.70
		M(2in)-9	291.06	26.69	10.20	10.21	7.18
		M(2in)-10	314.61	25.64	10.19	10.28	7.18
	Avg	402.48	32.22	9.92	10.64	7.48	
	Std Dev	216.79	13.86	0.23	0.23	0.46	
	0.5in	M(.5in)-1	564.61	32.01	9.67	13.07	7.36
		M(.5in)-2	271.14	15.89	9.80	13.33	7.16
		M(.5in)-3	431.76	19.57	9.91	13.25	7.10
		M(.5in)-4	657.00	29.09	9.91	13.24	7.30
		M(.5in)-5	626.81	31.71	10.02	13.04	8.22
		M(.5in)-6	111.71	10.34	10.27	13.41	7.59
		M(.5in)-7	774.76	34.93	9.27	13.38	7.40
		M(.5in)-8	781.40	35.68	9.30	12.19	7.75
		M(.5in)-9	602.66	29.91	9.55	12.00	7.57
		M(.5in)-10	528.99	25.41	9.59	13.01	7.64
Avg		535.08	26.45	9.73	12.99	7.51	
Std Dev		212.51	8.52	0.32	0.49	0.33	

Table 4.10 Impact characteristics of the second high-energy impact at two separation distances.

Second Impact, High Energy							
Impact Energy	Separation	Sample ID	Area (mm ²)	Diameter (mm)	Peak Load (kN)	Duration (ms)	Absorbed Energy (N-m)
High	2in	H(2in)-1	352.47	29.40	7.83	10.88	9.76
		H(2in)-2	764.81	59.81	7.64	10.94	9.19
		H(2in)-3	446.86	33.58	7.67	10.81	9.22
		H(2in)-4	624.40	39.66	7.55	10.80	9.49
		H(2in)-5	924.52	63.19	7.69	10.88	9.83
		H(2in)-6	617.15	38.61	8.01	10.55	10.50
		H(2in)-7	1168.48	73.54	8.08	10.29	10.68
		H(2in)-8	538.65	37.56	7.91	10.44	10.19
		H(2in)-9	1376.21	89.88	8.77	12.38	12.02
		H(2in)-10	1975.85	86.73	8.39	12.28	10.32
		Avg	878.94	55.20	7.95	11.02	10.12
	Std Dev	501.38	22.56	0.38	0.72	0.84	
	0.5in	H(.5in)-1	1347.83	58.70	7.47	12.80	11.37
		H(.5in)-2	1373.19	71.14	7.41	12.80	11.06
		H(.5in)-3	1248.19	55.85	7.50	12.53	10.65
		H(.5in)-4	1711.35	63.72	7.45	12.37	11.25
		H(.5in)-5	2306.16	86.43	8.16	12.47	11.14
		H(.5in)-6	2657.00	87.78	8.22	12.74	11.11
		H(.5in)-7	2521.14	101.65	7.18	12.49	10.58
		H(.5in)-8	2085.14	86.73	8.26	12.54	11.59
		H(.5in)-9	2646.74	101.65	8.34	12.37	11.39
		H(.5in)-10	2983.70	101.65	8.10	12.52	11.66
Avg		2088.04	81.53	7.81	12.56	11.18	
Std Dev	630.64	17.98	0.44	0.16	0.36		

Figures 4.16 and 4.17 show the impact results for both the middle and high energies at both separation distances. Similar to Figure 4.2 the impact characteristics are scaled to the largest average of each type, i.e. the largest damage area is represented as one and is used to normalize the smaller value of the pair. Consider the multiple impacts separated by 2in at the middle energy level from Tables 4.7 and 4.8. The average damage diameter of the first impact is 33.23mm with an 8.63mm standard deviation; the average and standard deviation of the second impact is 32.22mm and 13.86mm , respectively. Since the average diameter of the first impact is the largest of the set, it becomes the normalizing magnitude. Therefore, its normalized value becomes 1.00 ± 0.260 and the normalized value of the second impact is 0.970 ± 0.417 . The p-value for each pair of data is also presented. The p-value is a measure of the difference between the ranges of values for comparative data sets. A p-value below 5% suggests that the distribution of the data points for each set is distinctly different, that is, it would be expected for a data point of one set to fall outside the range of the other. A p-value above 5% suggests that the variability between the two distributions can be attributed to random chance, or that a single data point could be associated with both data sets.

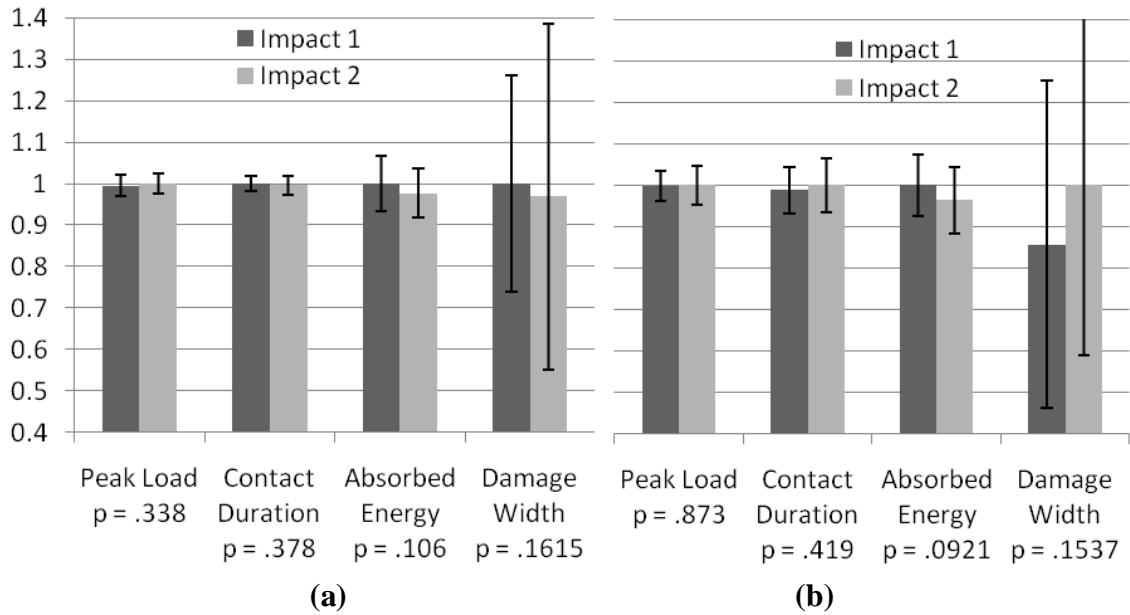


Figure 4.16 Impact characteristics for two impacts separated by 2in at (a) middle and (b) high energies.

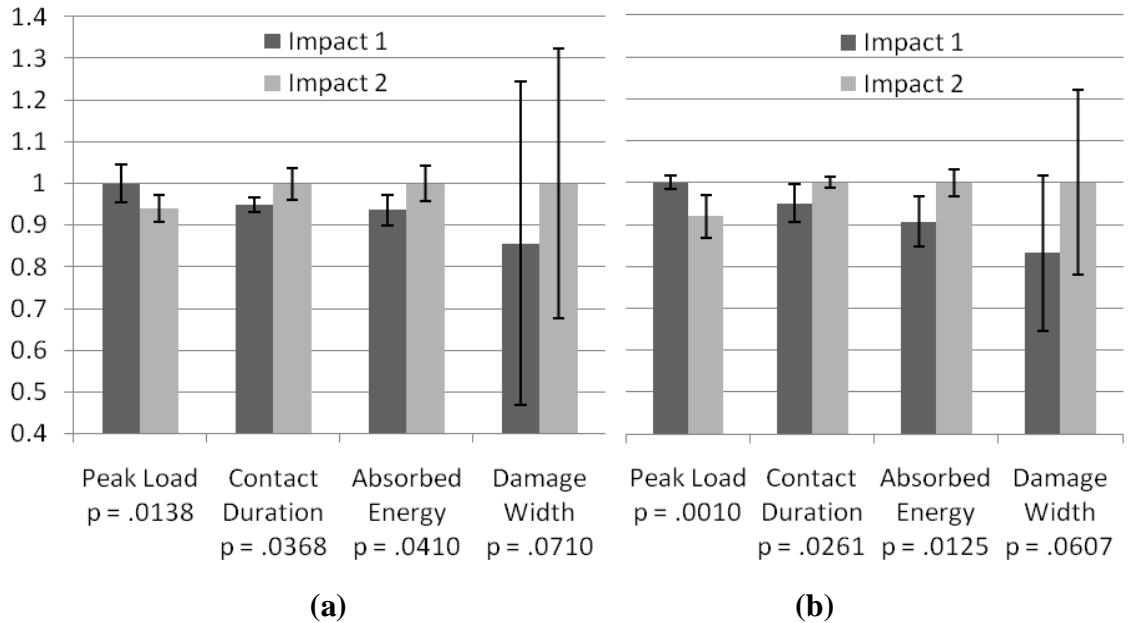


Figure 4.17 Impact characteristics for two impacts separated by 0.5in at (a) middle and (b) high energies.

It is clearly evident in Figures 4.16 that the impacts separated by 2in, for both energies, have similar impact characteristics. None of the impact characteristics generated by the second impact appear affected by the damage of the first. This is supported by the fact that the p-values far surpass 5% and the confidence intervals significantly overlap. The 0.5in separation, however, reveals a distinct difference between the characteristics of the first and second impacts.

Visually, the damage at 2in due to both impacts is similarly sized and displays no overlap. The damage of the initial impact site does not appear to change dimensions as a result of the second impact; this will be addressed in the following section. When the initial site is displaced from the center of the support span, its effect on the global stiffness loss may be minimized for the following impact event. The short duration over which the impact takes place may reduce its sensitivity to the subtle structural variations introduced by previously existing damage at a remote location. Thus, there is little disparity between the characteristics of impacts separated by 2in.

At 0.5in, on the other hand, the impact damage is allowed to significantly overlap. The increase in contact duration, absorbed energy, and damage width and the decrease in peak load as seen in Figure 4.17 suggest that this overlap in damage increases the compliance of the material. This in turn suggests that a greater degree of damage is formed during the overlapping event. As opposed to the 2in impacts, the local and global effects of the initial impact appear to directly influence the characteristics of the following impact. Stress concentrations introduced by the delaminations and transverse/interlaminar matrix cracks already present allow similar damage to propagate

more readily. The formation of more extensive damage may contribute to the loss of overall stiffness and larger energy absorption suggested in Figure 4.17. The particular effect of the multiple impacts on damage formation and mechanical properties will be discussed in the following sections.

4.4.2 Damage Evaluation

As mentioned in the previous section, each sample is scanned after each impact. A separation distance of 2in was chosen to produce two distinct damage areas, such that there is no interaction between these two zones. Conversely, a 0.5 in separation distance was selected to induce the overlap of the two sites. Visual inspection of the impacts supports the decision of the distances but as is inherent of composite materials, certain damage types can remain essentially invisible. While the C-scan cannot distinguish the intensity or type of the internal damage, it can clearly display the overlap of the delaminated area. The results for damage area and width after each impact are tabulated in Tables 4.7 and 4.8 of the previous section for the 99.9% threshold.

While it is clear in Figure 4.11 of the previous section that the influence of the second impact at 0.5in tends to be larger, it is not clear whether the damage of the first impact grows as a result of the second impact. Figure 4.18 show that the impact sites separated by 2in produced distinct damaged areas. The first impact does not show a tendency to grow as a result of the second impact. The second impact is also not consistently larger or smaller than the first, suggesting that the impact events are independent of each other. At 0.5in, however, these areas significantly overlap. By overlaying the scans of the first impact onto that of the second at 0.5in it can be seen that

initial damage grows predominantly in the direction of the secondary impact site (Figure 4.19). Only portions of the initial damage adjacent to the second impact expand, but become indistinguishable from the coalesced damaged regions. The maximum diameter is consistently larger after the second impact, likely due to the propagation from the initial damage.

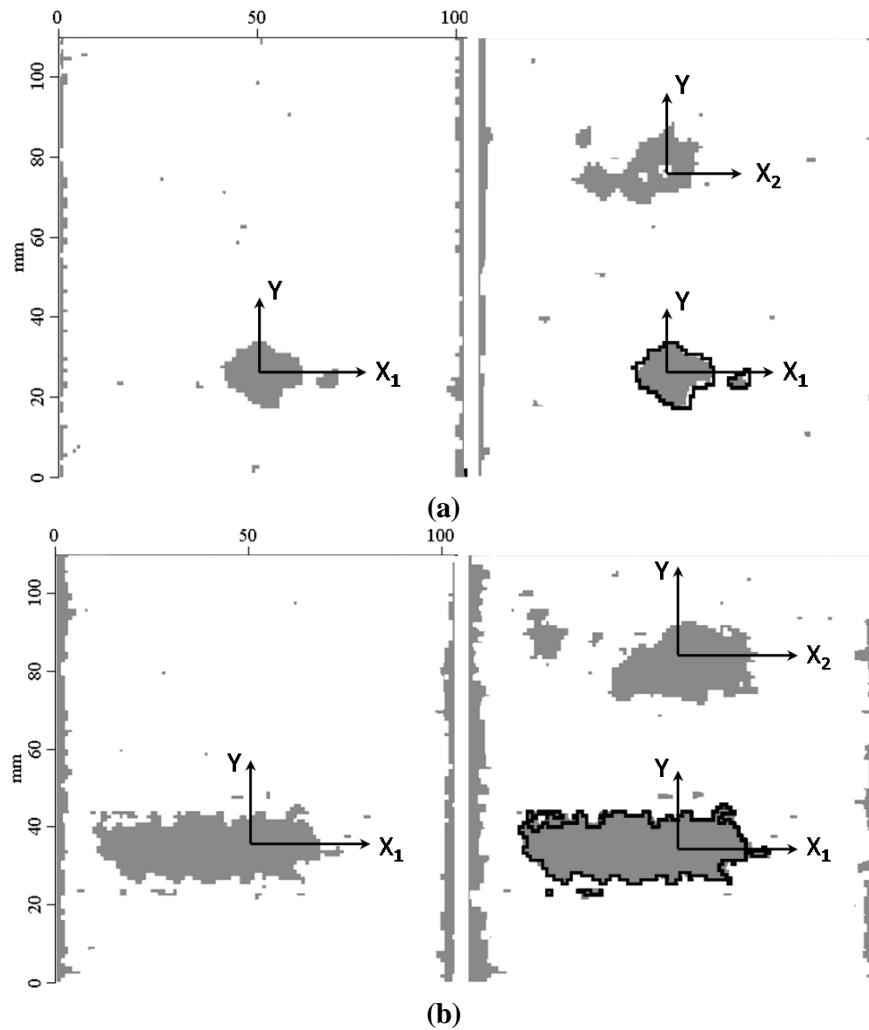


Figure 4.18 C-scans of the damage in samples impacted with a 2in separation show two distinct damage regions with no overlap for both the (a) middle and (b) high energies.

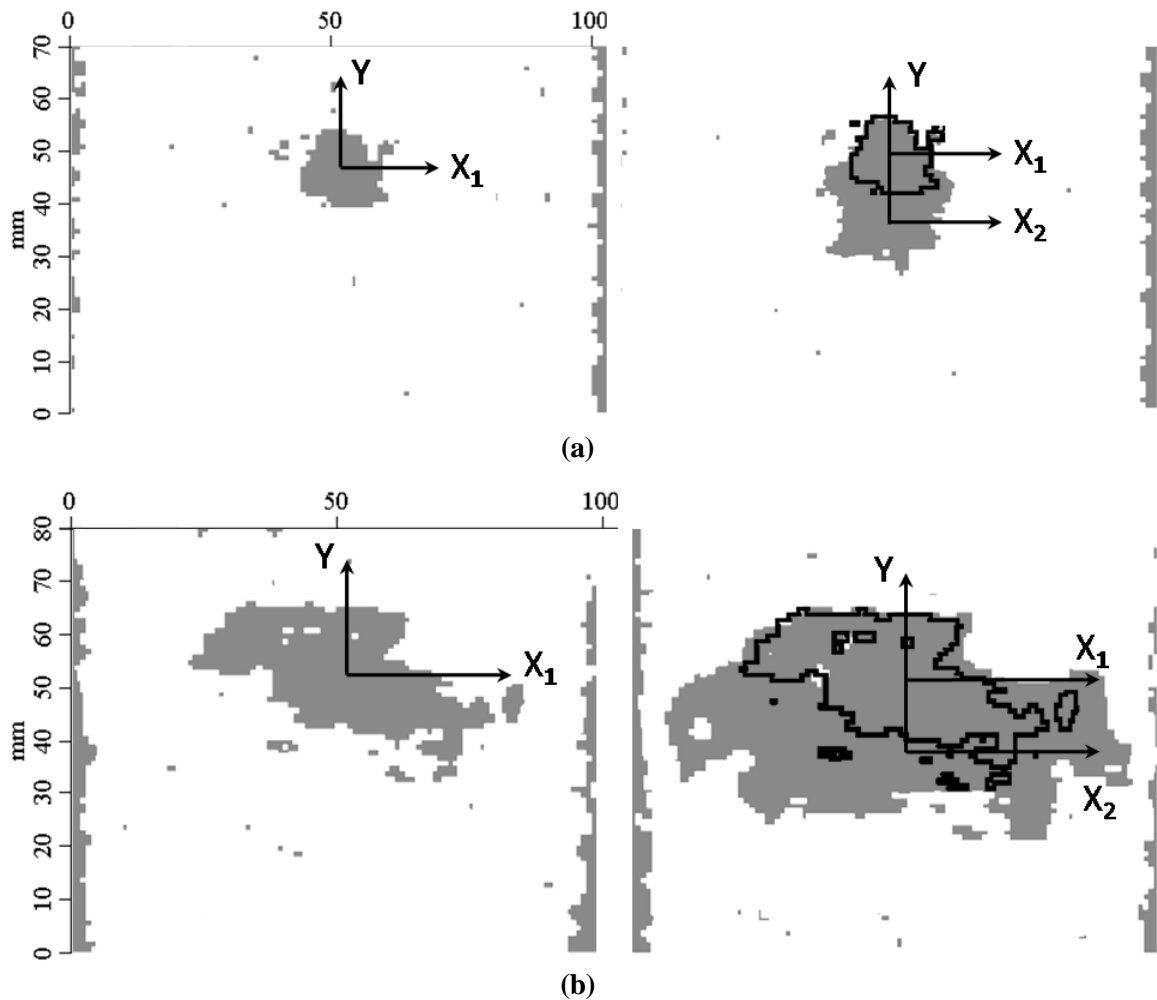


Figure 4.19 An overlay of the initial damage caused by (a) middle and (b) high impact energy shows that the bulk of its growth coincides with the formation of the second damage region.

Just as in Section 4.3.2, sectional cuts were taken of representative samples to visualize the extent and types of damage within the material. The sections for the multiple impacts, however, are taken through the midpoint between the impacts sites. Figure 4.20, shows a comparison between the sections of the multiple impacts for both the middle and high energies. At the middle energy the delaminations appear to be more

expansive for the multiple impacts than for single (Figure 4.6) with a small increase in number. At the high energy, not only are there more delaminations but they tend to be larger, and the degree of matrix cracking is much more extensive. Again, the damage seems to manifest in a conical pattern through the thickness. Though the delaminations appear to be of similar shape, the largest occur closer to the back face. More tensile and transverse matrix cracking also occurs farther from the impacted face. The C-scan is unable to distinguish the different failure types and only captures the largest envelope of damage. Thus, the images evaluated from these tests typically represent the largest delamination envelope. Due to the conservative nature of the FE modeling, this may be suitable for approximating the residual mechanical response of the damaged plate.

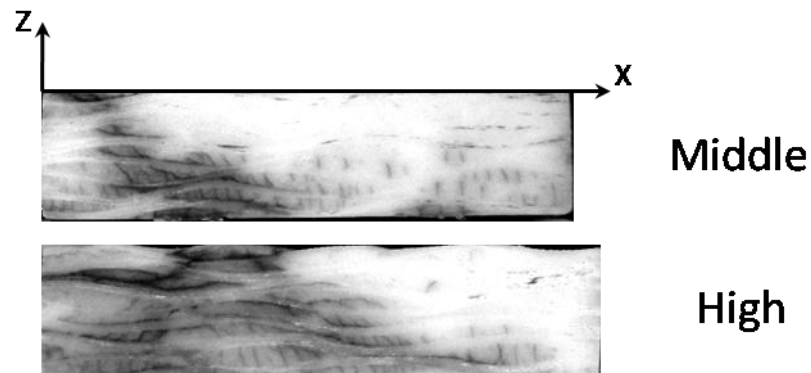


Figure 4.20 Sections through the damage of samples impacted twice with a 0.5in separation show a greater degree of matrix cracking on the back surface as well as more severe delaminations than those with a single impact (Figure 4.6): 3x magnification.

4.4.3 Post-Impact

Since Figure 4.17 suggests that an impact at 0.5in from another impact site has different characteristics than the first, it would follow that the material experienced a degradation of properties. In this series of tests, the modulus of the sample after the first and second impacts can be compared. Since flexural and residual compressive strength measurements require destructive methods they will only be compared after the second impact

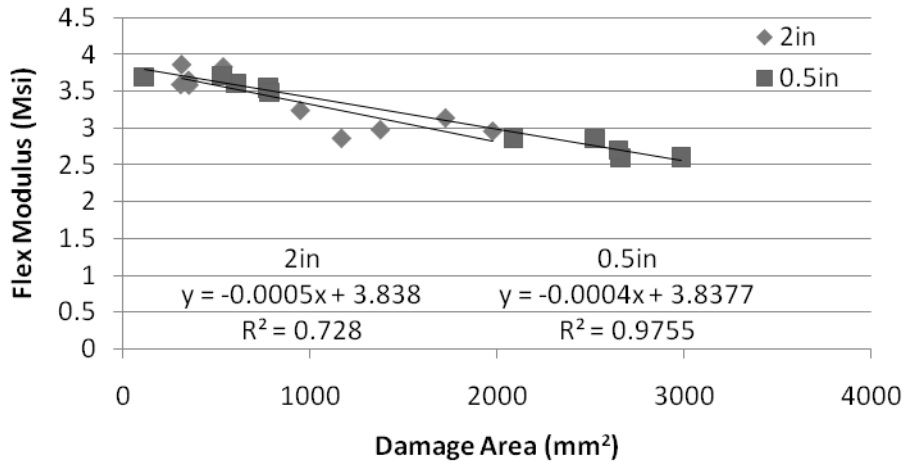
Samples were trimmed for the CAI such that the midpoint between the two impact sites was at the center of the sample. Again a precision surface grinder with a diamond coated circular blade was used to ensure squareness of the final dimensions. For FAI the midpoint was centered between the loading noses. The 2in separation was also selected to retain the entire damaged areas within the 3in span of the loading noses. Results from the CAI and FAI tests are presented in Tables 4.11 and 4.12, respectively.

Table 4.11 CAI results for samples damaged by two impacts separated by 2in and 0.5in at middle and high energies.

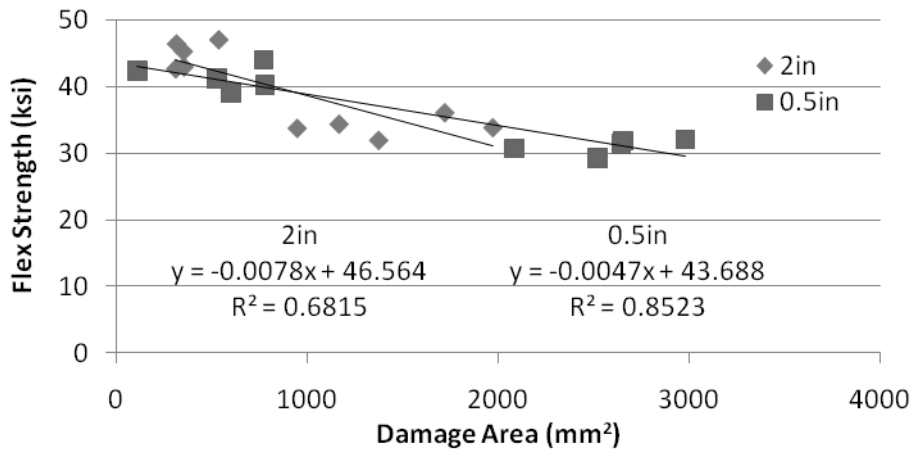
CAI				
Impact Energy	Separation Distance	Sample ID	Max Load (lbf)	Strength (ksi)
Nominal		N-1	8287	36.80
		N-2	7943	35.66
		N-3	8095	36.21
		N-4	8210	36.49
		N-5	8036	35.84
		Average	8114	36.20
Std Dev	137	0.46		
Middle	2in	M(2in)-1	24129	26.81
		M(2in)-2	23824	27.07
		M(2in)-3	23096	25.95
		M(2in)-4	25025	27.50
		M(2in)-5	23933	26.89
		Avg	24001	26.84
	Std Dev	693	0.57	
	0.5in	M(.5in)-1	21825	24.25
		M(.5in)-2	21094	23.97
		M(.5in)-3	17968	20.19
		M(.5in)-4	19686	21.63
M(.5in)-5		22117	24.85	
Avg	20538	22.98		
Std Dev	1717	1.98		
High	2in	H(2in)-1	19578	21.75
		H(2in)-2	16736	19.02
		H(2in)-3	17423	19.58
		H(2in)-4	17773	19.53
		H(2in)-5	18112	20.35
		Avg	17924	20.05
	Std Dev	1055	1.07	
	0.5in	H(.5in)-1	16975	18.86
		H(.5in)-2	15050	17.10
		H(.5in)-3	16318	18.34
		H(.5in)-4	16656	18.30
H(.5in)-5		14337	16.11	
Avg	15867	17.74		
Std Dev	1125	1.12		

Table 4.12 Residual flexural properties after two impacts separated by 2in and 0.5in at the middle and high impact energies.

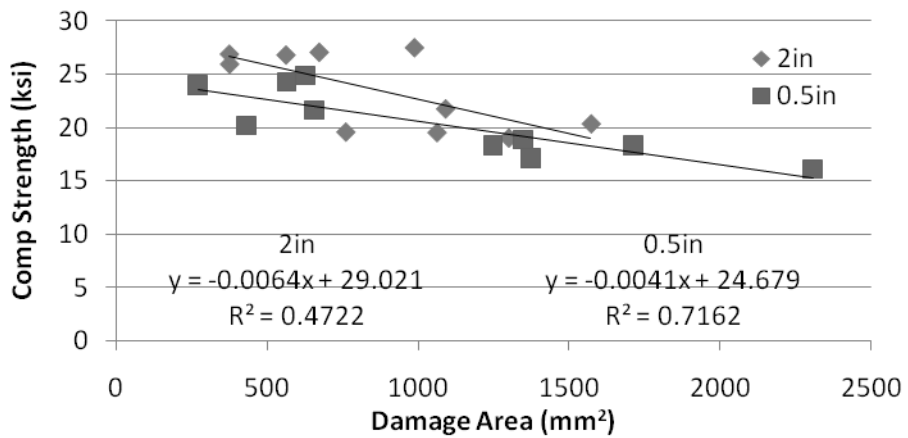
FAI							
Impact Energy	Separation Distance	Sample ID	Max Load (lbf)	Deflection @ Max Load (in)	Apparent Modulus		Strength (ksi)
					Impact 1 (Msi)	Impact 2 (Msi)	
Nominal		N-6	2258	0.422	4.52		51.63
		N-7	2068	0.461	4.18		47.40
		N-8	2336	0.408	4.34		53.36
		N-9	2319	0.411	4.29		52.97
		N-10	2115	0.451	4.06		48.45
		Average	2219	0.431	4.28		50.76
Std Dev	121	0.024	0.17		2.69		
Middle	2in	M(2in)-6	1865	0.448	3.77	3.60	42.72
		M(2in)-7	1878	0.445	3.88	3.59	42.99
		M(2in)-8	1982	0.422	3.75	3.65	45.32
		M(2in)-9	2061	0.406	3.68	3.83	47.07
		M(2in)-10	2033	0.411	3.92	3.87	46.45
		Avg	1964	0.426	3.80	3.71	44.91
	Std Dev	89	0.019	0.10	0.13	1.98	
	0.5in	M(.5in)-6	1894	0.449	3.96	3.69	42.38
		M(.5in)-7	1971	0.432	3.78	3.55	44.08
		M(.5in)-8	1798	0.473	3.74	3.48	40.25
		M(.5in)-9	1750	0.486	3.75	3.60	39.17
		M(.5in)-10	1844	0.461	3.81	3.71	41.26
Avg		1851	0.460	3.81	3.61	41.43	
Std Dev	86	0.021	0.09	0.10	1.90		
High	2in	H(2in)-6	1477	0.437	3.17	3.24	33.80
		H(2in)-7	1505	0.429	3.21	2.86	34.42
		H(2in)-8	1582	0.408	2.90	3.14	36.13
		H(2in)-9	1395	0.462	3.23	2.98	31.99
		H(2in)-10	1481	0.436	3.05	2.96	33.89
		Avg	1488	0.434	3.11	3.04	34.05
	Std Dev	67	0.020	0.14	0.15	1.48	
	0.5in	H(.5in)-6	1434	0.460	3.13	2.59	31.86
		H(.5in)-7	1319	0.500	3.30	2.86	29.30
		H(.5in)-8	1384	0.477	3.41	2.87	30.75
		H(.5in)-9	1414	0.467	3.20	2.70	31.42
		H(.5in)-10	1444	0.457	3.10	2.60	32.09
Avg		1399	0.472	3.23	2.72	31.09	
Std Dev	50	0.018	0.13	0.13	1.12		



(a)



(b)



(c)

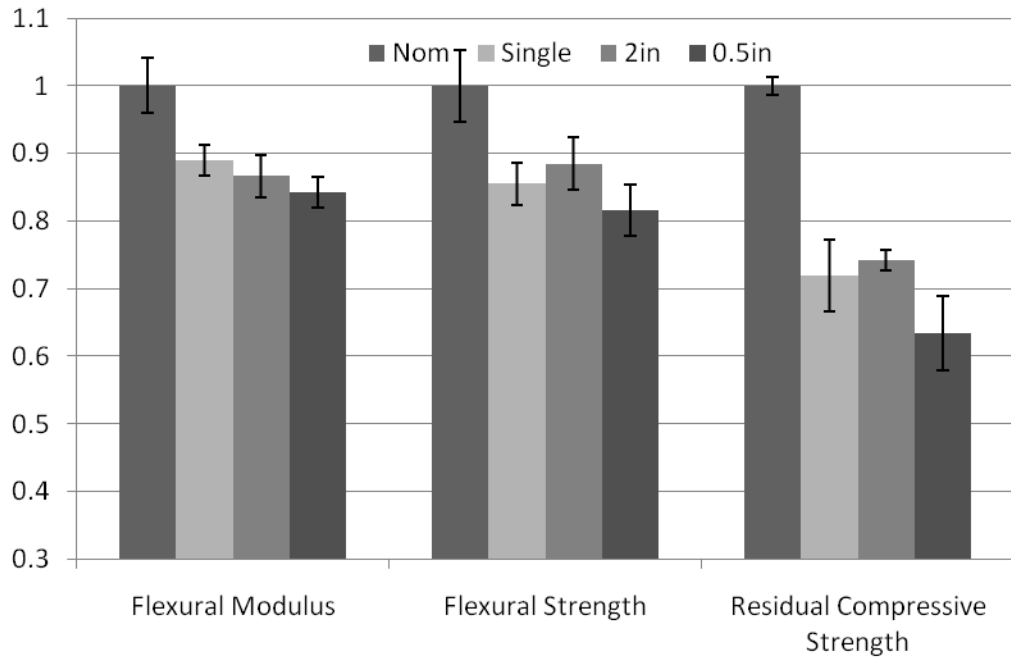
Figure 4.21 Plot of residual (a) flexural modulus, (b) flexural strength, and (c) compressive strength against maximum damage area.

In order to gauge the utility of the FAI method it can be compared to the results of CAI, which is a traditional means to measure impact damage tolerance. Since CAI is known to be sensitive to the size of impact-induced delamination, it can be used as a baseline to judge the sensitivity of the residual flexural modulus and strength. Figure 4.21c plots the residual compressive strength of the multiple impact samples against the corresponding damage area. The sensitivity may be represented by the slope of the regression line, which is -0.0064 for the 2in impacts. The low consistency associated with CAI ($R^2 = 0.47$) may be partially attributed to the significant scatter in the original impact and damage data. The overall CAI strength is reduced by approximately 40% at the largest damage area. The flexural strength has marginal consistency ($R^2 = 0.68$) to a slope of -0.0078 that corresponds to a strength reduction of approximately 35%.

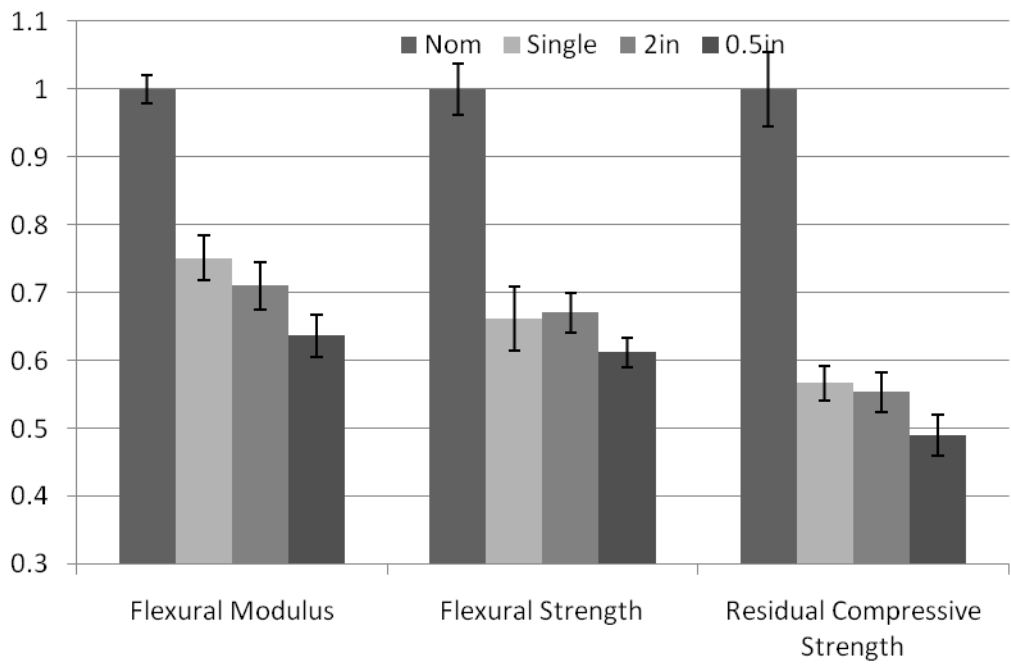
The modulus data shows good consistency ($R^2 = 0.73$) with an approximate 25% reduction at the highest damage area. Though less sensitive than CAI, the consistency of the modulus data suggests that the tests are repeatable and show a particular degree of sensitivity to the damage size. The same comparison can be made with the 0.5in data, which displays a significant increase in consistency. Considering this consistency and the unique sensitivities of the flexural strength and modulus, the FAI method may be a feasible option for damage tolerance testing.

A normalized comparison of the post-impact results is presented in Figure 4.22. The results from the single impacts are used to compare the effect of multiple impacts. At the middle energy (Figure 4.22a) there is a 13% and 16% reduction from the average nominal modulus for the 2in and 0.5in impacts, respectively. This also corresponds to a

2% and 5% reduction from the single impact modulus. It is clear that two impacts significantly reduce the flexural modulus from the undamaged value. There is significant overlap, however, between the distributions of the single and multiple impacts, but the monotonically decreasing average suggests that there may be a distinct effect from the impact proximity. At the high energy (Figure 4.22b) the loss of modulus is more pronounced. The 2in and 0.5in impacts have a 4% and 11% reduction, respectively, from the modulus of the single impacts. Their distributions appear more distinct than at the middle energy, which supports the assumption that impact proximity influences the residual properties. The greater loss of modulus associated with the 0.5in impacts may be attributed to the greater extent of damage resulting from the interaction of the damage sites. While the 2in separated impacts produce more damaged material, the extent of damage generated by the 0.5in impacts seems to be of greater influence on the impact and post-impact properties.



(a)



(b)

Figure 4.22 Comparison of normalized residual properties for the (a) middle and (b) high impact energies at separated locations.

There appears to be little difference between the residual flexural strength of the single and 2in impacts at both impact energies. This may be a result of the stress concentrations induced by the damage site. Since the 2in separated impacts do not interact, their resulting damage regions each may be similar to those generated by a single impact. Therefore, the concentration of stress adjacent to the damage regions of the separated impacts should be similar to that caused by the single impact site. Strength reductions from the 0.5in impacts, on the other hand, appear more significant. There is a 4% and 5% reduction from the single impact strength for middle and high energies, respectively. This corresponds to an 18% and 39% overall reduction from the nominal flexural strength. As previously discussed, this may be attributed to the greater extent of damage induced by the coalescing damage sites. Typical failed samples are shown in Figure 4.23.

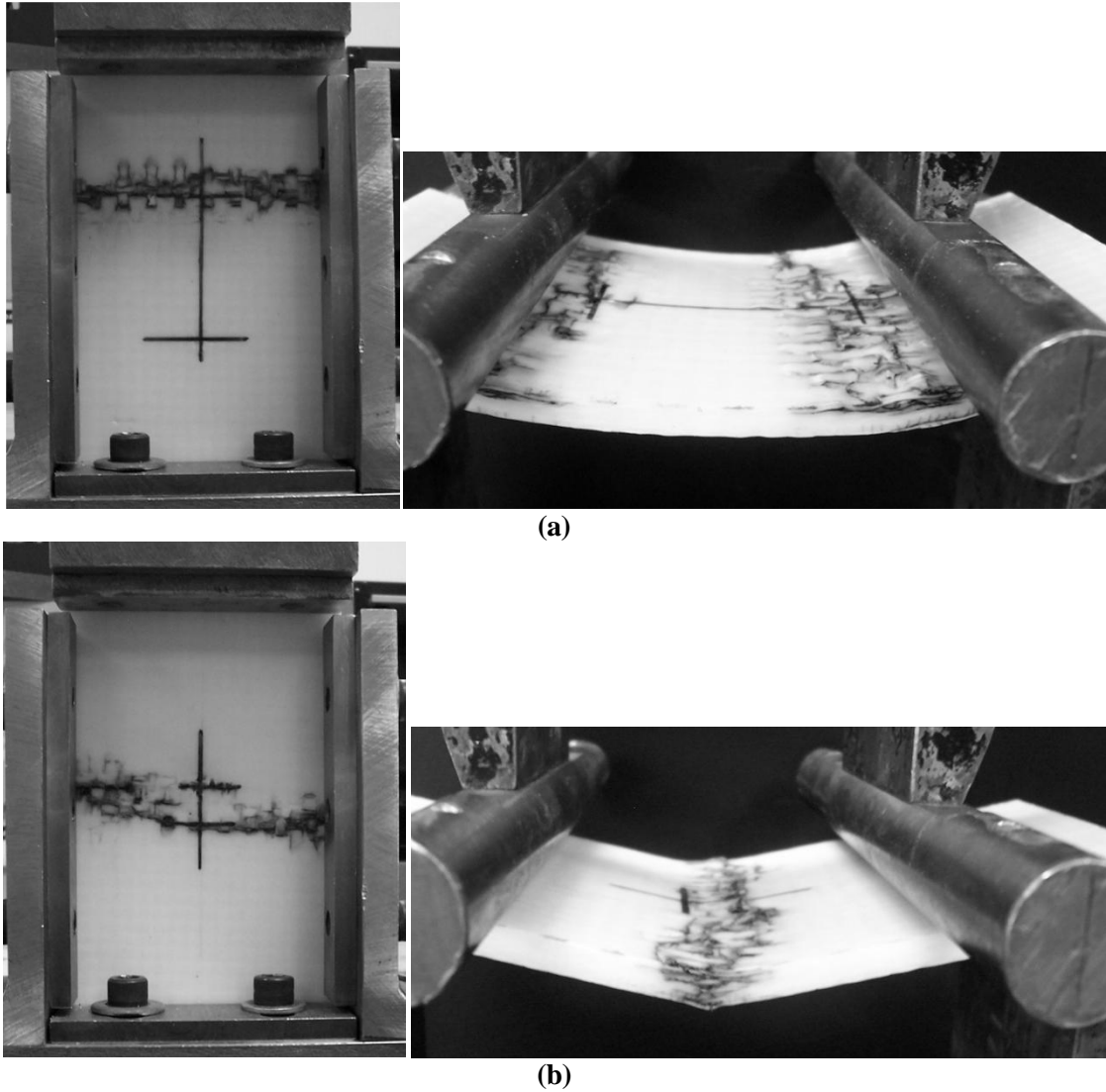


Figure 4.23 Failed CAI and FAI samples for the (a) 2in and (b) 0.5in separated impacts.

The same arguments can be made for the residual compressive strength. There appears to be little difference between the value of the single and 2in impacts. Since each of the 2in impacts produce damage with similar size and extent as the single impact, the stress concentrations are likely to be similar. At 0.5in, however, the extent of damage has

been found to be greater than that of the single impact. Larger and a greater number of delaminations are recorded as well as more matrix cracking; CAI is known to be sensitive to the size of delaminations. Thus, the residual compressive strength of the 0.5in separated impacts is expected to be lower than for a single impact. The middle energy shows a 36% reduction from the nominal compressive strength and an 8% from the single impact strength. A 51% from nominal and 8% from single strength reductions are observed for the high impact energy. The extent to which the damage size and proximity influence the concentration of stress will be explored in the following section.

4.4.4 FEA of Residual Performance after Multiple Impacts

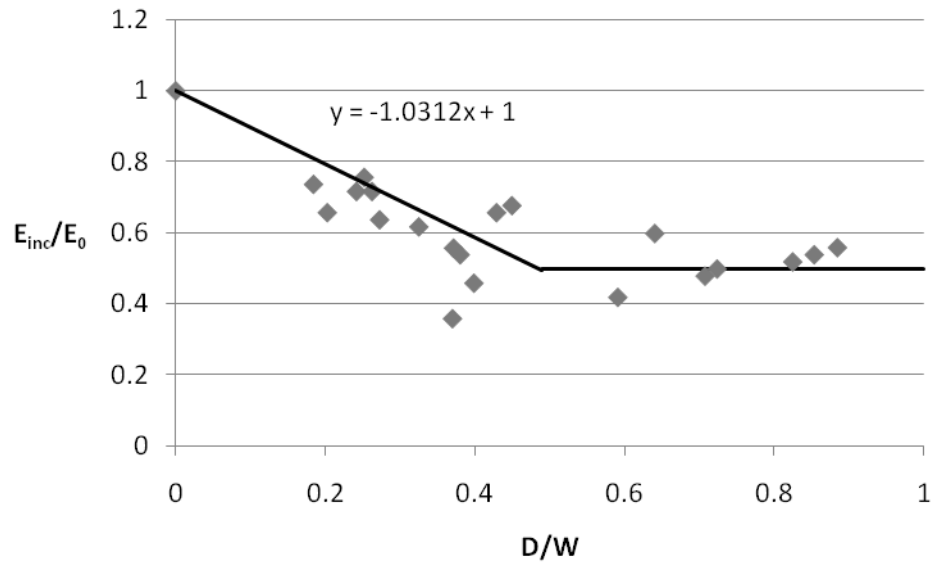
Similar to the procedure in Section 4.3.4, the damage areas were modeled as circles and ellipses. For impacts separated by 0.5in, an equivalent elliptical inclusion area was modeled at the center of the plate. The stiffness within the inclusion was adjusted such that the apparent flexural modulus of the model matched the experimental value. For the 2in separated impacts, however, the inclusions were assumed to be symmetrically displaced from the center axis. Since the flexural modulus was measured after the first impacts, the same process to determine the inclusion stiffness of the single impacts was used. The stiffness of the second inclusion was then adjusted to determine the final apparent modulus.

Similar to the results in Section 4.3.4 for a single impact, Figure 4.24 shows a bilinear trend between inclusion stiffness and damage width for both separation distances. As discussed in Section 4.3.4, the plateau suggests that the geometry of the inclusion begins to take precedence over the loss of stiffness. However, the combination of a larger

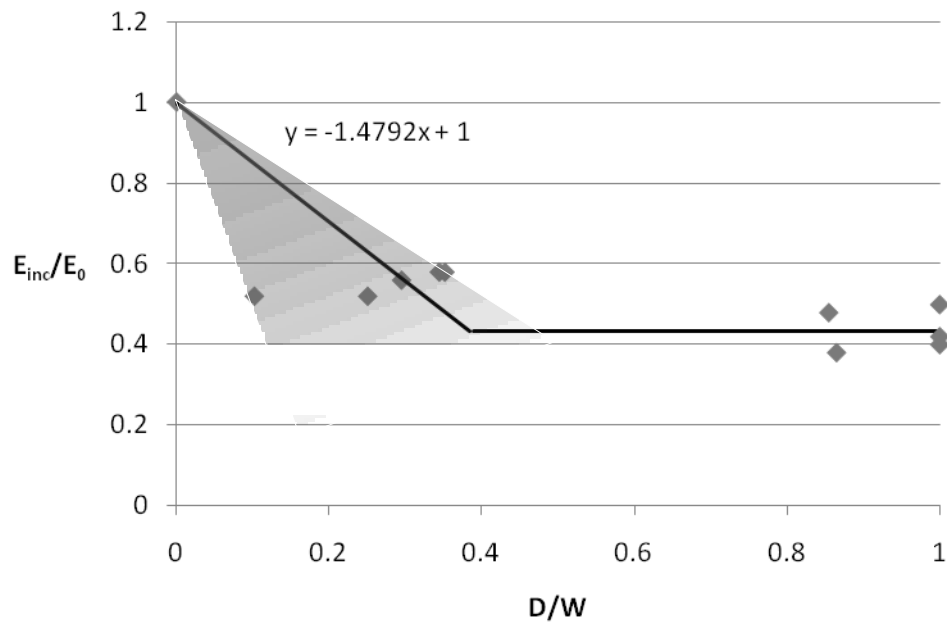
inclusion with a smaller change in stiffness continues to produce a monotonic loss of apparent modulus as seen in Figure 3.14. The slope of the initial trendlines for the single (Figure 4.9), -1.02, and 2in separated impacts, -1.03, are roughly equivalent. This is reasonable since the 2in distance was chosen such that the damage regions do not overlap. Therefore, the loss of modulus is the result of two distinct inclusions with properties similar to those of a single impact at the same energy. While the trendline of the 2in separated impacts appears to plateau at a slightly higher inclusion stiffness than the single, significant scatter makes it difficult to draw and substantial conclusions.

The slope of the regression line for the 0.5in separated impacts, however, is significantly steeper, -1.48. This suggests that for similar damage diameters, 0.5in separated impacts produce a single damage site with properties smaller than the inclusions of single or 2in separated impacts. This appears logical as the 0.5in distance was chosen to allow the two damage sites to overlap and interact. It may be more appropriate, however, to consider an envelope over the initial regression. The assumptions made when modeling the 0.5in separated damage sites do not account for the complex interactions that have likely occurred in the material. For consistency, however, the original slope will be used to later extrapolate the CAI stiffness values.

As discussed in Section 4.4.2, the extent of damage was greater than that of the single impact sites but showed only little growth from the initial impact especially at the middle impact energy, as seen in Figure 4.18. The plateau of the 0.5in impacts appears to also fall more consistently below the inclusion stiffness of the single impacts. This also suggests a greater degree of damage for similar inclusion sizes.



(a)

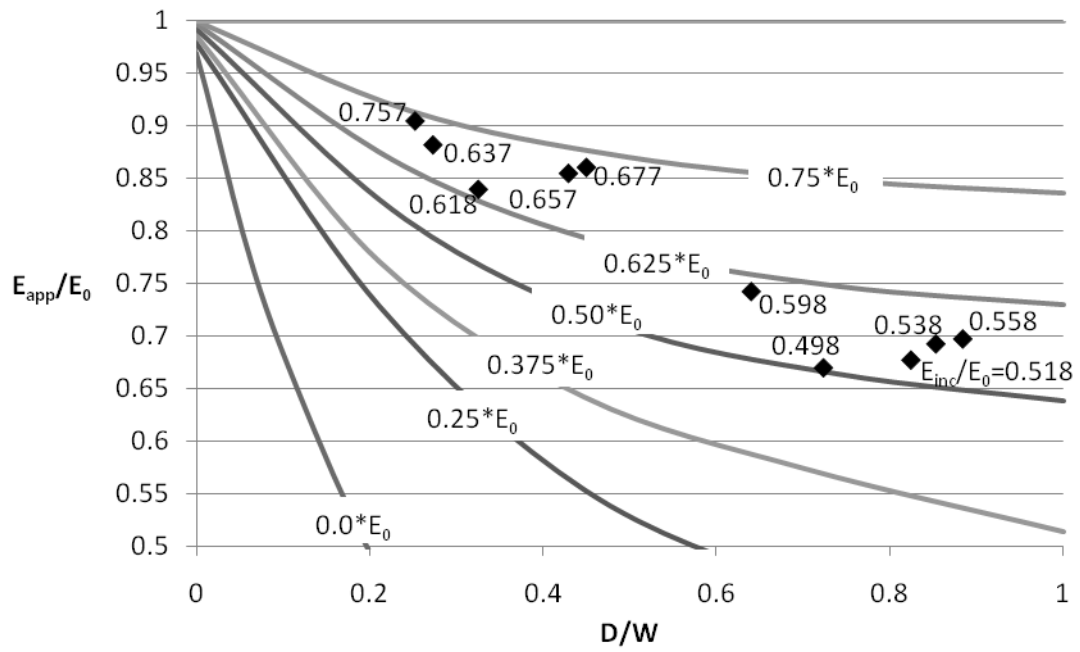


(b)

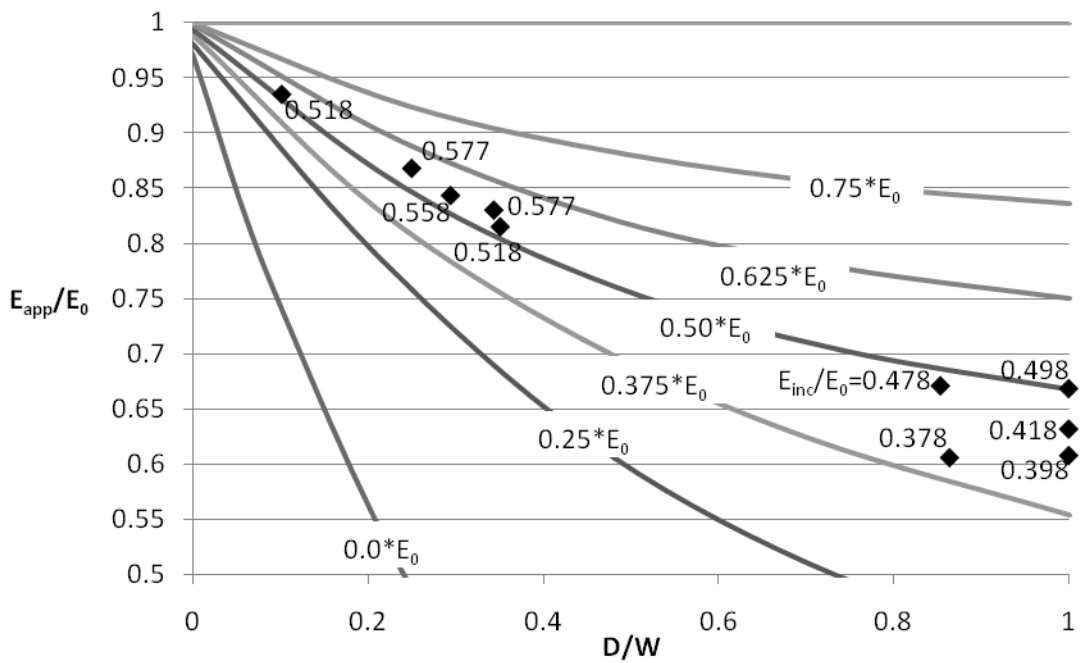
Figure 4.24 While the inclusions of the (a) 2in impacts have a similar slope and plateau as the single impacts, the loss of stiffness in the (b) 0.5in impacts appears more drastic with increasing damage diameter.

Just as for the single impact condition, the FE model can be initially compared to the experimental tests by overlaying their data on Figures 3.9, 3.11, 3.18, and 3.19. The model used to construct the inclusion stiffness curves in Figure 4.25a assumed both inclusions to have the same dimensions and stiffness. The experimental tests typically resulted in damage sites with different dimensions, and the modeling showed the corresponding inclusions to have different stiffness as well. Therefore, the experimental data may not be expected to correspond precisely with the FE predictions. In Figure 4.25a the experimental data points represent the largest diameter of the two damage regions, as it is typically associated with the lowest stiffness and highest stress concentration. They are also labeled with their corresponding inclusion stiffness. The model appears to show good agreement with the experiments since the data points seem to fall in the vicinity of the respective stiffness curve. This is also true in Figure 4.25b for 0.5in separated impacts.

Figures 4.26a and 4.26b compare the strength predictions of the FE model to the experimental results. As discussed in Section 4.3.4, the moment concentrations from the FE model ($K_M = M_{max}/M$) are considered equivalent to the ratio of undamaged strength (S_0) to residual strength (S_{FAI}); the surface membrane stresses that cause failure are directly proportional to the moments, and so their maximum ratios must be the same. The data points appear to fall within the proximity of the corresponding stiffness curves. This suggests that the model may be suitable for predicting the residual strength of plates with multiple inclusions. The degree of accuracy will be discussed in conjunction with Figures 4.27a and 4.27b.

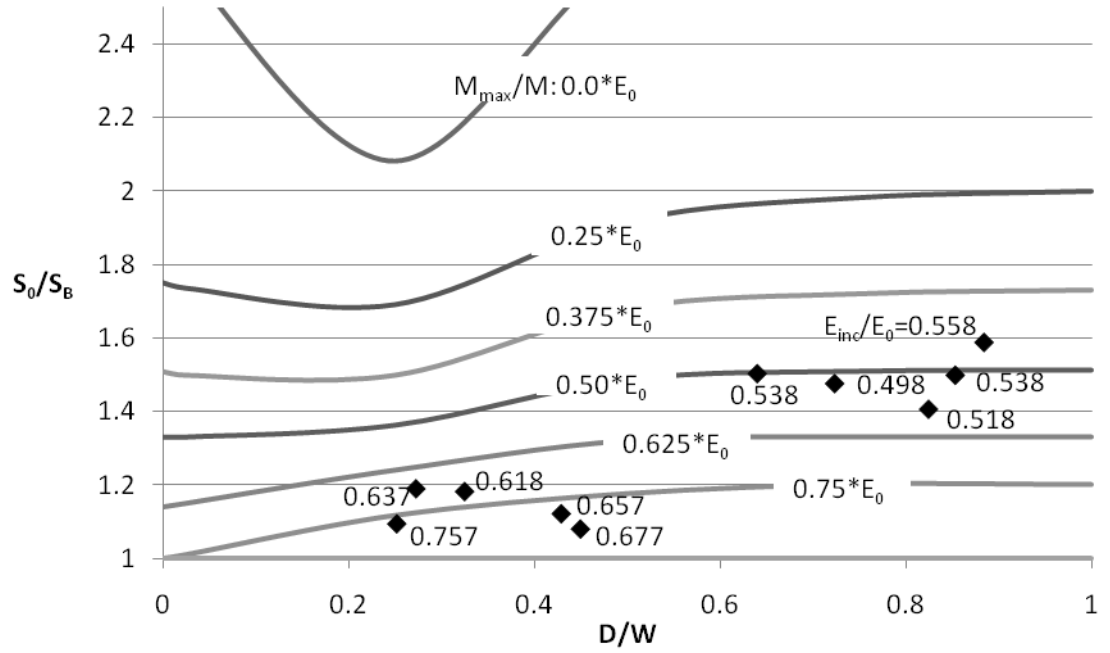


(a)

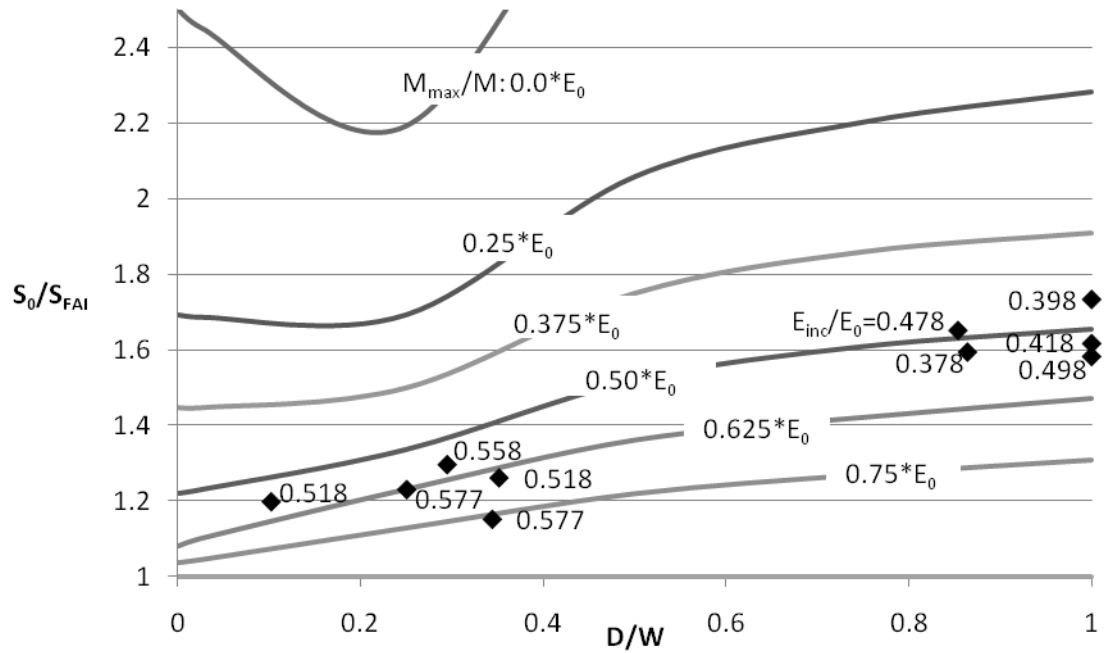


(b)

Figure 4.25 The experimental modulus data for (a) 2in and (b) 0.5in impacts show the effect of inclusion stiffness and diameter.



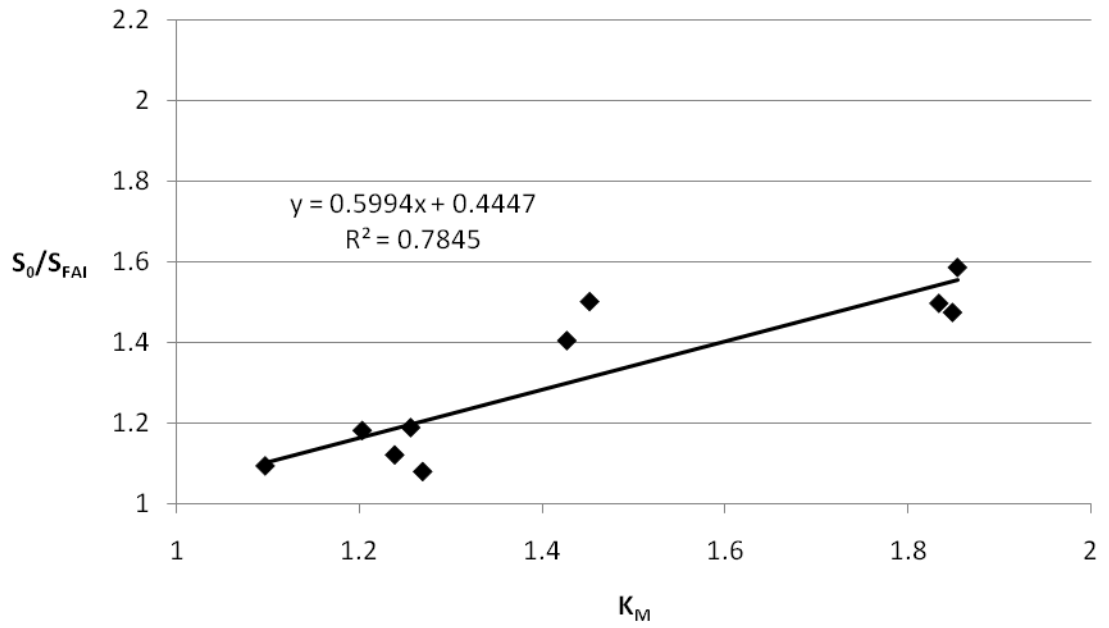
(a)



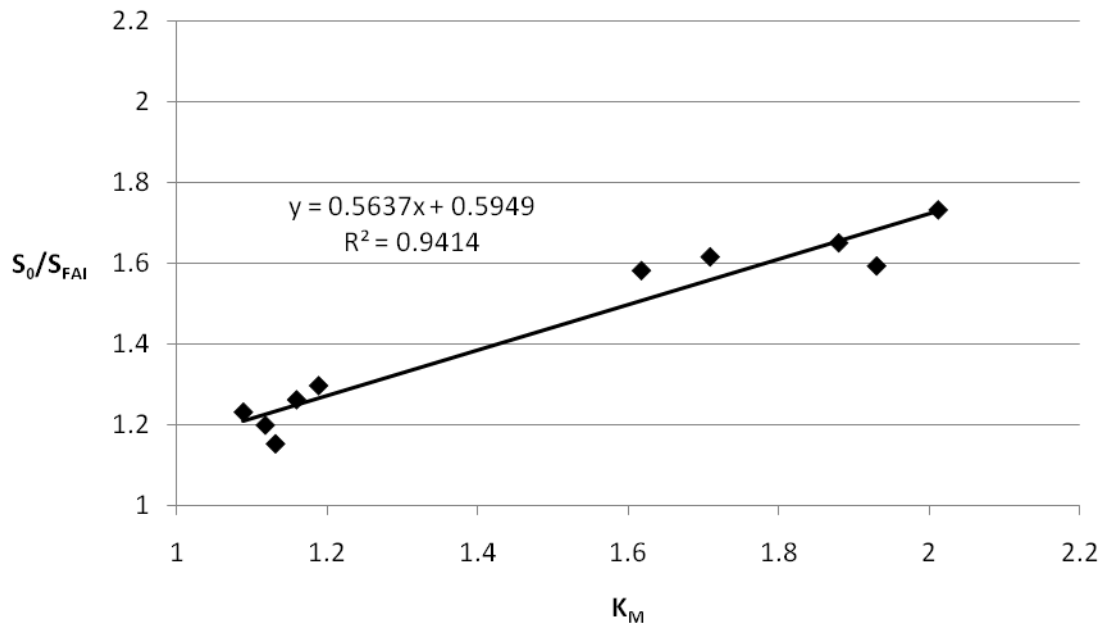
(b)

Figure 4.26 Though the experimental and FE stress concentrations for the (a) 2in and (b) 0.5in impacts may not exactly correspond, there is good agreement between the inclusion stiffness of the model and those read from the chart.

Figure 4.27 shows plots of FE moment concentrations against the experimental strength ratios. The model predictions for the 2in impacts (Figure 4.27a) correlate well ($R^2 = 0.78$) to a regression line with slope $m = 0.60$. The 0.5in predictions (Figure 4.27b) show a much stronger correlation ($R^2 = 0.94$) to a line with slope $m = 0.56$. If the model exactly predicted the residual strength then the slope would be one. Thus, the model appears to consistently underestimate the strength for both impact separations. The average percent difference of the FE results from the experimental data for the 2in and 0.5in impacts is $-9.9 \pm 10.1\%$ and $-2.2 \pm 11.5\%$, respectively. This seems to be a reasonable margin given the novelty of the tests and assumptions used to simplify the FE model.



(a)



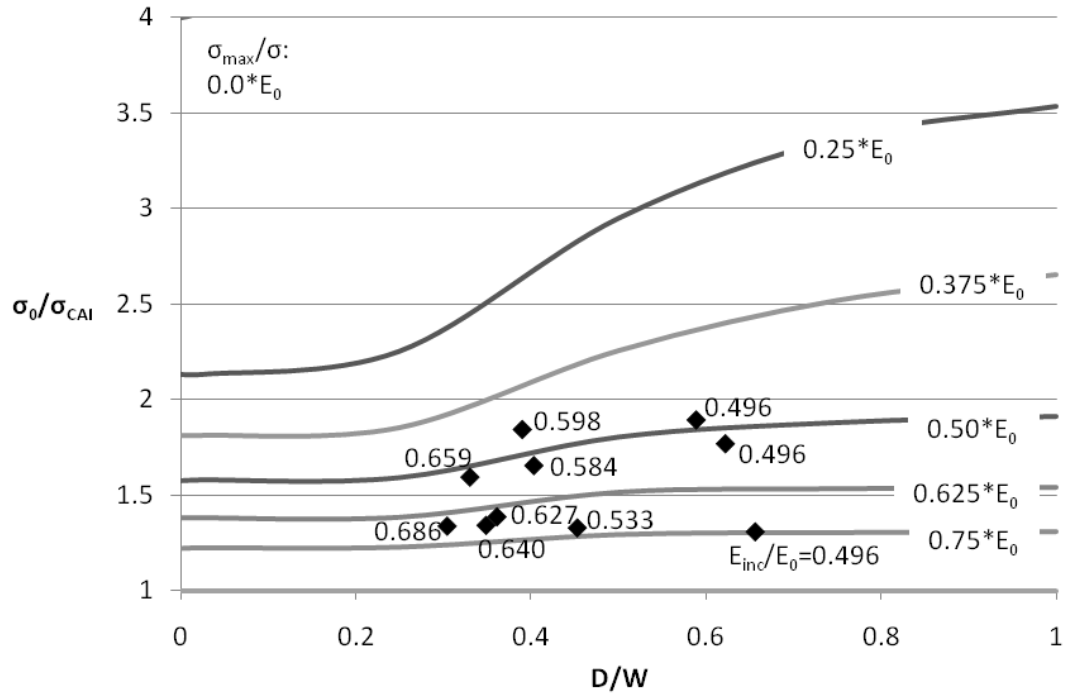
(b)

Figure 4.27 The (a) 2in and (b) 0.5in separated impacts show more disparity between experimental and FE stress concentrations, but they may still be considered suitable conservative approximations.

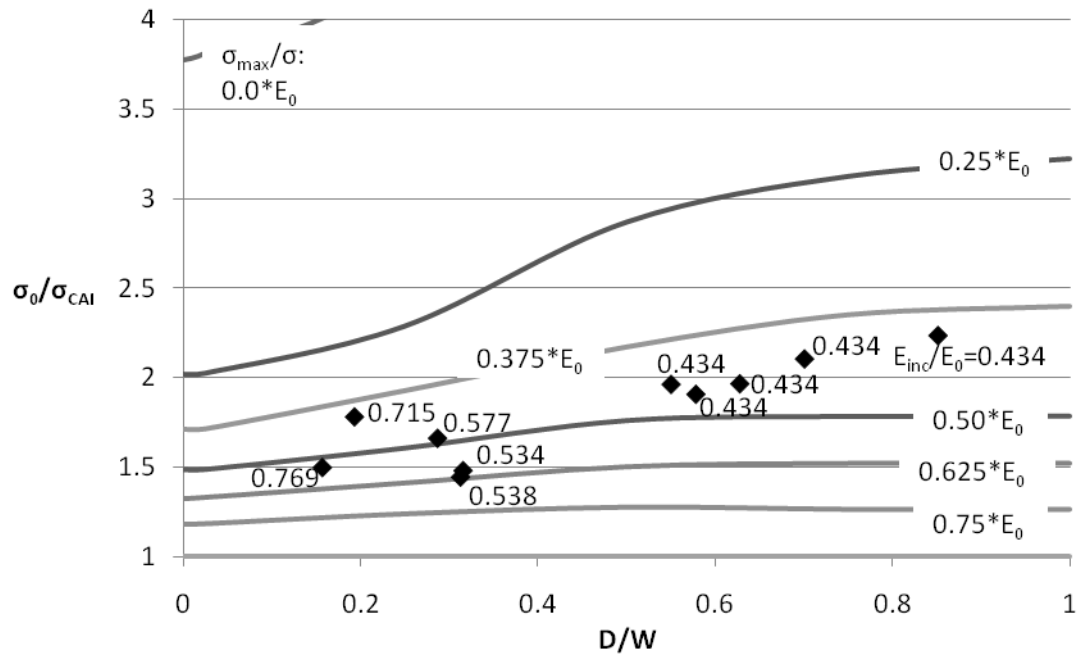
The model may also be used to estimate the loss of compressive strength by extrapolating the inclusion stiffness values for the CAI samples. Equations for the regression lines constructed in Figure 4.24 are used to extrapolate the inclusion stiffness for the damage dimensions measured in the CAI samples. In Figures 4.28, the experimental strength ratios (σ_0/σ_{CAI}) are plotted over the FE stress concentrations ($K_T = \sigma_{max}/\sigma$) for various inclusion sizes and stiffness. Due to the scatter of the original impact and damage data, the inclusion dimensions overlap for the middle and high impact energies in Figure 4.28a. However, the middle impact energy data shows higher inclusion stiffness for similarly sized inclusions. This is likely due to the greater extent of damage imparted by the high energy impacts, thereby reducing the inclusion properties.

There appears to be good correlation between the model and experimental data for both the 2in and 0.5in separated impacts, Figures 4.28a and 4.28b respectively. The experimental data points are labeled with their corresponding inclusion stiffness and fall roughly in the vicinity of the respective inclusion stiffness curve. There are some significant disparities, however, in the 0.5in plot (Figure 4.28b) for the lower inclusion sizes. As seen in the stiffness plateau in Figure 4.24b, an envelope of stiffness values was created to account for the simplifying assumptions used to model the 0.5in impacts. The scatter within this region combined with the scatter of the original damage and CAI data could explain some of the discrepancies seen in the plot. The plateau region, however, displayed much more consistency, which can be seen for the larger inclusions in Figure 4.28b.

Figure 4.29 is constructed to more clearly show the relationship between the FE model and experimental data. By plotting the FE stress concentrations against the experimental strength ratios (Figure 4.29) it is easier to see the accuracy of the FE model predictions; a slope of one suggests that the model was able to precisely predict the experimental loss of strength. Data for the 2in separated impacts (Figure 4.29a) show a strong correlation ($R^2 = 0.88$) to a regression line with slope $m = 0.99$, suggesting that the model slightly underestimates the residual strength. The 0.5in impacts (Figure 4.29b) have a strong correlation ($R^2 = 0.81$) to a line with slope $m = 0.92$, which also tends to slightly underestimate the strength. The percent difference of the FE results from the experimental data is $6.3 \pm 9.4\%$ and $3.6 \pm 4.9\%$ for the 2in and 0.5in impacts, respectively. All this suggests that while the model does not precisely predict the residual compressive strength of an impact-damaged composite, it at least provides good approximations that follow a consistent trend. Therefore, alone or with suitable correction factors, flexural modulus data combined with a simple elastic FE model can generate conservative strength estimates of damaged plates.

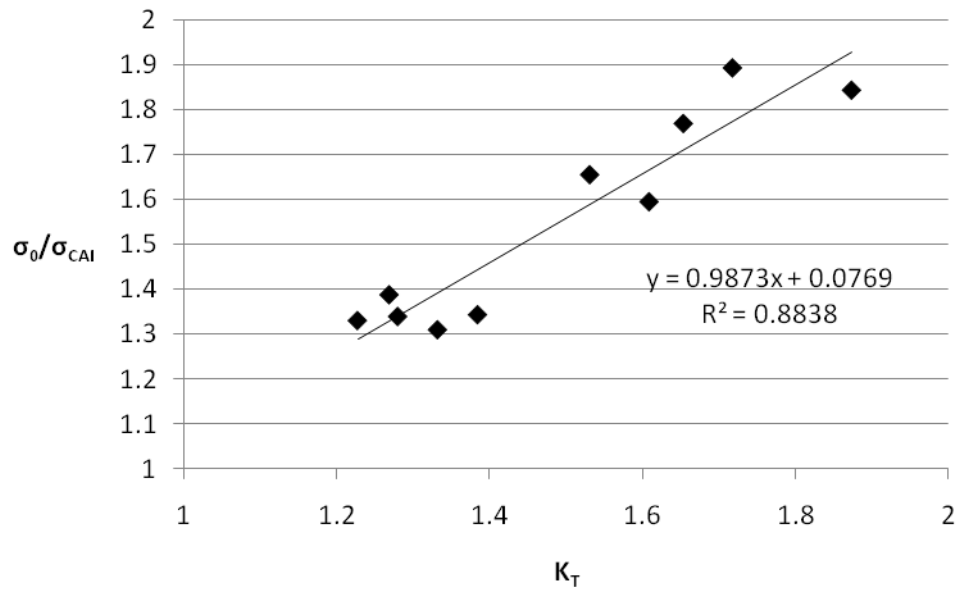


(a)

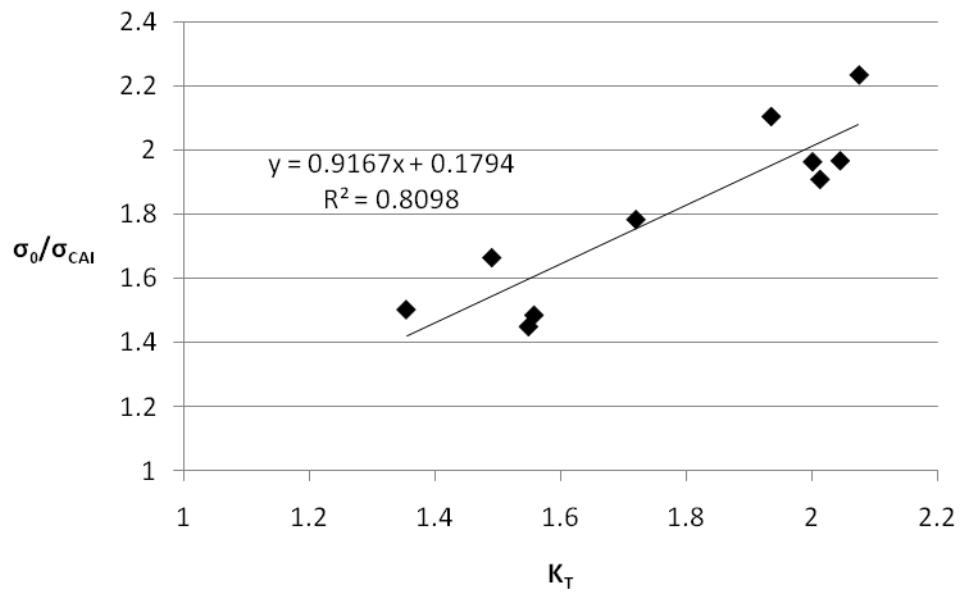


(b)

Figure 4.28 Though the exact stiffness for the (a) 2in and (b) 0.5in impacts is not known, values read from the design charts seem reasonable compared to the flexure models.



(a)



(b)

Figure 4.29 While there is a greater disparity between the in-plane stress concentrations for the (a) 2in and (b) 0.5in impacts, the distributions appear to significantly overlap.

4.5 Summary

This chapter presents the experimental results for the impact and post-impact performance of a composite plate. Samples were damaged by single and multiple impact events then tested to determine the residual flexural and compressive properties. The FE model developed in Chapter 3 was used to simulate the flexural response of a finite plate containing an elliptical inclusion of reduced stiffness. The apparent flexural modulus values from the FAI tests were used to determine the inclusion stiffness for a given damage size. The combination of inclusion dimensions and stiffness produce stress concentrations that would ultimately affect the residual flexural and compressive strength. These stress concentrations are compared to the ratios of nominal-to-residual strength to assess the viability of using a simple elastic model to approximate the post-impact performance of a composite plate damaged by single and multiple impacts.

As expected, impact characteristics are influenced by the incident energy. Therefore, three single impact energies were chosen to produce a distinct range of damage sizes. Comparing the impact characteristics of the three incident energies (low, middle, and high), it is evident that damage size increases with increasing energy. This also corresponds to an increase in contact duration and absorbed energy and a decrease of peak load. This relationship may be a result of the larger compliance of the plate as damage is introduced. Post-impact tests reveal that while the lowest energy has little effect on the residual flexural properties, there is a significant reduction of compressive strength. When observing a section through the damage site, it is clear that only few delaminations are created with little back-face damage (tensile matrix cracks). Since CAI

is traditionally known to be sensitive to delaminations, there is a more significant reduction from the nominal compressive strength. The middle and high energies, on the other hand, have distinct reductions from the nominal flexural and compressive properties.

The damage dimensions and apparent modulus are used to model the flexural response of a plate with an inclusion of reduced stiffness. The stiffness of the inclusion is adjusted to achieve the experimental modulus. When plotted against the damage diameter, the inclusion stiffness plateaus after an initial regression suggesting that the geometry of the inclusion compensates for slight reductions of stiffness. The corresponding moment concentration at the edge of the inclusion is also recorded. Since the modulus was not measured for the CAI samples, their inclusion stiffness could not be determined. Therefore, regression lines from the inclusion data of the FAI analyses were used to extrapolate the stiffness of the inclusions in the CAI samples according to their dimensions. The in-plane stress concentrations and flexural moment concentrations were compared to the experimental nominal-to-residual strength ratios. The FE model displayed good consistency and appeared to approximate the experimental results well. This lends confidence to the method of using flexural modulus and damage size to determine the residual strength of a damaged plate.

The multiple impact cases were conducted similarly to the single impact testing. Two separation distances were chosen to explore the effect of damage proximity on the impact and post-impact performance of a composite plate. A distance of 2in was chosen to produce two distinct but similar damage sites that do not overlap; a 0.5in distance was

also selected to allow overlap of the damage sites. Comparing the impact characteristics from the first and second impacts for the middle and high energies, it appears that the presence of damage 2in from the impact site does not influence the impact response of the plate. The post-impact data also shows little change from the single to multiple impact case for the flexural and compressive strength, whereas the apparent modulus has a more distinct reduction. Since the 2in distance prevents the damage sites from interacting, each site has similar properties as those modeled for the single impacts. Thus, each site may have the similar capacity as a single inclusion to affect the residual strength. The larger total area of reduced stiffness within the plate from multiple inclusions, however, may induce a loss of overall modulus. The 0.5in separated impacts displayed significant reduction for all of the post-impact properties, which may be due to the greater degree of damage induced by the overlap of the damage sites.

Modeling was again performed on the plates with separated impacts. The 0.5in samples were modeled with a single central inclusion since the individual damage sites became indistinguishable after the second impact. The 2in samples contained two distinct inclusions with unique dimensions and stiffness. Since the apparent modulus of these samples was also measured after the initial impact, it was possible to determine the unique stiffness for each inclusion. When compared to the results for single impact, the inclusion stiffness displayed a similar trend against the damage width. This is reasonable since the 2in distance was chosen to produce two distinct damage sites with similar properties to those from single impacts. The 0.5in samples, however, contained a steeper initial slope and lower plateau. This suggests that the inclusion overlap induces a greater

degree of damage for diameters comparable to those from single impacts. Just as for single impacts, the FE stress concentrations are compared to the experimental strength ratios. Again, the model displayed reasonable consistency and accuracy to the experimental data. The significance and applicability of these results will be discussed in Chapter 5, which will ultimately determine the basis for future work.

Chapter 5

CONCLUSIONS AND FUTURE WORK

5.1 Introduction

The goal of this research was to address the multiple impact performance of composite materials. In Chapter 4, a series of tests were conducted to measure the impact and post-impact response of a composite plate to repeated non-coincident impact events. The impact characteristics and residual mechanical properties were recorded as a means to distinguish the structural influence of multiple damage areas from that of a single damaged inclusion. An FE model was developed in Chapter 3 to approximate the stiffness loss within these damaged areas according to its dimensions under elastic flexural conditions. In this chapter, the information from these experiments will be discussed and conclusions will be drawn for the research questions posed in Chapter 1. These conclusions also determine the extent to which further experimentation must be conducted in order to establish a complete overview of the multiple impact performance of composite backing panel materials.

5.2 Multiple Impact Testing

This research explored the effects of multiple non-coincident impacts on a composite plate composed of potential materials. During use, a structural composite is expected to contain areas of reduced properties within the geometry of the part. These

areas can be introduced by a series of impacts and consist of a number of material damage types. The damage resistance of many composite systems to a single drop-weight impact has been tested extensively. However, little research has been conducted into multiple impacts, especially when the impact events occur at separate locations.

In this study, it was of primary concern to understand the influence of an initially damaged composite to repeated impacts. Not only was the number of impacts expected to influence the physical properties of the material but also the vicinity of the events may produce distinct effects. Comparing the impact characteristics of the initial and secondary impacts revealed that a damage site 2in from the impact site has little influence on the response of the plate. This appeared true for both the middle and high impact energies. The presence of damage 0.5in from the secondary impact site, however, appears to produce a more significant effect on the impact characteristics of the plate. This manifested as an increase in damage dimensions and absorbed energy, which also corresponded to an increase of contact duration and decreased peak load. This may be attributed to the greater compliance of a damaged plate. Sectioning through the damage center reveals that the 0.5in separated impacts induce a greater degree of damage in the form of delaminations, tensile, and transverse matrix cracks than the single or 2in impacts.

The greater extent of damage ultimately reduces the stiffness of the plate, which can be easily seen when compared to the single impact and post-impact results. There is a loss of 5% and 11% from the single impact modulus for 0.5in impacts at middle and high energies, respectively. These values are only 2% and 4% for the 2in separated impacts.

The residual flexural and compressive strengths of the 2in impacts also show little reduction from the single impact values. Since each of the 2in impacts produces a damage area similar to a single impact, it may be expected that their respective stress concentrations similarly influence the strength of the plate. The severity of the 0.5in impact damage, however, would more significantly influence the residual strength.

Flexural strength of the 0.5in separated impacts is 4% and 5% lower than the single impacts for the middle and high energies, respectively. The compressive strength, however, shows an 8% reduction from the single impact values. Traditionally, CAI is known to be sensitive to the presence of delaminations. The larger delaminations caused by the 0.5in impact, therefore, corresponds to a greater loss of residual compressive strength. Thus, multiple non-coincident impact testing may be a suitable means to gauge the damage tolerance of a given composite system. Tracking changes in impact characteristics and post-impact properties may be used to rank materials just as CAI has been traditionally used.

5.3 Flexure after Impact (FAI)

One of the objectives of this research was to investigate the feasibility of an elastic flexural test as an effective metric for the residual properties of an impacted composite. For years the CAI method has been accepted as the standard gauge for the damage tolerance of composites with impact-induced damage. This technique, however, has a number of drawbacks. The fixturing required for the test involves extensive tolerancing and proper edge conditions to produce a reliable result. Improper torque in the assembly, an out-of-perpendicular sample, or gaps between the edge supports would

produce undesirable failure modes that must be entirely disregarded. Strain gauge placement is also necessary to extract the compressive modulus data from the test. CAI nominally provides residual compressive strength results that may not represent the application loading intended for the material, which it does not for the considerations of this research. Ultimately, the CAI method is a destructive test that negates the reusability of the tested structure.

FAI provides a simple means to test the applicable residual response of a damaged composite structure. Only simple fixtures are required and the nominal test gives both flexural modulus and strength data. As a nondestructive test, however, a relationship between the flexural modulus and other residual properties must be established. It has been shown that the apparent flexural modulus is sensitive to the damage size associated with a particular impact energy level. The number and proximity of multiple impacts also appear to uniquely influence the flexural stiffness. By using a simple elastic model to simulate the flexural response of a damaged plate, it may be possible to determine the reduced stiffness properties of an idealized damage inclusion and the resulting concentration of stress. This stress concentration may be comparable to the experimental strength loss measured from the CAI and FAI tests.

As described above, the flexural modulus and damage dimension were used to determine the stiffness of a commensurate elliptical inclusion in the model developed in Chapter 3. The combination of the inclusion dimensions and stiffness produce a unique stress concentration at the inclusion's edge. Since failure during the CAI and FAI tests

are likely due the stress concentration induced by the damage site, there should be a reasonable relationship between the FE and experimental results.

The FE results are plotted against the experimental data; therefore a line with slope, $m = 1$ (1:1 ratio), would suggest that the model exactly predicts the experimental strength loss. For single impacts, the slope of this line is 1.04 suggesting that the model consistently, but slightly, underestimates the loss of flexural strength. For the 2in and 0.5in separated impacts, however, the slope becomes 0.60 and 0.56, respectively. Therefore, the model predictions for residual strength are more conservative, showing a much higher loss. The data for the single and multiple impacts show good correlation to these regression lines ($R^2 = 0.95, 0.78, 0.94$, respectively). Thus, while the predictions are not exact, they are consistently good or conservative.

Since the modulus of the CAI samples was not measured, their exact inclusion stiffness, and hence stress concentrations, could not be determined. Therefore, inclusion data for the FAI analyses was used to extrapolate the stiffness of the CAI inclusions according to their dimensions. Just as for the flexural strength, the FE in-plane stress concentrations were compared to the experimental data, and a 1:1 ratio suggests complete accuracy. Contrary to the flexural strength, the in-plane model appears to overestimate the strength loss for the single impacts ($m = 0.71$). Again, however, the model underestimates the residual strength of the 2in ($m = 0.99$) and 0.5in ($m = 0.92$) separated impacts. This data, however, is consistent with its respective regression lines ($R^2 = 0.87, 0.88, 0.81$). Thus, with a computationally inexpensive model it is possible to conservatively approximate the residual strength of an impact-damaged plate based the

resulting damage dimensions and elastic flexural modulus. Given the consistency of the model's predictions, accuracy may also be improved by applying a suitable correction factor.

5.4 Damage Width Analysis

During application it is often impractical to remove and test a damaged structure in order to determine its residual properties. This research has proposed a method for approximating the residual properties of an impacted composite based on the resulting damage size. While it is difficult to accurately measure the area enclosed by the damage boundary, more accuracy can be achieved by simply measuring the largest width relative to the structure's geometry. This technique could potentially be performed in the field to generate a rough estimate of the residual properties and provide insight into the structures survivability.

In this study the damage has been considered an elastic inclusion with mechanical properties lower than the surrounding material. The degree of stiffness loss in the inclusion will directly influence the stress concentration created by the inhomogeneity. While expressions exist for an infinite plate with an inclusion (Section 3.2.1), these solutions are computationally expensive and are beyond the requirements of this study. Since advancements in the infinite solution have only emerged recently, there has been little consideration to the effect of a finite width panel. To bridge this gap, a simple finite element model has been developed in ABAQUS (Section 3.2.4) to determine the interaction of an inclusion of arbitrary stiffness with boundaries of a finite width parent structure.

As expected, larger damage areas are associated with a greater degree of damage as can be seen when plotting the inclusion stiffness against the damage width. Initially, the growth of damage corresponds to a loss of stiffness. The regression of stiffness with damage diameter is similar for the single and 2in separated impacts. This is likely a result of the separation distance, for which the two impacts produce damage similar to a single impact of the same energy. There is a greater loss of stiffness, however, for the 0.5in impacts. The overlap of damage generates a greater extent of damage but does not drastically increase the damage diameter. The loss of stiffness for each impact type eventually plateaus at nearly 50% reduction with increasing diameters. This plateau may be attributed to more significant interaction of the stress concentration caused by the inclusion with the edge of the plate. As such, the geometry of the inclusion becomes a larger influence over the loss of global modulus than the loss of inclusion stiffness.

This trend manifests for each of the impact types: single, 2in, and 0.5in. With more testing, a more substantial trend can be defined that could show a strong correlation between inclusion stiffness and diameter. Thus, if the damage dimensions are known, it would be possible to use the design charts to approximate the residual properties. As discussed in the previous section, these approximations may be used where conservative estimates are suitable. More testing is needed to determine the particular relationship between the FE model and experimental CAI tests, but preliminary extrapolations are encouraging for further investigation.

5.5 Future Work

This study was conducted to explore the effects of multiple non-coincident impacts on the impact and post-impact response of a structural composite material. It was concluded that multiple impacts with overlapping damage zones more significantly influence the impact characteristics and residual mechanical properties than those with distinct, but similar, damaged regions. However, only a single material was investigated in these experiments and significant scatter existed in the raw data. As discussed in Chapter 1, a number of factors can influence the impact performance of a backing panel material. These can include matrix material, fiber material and surface treatment, preform stitching, weave patterns, and layup sequence as well as many others. Further testing can be used to rank the damage tolerance of these materials and to establish the consistency and practicality of this method.

Unfortunately, the results from these experiments cannot be scaled to thick-section composite testing. Different structural mechanisms are activated or amplified when a large composite panel is dynamically loading by a high-energy impact. The procedures used in this research, however, were designed to be modified to accommodate these larger panels and energies. It is unclear whether the backing panels might display similar impact and post-impact tendencies as the composites tested in this study. Extensive testing is needed to confirm the large-scale applicability of this research method and to categorize the effect of various material factors on the multiple impact performance of backing panel composites.

REFERENCES

- [1] ASTM D7136/D7136M-05, Standard test method for measuring the damage resistance of a fiber-reinforced polymer matrix composite to a drop-weight impact event. *Annual Book of ASTM Standards*, American Society for Testing and Materials, West Conshohocken, PA, USA, 2005.
- [2] Tracy, J. J., Dimas, D. J., and Pardoen, G. C., The effect of impact damage on the dynamic properties of laminated composite plates, *Proceedings of the 5th International Conference on Composite Materials*, 1985, 111-125.
- [3] Kwon, Y. S. and Sankar, B. V., Indentation-flexure and low-velocity impact damage in graphite epoxy laminates, *Journal of Composite Technology and Research*, 1993, **15**(2), 101-111.
- [4] Kumar, P. and Narayanan, M. D., Energy dissipation of projectile impacted panels of glass fabric reinforced composites, *Composite Structures*, 1990, **15**, 75-90.
- [5] Morton, J. and Godwin, E. W., Impact response of tough carbon fibre composites, *Composite Structures*, 1989, **13**, 1-19.
- [6] Wang, C. J., Jang, B. Z., Panus, J., and Valaire, B. T., Impact behavior of hybrid-fiber and hybrid-matrix composites, *Journal of Reinforced Plastics and Composites*, 1991, **10**(4), 356-378.
- [7] Lagace, P. A. and Wolf, E., Impact damage resistance of several laminated material systems, *Proceedings of the 34th AIAA Structures, Structural Dynamics and Materials Conference*, 1993, 1863-1872.
- [8] Wang, H. and Khang, T. V., Low velocity impact damage of carbon/PEEK crossply laminates, *Proceedings of the 8th International Conference on Composite Materials*, **28**(K), 1-11.
- [9] Hull, D. and Shi, Y. B., Damage mechanism characterization in composite damage tolerance investigations, *Composite Structures*, 1993, **23**, 99-120.
- [10] Hosur, M. V., Karim, M. R., and Jeelani, S., Studies on stitched woven S2 glass/epoxy laminates under low velocity and ballistic impact loading, *Journal of Reinforced Plastics and Composites*, 2004, **23**, 1313-1323.

- [11] Sugun, B. S. and Rao, R. M. V. G. K., Low-velocity impact characterization of glass, carbon, and Kevlar composites using repeated drop tests, *Journal of Reinforced Plastics and Composites*, 2004, **23**, 1583-1599.
- [12] Morais, W. A., Monteiro, S. N., and d'Almeida, J. R. M., Evaluation of repeated low energy impact damage in carbon-epoxy composite materials, *Composite Structures*, 2005, **67**, 307-315.
- [13] Icten, B. M., Repeated impact behavior of glass/epoxy laminates, *Polymer Composites*, 2008, DOI 10.1002/pc.20728.
- [14] Wyrick, D. A. and Adams, D. F., Damage sustained by a carbon-epoxy composite material subjected to repeated impact, *Composites*, 1988, **19**(2), 19-27.
- [15] Wyrick, D. A. and Adams, D. F., Residual strength of a carbon-epoxy composite material subjected to repeated impact, *Journal of Composite Materials*, 1988, **22**(3), 749-765.
- [16] Rotem, A., The strength of laminated composite materials under repeated impact loading, *Journal of Composite Technology and Research*, 1988, **10**(2), 74-79.
- [17] Harris, B., Chen, A. S., Coleman, S. L., and Moore, R. J., Residual strength and toughness of damaged composites, *Journal of Materials Science*, 1991, **26**, 307-320.
- [18] ASTM D7137/D71737M-05, Standard test method for compressive residual strength properties of damaged polymer matrix composite plates. *Annual Book of ASTM Standards*, American Society for Testing and Materials, West Conshohocken, PA, USA, 2005.
- [19] Ghasemi Nejjhad, M. N. and Parvizi-Majidi, A., Impact behavior and damage tolerance of woven carbon fiber-reinforced thermoplastic composites, *Journal of Engineering Materials Technology*, 1990, **113**, 93-98.
- [20] Chen, G. S., Bidinger, G. M., and Lou, M. C., Impact damage tolerance of thin wall composite struts, *Proceedings of the 34th AIAA Structures, Structural Dynamics and Materials Conference*, Part 2, 847-858.
- [21] Pintado, P., Vogler, T. J., and Morton, J., Impact damage development in thick composite laminates, *Composites Engineering*, 1991, **1**(4), 195-210.
- [22] Manders, P. W. and Harris, W. C., A parametric study of composite performance in compression-after-impact testing, *SAMPE Journal*, 1986, **22**, 47-51.

- [23] Dost, E. F., Ilcewicz, L. B., and Avery, W. B., Effects of stacking sequence on impact damage resistance and residual strength for quasi-isotropic laminates, *ASTM STP 1110*, 1991, 476-500.
- [24] Monib, A., Gillespie, J. W., Jr., and Fink, B. K., Damage tolerance of thick-section composites subjected to ballistic impact. Master's Thesis, University of Delaware: Center for Composite Materials, Newark, DE, USA, 1999.
- [25] ASTM D6272-02, Standard test method for flexural properties of unreinforced and reinforced plastics and electrical insulating materials by four-point bending. *Annual Book of ASTM Standards*, American Society for Testing and Materials, West Conshohocken, PA, USA, 2002.
- [26] Zhang, Z. Y. and Richardson, M. O. W., Low velocity impact induced damage evaluation and its effects on the residual flexural properties of pultruded GRP composites, *Composite Structures*, 2007, **81**, 195-201.
- [27] Chenghong, H., Yubin, L., Zuoguang, Z., and Zhijie, S., Impact damage modes and residual flexural properties of composite beams, *Journal of Reinforced Plastics and Composites*, 2008, **0**(0), 1-14.
- [28] Peijs, A. A. J. M., Venderbosch, R. W., and Lemstra, P. J., Hybrid composites based on polyethylene and carbon fibres; Part 3: impact resistant structural composites through damage management, *Composites*, 1990, **21**(6), 522-530.
- [29] Mouritz, A. P., Gallagher, J., and Goodwin, A. A., Flexural strength and interlaminar shear strength of stitched GRP laminates following repeated impacts, *Composites Science and Technology*, 1997, **57**, 509-522.
- [30] Mariatti, M., Nasir, M., and Ismail, H., The flexural behavior of woven prepreg thermoplastic composites, *Journal of Thermoplastic Composite Materials*, 2001, **14**, 290-305.
- [31] Kim, J. K., Mackay, D. B., and Mai, Y. W., Drop-weight impact damage tolerance of CFRP with rubber-modified epoxy matrix, *Composites*, 1993, **24**(6), 485-494.
- [32] Simacek, P., Heider, D., Gillespie, J. W., Jr., and Advani, S. G., Post-filling flow in vacuum assisted resin transfer molding processes: Theoretical analysis, *Composites Part A: Applied Science and Manufacturing*, 2009, **40**(6-7), 913-924.
- [33] ASTM D792-00, Standard test methods for density and specific gravity (relative density) of plastics by displacement. *Annual Book of ASTM Standards*, American Society for Testing and Materials, West Conshohocken, PA, USA, 2000.

- [34] ASTM D2734-94 (Reapproved 2003), Standard test method for void content of reinforced plastics. *Annual Book of ASTM Standards*, American Society for Testing and Materials, West Conshohocken, PA, USA, 2000.
- [35] ASTM D2584-02, Standard test method for ignition loss of cured reinforced resins. *Annual Book of ASTM Standards*, American Society for Testing and Materials, West Conshohocken, PA, USA, 2002.
- [36] S-2 Glass Fiber: The High Performance System Solution. *Advanced Materials: Solutions for Demanding Applications*, AGY, Aiken, SC, USA, 2004.
- [37] Chatterjee, A., Deitzel, J., and Gillespie, J. W., Jr., University of Delaware: Center for Composite Materials, Internal literature, Newark, DE, USA, 2004.
- [38] Blake, R. A., *et al.*, *Test Methods Volume 6*, Delaware Composites Encyclopedia, Technomic Pub. Co., 1990.
- [39] ASTM D3410-M95, Standard test method for compressive properties of polymer matrix composite materials with unsupported gage section by shear loading, *Annual Book of ASTM Standards*, American Society for Testing and Materials, West Conshohocken, PA, USA, 2000.
- [40] Lekhnitskii, S. G., *Anisotropic plates*. New York, USA: Gordon and Breach Science Publishers; 1968.
- [41] Gillespie, J. W. Jr., Rothschilds, R. J., and Carlsson, L. J., Influence of finite width on notched laminate strength predictions. *Composites Science and Technology*, 1988, **32**, 15-30.
- [42] Whitney, J. M., and Nuismer, R. J., Stress fracture criteria for laminated composites containing stress concentrations. *Journal of Composite Materials*, 1974, **8**, 253-265.
- [43] Cheng, Z. Q. and Reddy, J. N., Laminated anisotropic thin plate with an elliptic inhomogeneity, *Mechanics of Materials*, 2004, **36**, 647-657.
- [44] Hsieh, M. C. and Hwu, C., Anisotropic elastic plates with holes/cracks/inclusions subjected to out-of-plane bending moments, *International Journal of Solids and Structures*, 2002, **39**, 4905-4925.
- [45] Bert, C. W. and Zeng, H. Generalized bending of a large, shear deformable isotropic plate containing a circular hole or rigid inclusion, *Journal of Applied Mechanics*, 2001, **68**, 230-233.

- [46] Ramesh, S. S., Wang, C. M., Reddy, J. N., and Ang, K. K., Computation of stress resultants in plate bending problems using higher-order triangular elements, *Engineering Structures*, 2008, **30**, 2687-2706.
- [47] Ting, T. C. T., *Anisotropic elasticity: theory and applications*, Oxford University Press, New York, 1996.
- [48] Eshelby, J. D., The determination of the elastic field of an ellipsoidal inclusion, and related problems, *Proceedings of the Royal Society of London, Series A*, 1957, **241**, 376-396.
- [49] Vinson, J. R. and Sierakowski, R. L., The behavior of structures composed of composite materials. 2nd Ed., *Solid Mechanics and Its Applications*, **105**, Netherlands: Kluwer; 2002.
- [50] Reissner, E., On the analysis of first and second-order shear deformation effects for isotropic elastic plates, *Journal of Applied Mechanics*, 1980, **47**, 959-961.
- [51] Zeng, H. and Bert, C. W., Generalized bending of shear-deformable plate elastic inclusion, *Journal of Engineering Mechanics*, 2001, 927-931.
- [52] Ablas, J. B., *Theorie van de driedimensionale spanningstoestad in een doorboorde plaat*, Doctoral dissertation, Tech Univ, Delft, The Netherlands, 1957.
- [53] Shuart, M. J. and Prasad, C. B., Analysis and experiments for composite laminates with holes and subjected to 4-point bending, *Proceedings of the 31st AIAA Structures, Structural Dynamics and Materials Conference*, 1990, Pt. 2, **2**, 748-758.
- [54] Chen, H. C., Bending of laminated composite plates with cutouts, *Proceedings of the 38th AIAA Structures, Structural Dynamics and Materials Conference*, 1997, Pt 3, **3**, 1884-1892.
- [55] Madenci, E., Barut, A., and Nemeth, M. P., A complex potential method-variational method for stress analysis of unsymmetric laminates with and elliptical cutout, *Journal of Applied Mechanics*, 2001, **68**, 731-739.
- [56] Shyr, T.-W. and Pan, Y.-H., Impact resistance and damage characteristics of composite laminates, *Composite Structures*, 2003, **62**, 193-203.